PFC/RR-84-12 DOE/ET/51013-129

ICRF ANTENNA COUPLING THEORY FOR A CYLINDRICALLY STRATIFIED PLASMA

B. McVey

Plasma Fusion Center
Massachusetts Institute of Technology
Cambridge, MA 02139

July 1984

This work was supported by the U. S. Department of Energy Contract No. DE-AC02-78ET51013. Reproduction, translation, publication, use and disposal, in whole or in part by or for the United States government is permitted.

Abstract

Antenna coupling to a cyclindrical plasma is examined for the ion cyclotron range of frequencies (ICRF). A variety of antenna configurations are modelled such as a partial-turn loop, Nagoya coils, an aperture antenna, and arrays of coils. A procedure that utilizes the induction theorem is presented which replaces a general coil configuration with an equivalent representation in terms of sinusoidal current sheets. This transformation reduces the three dimensional antenna boundary value problem to that of one dimension (r, the radial coordinate) with the spatial variation in the other directions represented by complex exponentials ($\exp((in\phi + ik_z z))$. As constructed, the transformation is directly applicable to axisymmetric geometries where the plasma parameters are only functions of radius. The radial variation of the plasma parameters such as the local density and temperature are approximated by a stratified model. As the number of strata are increased, the step-wise model is shown to converge to the continuous case. The plasma response is modelled by a local equivalent dielectric tensor. In the context of this model antenna-plasma coupling characteristics are compared for the various ICRF antennas.

Contents

1. Introduction

The vacuum and the linear self-consistent plasma electromagnetic fields are calculated for the antenna configurations shown in Fig. 1.1. This section contains a short review of ICRF antenna coupling physics, a brief description of the antenna-plasma coupling problem that is solved, and a note on the computer program, "ANTENA".

1.a) ICRF antenna coupling physics: RF heating in the ion cyclotron range of frequencies (ICRF) has established itself as an efficient method of adding supplemental power to magnetically confined plasmas.[1,2] The basic configuration for all ICRF experiments is that of an antenna inside a vacuum tank yet external to the plasma boundary which is defined by a limiter. The application of RF power generates reactive fields near the antenna that may couple to the natural wave modes of the plasma, or directly interact with the plasma particles passing close to the antenna.

In the ICRF, the natural wave modes can be divided into two groups; fast modes with wavelengths comparable to or greater than the plasma scale length, and slow modes with shorter wavelengths comparable to an ion gyroradius. Among the long wavelength modes are the fast magnetosonic wave and the ion cyclotron wave. These modes are an extension of the MHD compressional and shear Alfven waves, respectively, to higher frequencies ($\omega \sim \omega_{ci}$). The identity of the slow modes is dependent upon the wave frequency relative to the cyclotron frequency and upon the direction of propagation relative to the magnetic field. Among these modes we have the ion Bernstein waves,[3] the two-ion hybrid mode,[4] the electrostatic ion cyclotron wave,[5] the kinetic Alfven wave,[6] and an ordinary slow wave (same polarization as the ECRH ordinary mode). In a plasma, the fast and slow modes do not necessarily propagate independently and exhibit coupling at

Fig. 1.1 Various ICRF Antennas

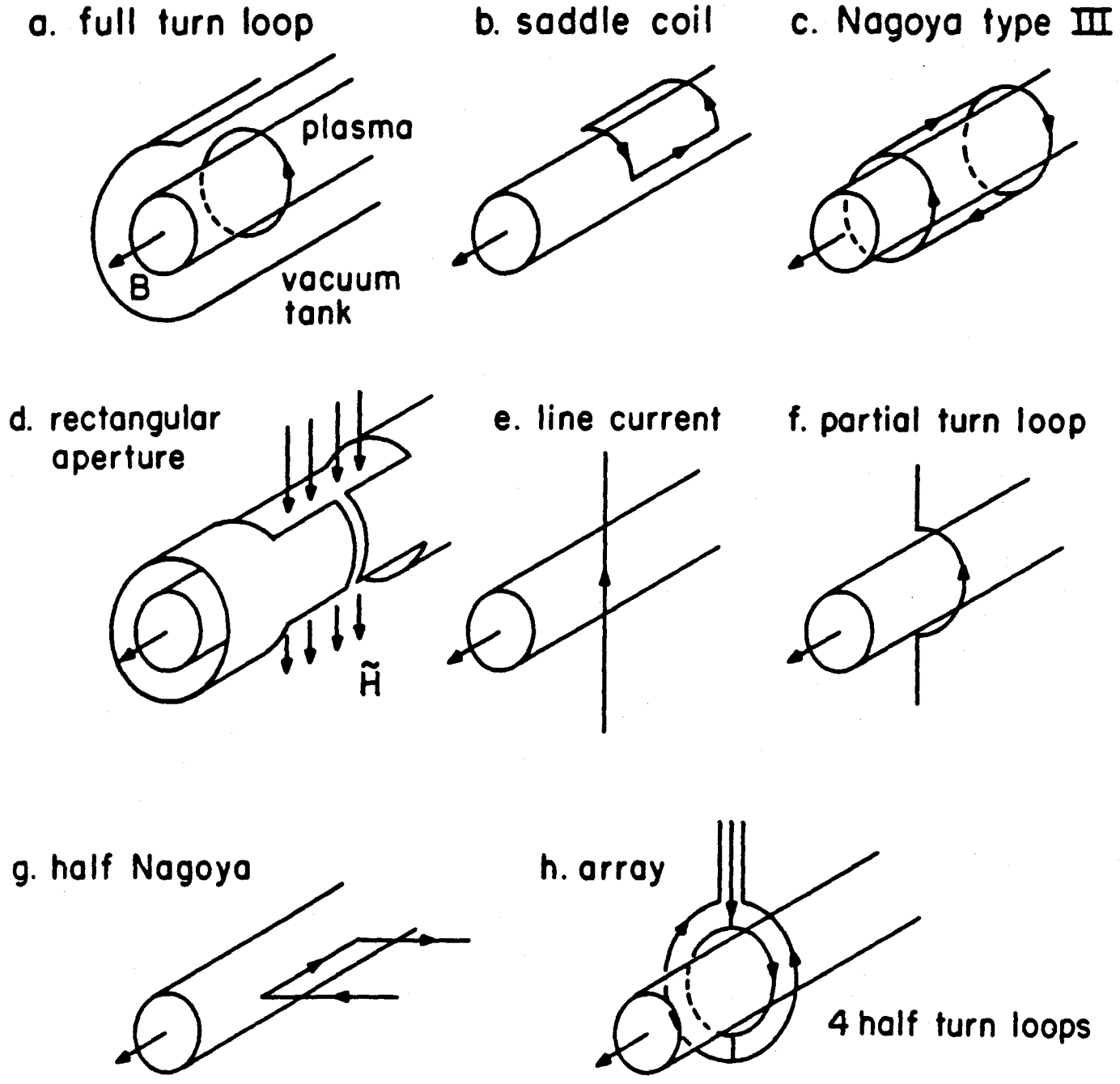

mode conversion layers. As an example, the fast magnetosonic wave couples to an ion Bernstein wave at the harmonics of the cyclotron frequency.[7,8] Further, since neither the polarization of the fast or slow mode matches the vacuum fields of the antenna, both modes can be directly excited in the edge density gradient of the plasma.

In general, the development of ICRF antennas has focussed on efficient coupling of power to the natural wave modes of the plasma. The mode that is utilized is dependent upon the geometry of the confining magnetic field. In early mirror and stellarator experiments, antennas were designed for efficient power transfer to an ion cyclotron wave.[9,10] The ion cyclotron wave propagates along the confining magnetic field and antennas that impose a finite k_z (k_z is the wave number along the magnetic field) were designed such as the "Stix" coil. Analysis of antenna coupling to an ion cyclotron wave lead to the "current sheet" representation of an antenna, a physically appealing concept that provides the basis of antenna modelling in this report.[11] With the advent of the tandem mirror and other multiple mirrors, antenna coupling to an ion cyclotron wave as an experimental research topic has been revitalized.

The tokamak geometry requires a wave that propagates across the magnetic field lines. Successful ICRF heating experiments have utilized the fast magnetosonic wave.[1,2,12] In the tokamak device, antenna design is restricted due to accessibility, and the emerging antenna configuration has been the partial turn loop (refer to Fig. 1.1f). Aperture antennas and dielectrically loaded waveguide launchers have been proposed, but as of yet untested experimentally. Recently, an efficient RF heating experiment was performed on the JIPPT-II-U tokamak using a half-Nagoya antenna (refer to Fig. 1.1g).[13] This experiment was interpreted as direct excitation of ion Bernstein waves by the antenna, and recent work on the ACT-1 tokamak has focussed on antenna coupling to the ion Bernstein wave.[14]

In many plasma experiments, the direct interaction of the near fields of the antenna with the plasma particles provides the dominant physics. This is particularly true at low frequencies or where the antenna is large compared to the dimensions of the plasma. RF plugging experiments at Nagoya University position antennas in the mirror throats of a magnetic cusp geometry.[15] The near fields of the antenna generate a ponderomotive potential that plugs the velocity space loss cone of the cusp. Some of the antennas of Fig. 1.1 were developed in this series of experiments and are so named. At low frequencies in a heavy ion plasma, ICRF heating has been used in the plasma separation process.[16] In this process, a careful examination of the near fields of the antenna can optimize performance. In ICRF heating experiments in a tokamak geometry, impurity influx due to ion sputtering can limit heating efficiency. The drive for the ion sputtering may be due to the near field interaction of the antenna with the low density plasma outside a limiter. ICRF heating experiments in the Phaedrus tandem mirror have measured additional features of near field antenna interaction with a plasma. Anomalously high (greater than a Boltzmann factor) ambipolar potentials have been measured close to ICRF antennas.[17] It has been suggested that direct electron pumping by the near fields of the antenna may account for the potential structure. Second, ICRF has been observed to provide stabilization of an otherwise MHD unstable simple mirror configuration.[18] The stability appears to be due to a radial ponderomotive force that reduces the bad curvature drift.

1.b) A description of antenna and plasma model: Shown in Fig. 1.1 is a schematic of the antennas that are modelled (filamentary coils are shown for clarity). These antennas may be superimposed to provide a variety of other antenna configurations as illustrated in the figure. The choice of antennas that are modelled is a reflection of antenna geometries that have been used in the past or proposed for future ICRF experiments. The full turn loop antenna is one element of a "Stix" coil, or it may be the optimal coil for

applications where azimuthal uniformity is required. The Nagoya type III coil was empirically found to be the optimal coil for high density RF plugging applications in a cusp geometry.[18] The saddle coil is a variation of the type III coil that may be used to generate a high azimuthal mode number near field geometry. The half-Nagoya coil is a one element of the type III coil with radial feeders. A phased array of 4 half-Nagoya coils is used on the RFC-XX multiple mirror experiment. The line current antenna models the rod antennas used in RF trapping experiments in the Phaedrus tandem mirror end plugs.[17] The partial or half turn loop antenna is the most popular in ICRF heating of tokamaks. Finally, the aperture antenna has been used in stellarator experiments[19] and will be experimentally tested in a tandem mirror geometry.

For the antennas of Fig. 1.1, the electromagnetic fields are calculated everywhere inside the vacuum tank $r \leq c$ (refer to Fig. 1.2). In addition to the electromagnetic fields, integrated quantities such as the local power deposition in the plasma, the power flow across a cylinder of constant radius, and the power flow out of the antenna (resistance and reactance) are calculated. The electromagnetic fields are determined by solving the time-harmonic form of Maxwell's equations.

$$\nabla \times \vec{E}(\vec{r}) = i\omega\mu_o \vec{H}(\vec{r}) \tag{1.1}$$

$$\nabla \times \vec{H}(\vec{r}) = -i\omega\varepsilon_o \overleftrightarrow{\epsilon}(r) \cdot \vec{E}(\vec{r}) + \vec{J}_{ext}(\vec{r}) \tag{1.2}$$

$$\text{domain:} \quad r \leq c \tag{1.3}$$

Fig. 1.2 Antenna - Plasma Geometry

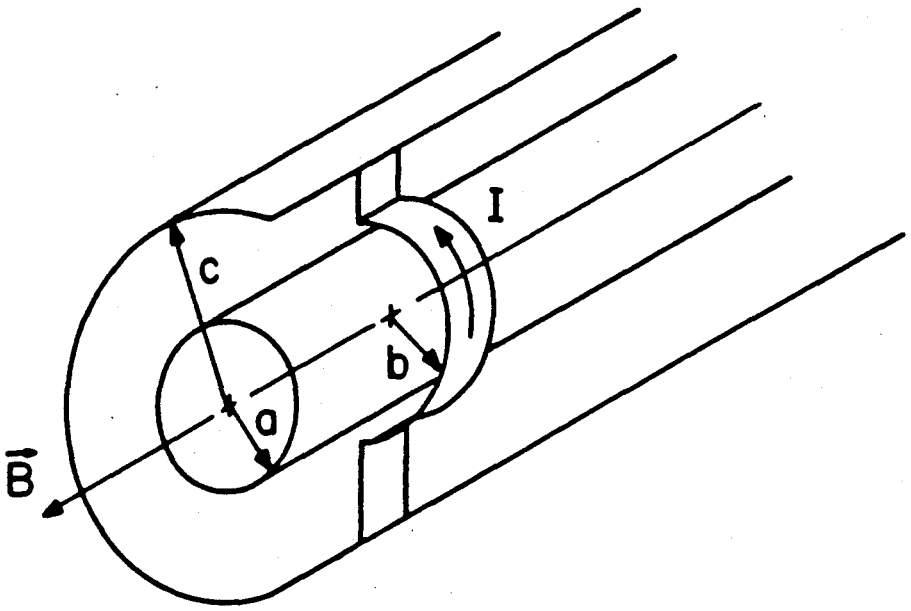

a = plasma radius
b = inside radius of coil
c = vacuum tank radius

The antenna is modelled by the external current density, $\vec{J}_{ext}$, which is a function of $\vec{r}$. The self-consistent current response of the plasma is modelled by a "local" equivalent dielectric tensor which is assumed to be only a function of the radial coordinate, r. Boundary conditions are imposed at the radius r = c such that Eqs. 1.1 - 3 define a boundary value problem with a unique solution.

The method used to obtain a solution to Eqs. 1.1 - 3 is outlined by the organization of the paper. If one removes the antennas from Fig. 1.1, the geometry is uniform in ϕ and z. The spatial variation of field quantities in these coordinates may be represented by an inverse Fourier transform, Eq. 2.1. Applying the Fourier transform (Eq. 2.2) to Eqs. 1.1 and 1.2 reduces Maxwell's equations to a coupled set of ordinary differential equations. Next, consider coil configurations located at a constant radius r = b (such as a full turn loop). On the cylinder (r = b) the spatial variation of the current density can also be represented by the inverse Fourier transform. This is the "current sheet" representation of the antenna defined in Sec. 2. In this case, three spatial domains are defined by the plasma radius, $r \leq a$; the coil radius, $a \leq r \leq b$; and the vacuum tank radius, $b \leq r \leq c$. In each domain, Maxwell's equations are reduced to a set of ordinary differential equations that have a unique solution, provided appropriate boundary conditions at r = a, r = b, and r = c are defined. These boundary conditions are defined in Sec. 2.a. The antenna current enters through a jump condition in the transverse magnetic field at r = b. The boundary conditions at r = b and r = c may be generalized to allow for magnetization currents (i.e., jump conditions in the transverse electric field) as defined in Sec. 2.c.

The radial feeders of some of the antenna configurations appear to pose a difficulty in using the above analysis. However, in Sec. 3, the induction theorem is used to represent an arbitrary antenna geometry defined in the

domain $b \leq r \leq c$, by equivalent electric and magnetization currents at $r = b$ and $r = c$. This provides a generalization of the current sheet concept to handle all antenna configurations. Appendices C and D contain derivations of the Fourier transforms of the equivalent current sheet representations for the antennas of Fig. 1.1. The 3-D boundary value problem of Eqs. 1.1 to 1.3 and Fig. 1.1 has been reduced to a 1-D radial boundary value problem (Fig. 2.2) for a specified azimuthal (n) and axial (k_z) mode number. For a given set of mode numbers (n, k_z); in Sec. 4 the inductive vacuum fields are calculated, in Sec. 5 the plasma current response is defined, and in Sec. 6 the self-consistent plasma fields are calculated. The total field solution is then obtained via the inverse Fourier transform of Eq. 2.1.

1.c) The computer code "ANTENA": The computer code "ANTENA" embodies the electromagnetic field calculation presented in this report. This code is a user-oriented computer code that is described in an accompanying MIT report, "ANTENA USER GUIDE". One function of this report is to define the physics contained in that computer code. All of the results presented in Sec. 7 were obtained from running "ANTENA". The notation used in "ANTENA" closely follows that used in this report. For convenience, a glossary of symbols used in this report is tabulated in Appendix A. The Fortran coding of the equations in this report are noted by comment statements in "ANTENA".

2. Current Sheet Method of Solution

This section 1) defines the current sheet concept which reduces the 3-D boundary value problem (B.V.P.) to a 1-D problem in (n, k_z) space, 2) provides sufficient boundary conditions to define a unique solution to the 1-D B.V.P.; and 3) defines axial boundary conditions that may be used to model various machine geometries.

2.a) The current sheet concept: A current sheet is defined as an imaginary cylindrical tube ($r = b$) supporting an infinitesimally thin surface current. In the plane of the tube, the surface current is assigned a complex exponential spatial variation of the form, $\exp [in\phi + ik_z z]$. The current sheet is schematically represented in Fig. 2.1. It will be shown in the next section that the electromagnetic fields of all of the antennas of Fig. 1.1 can be constructed by using a number of current sheets of the above form. Thus, the solution of the general antenna-plasma boundary value problem can be reduced to one where the antenna has a particularly simple form.

If the current sheet is removed from Fig. 2.1, one observes that the geometry is uniform in the z and ϕ directions. Spatial variations of field quantities in these coordinates may be represented in terms of orthogonal functions. Due to the uniformity, complex exponentials may be used.

$$F(r, \phi, z) = \frac{1}{2\pi} \int_{-\infty}^{\infty} dk_z \sum_{n=-\infty}^{\infty} F(r, n, k_z)\, e^{in\phi + ik_z z} \qquad 2.1$$

Associated with the above inverse transform is the transform to wave number space,

Fig. 2.1 Current Sheet Model

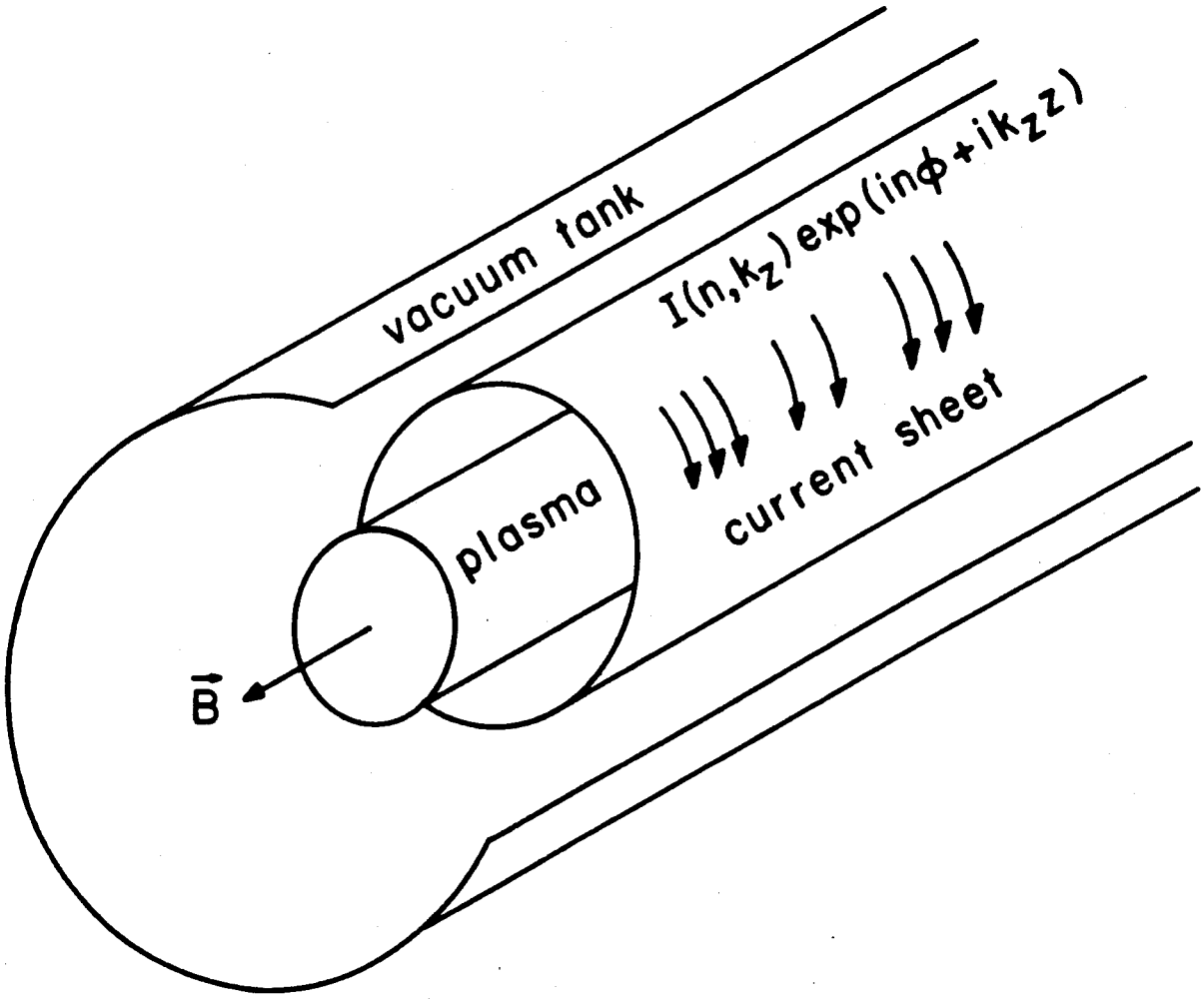

$$F(r, n, k_z) = \int_{-\infty}^{\infty} dz \; \frac{1}{2\pi} \int_{0}^{2\pi} d\phi \; F(r, \phi, z) \; e^{-in\phi - ik_z z} \qquad 2.2$$

We refer to Eq. 2.2 as the $n - k_z$ transform. If one now returns to the current sheet concept, Eqs. 2.1 and 2.2 state that the spatial variation of a current distribution can be represented by an infinite set of current sheets each assigned a weight given by Eq. 2.2. As an example, the $n - k_z$ transform of the current distribution of a full-turn loop is given by Eq. C.4. This Fourier coefficient is referred to as the $n - k_z$ spectrum of the antenna.

2.b) Boundary conditions for an electric current at r = b: Visualizing the antenna as a sum of current sheets provides a method of reducing a three-dimensional boundary value problem to one-dimensional (in the radial direction) boundary value problem. Working in $n - k_z$ space and referring to Fig. 2.2a, the field solution is defined if boundary conditions are imposed at the surfaces r = a, r = b, and r = c. For the current sheet configuration of that figure, the following boundary conditions are imposed:

at r = a (plasma-vacuum interface),

$$E_\phi(a - \epsilon, n, k_z) = E_\phi(a + \epsilon, n, k_z) \qquad 2.3a$$

$$E_z(a - \epsilon, n, k_z) = E_z(a + \epsilon, n, k_z) \qquad 2.3b$$

$$H_\phi(a - \epsilon, n, k_z) = H_\phi(a + \epsilon, n, k_z) \qquad 2.3c$$

$$H_z(a - \epsilon, n, k_z) = H_z(a + \epsilon, n, k_z) \qquad 2.3d$$

Fig. 2.2 Radial Boundary Value Problem

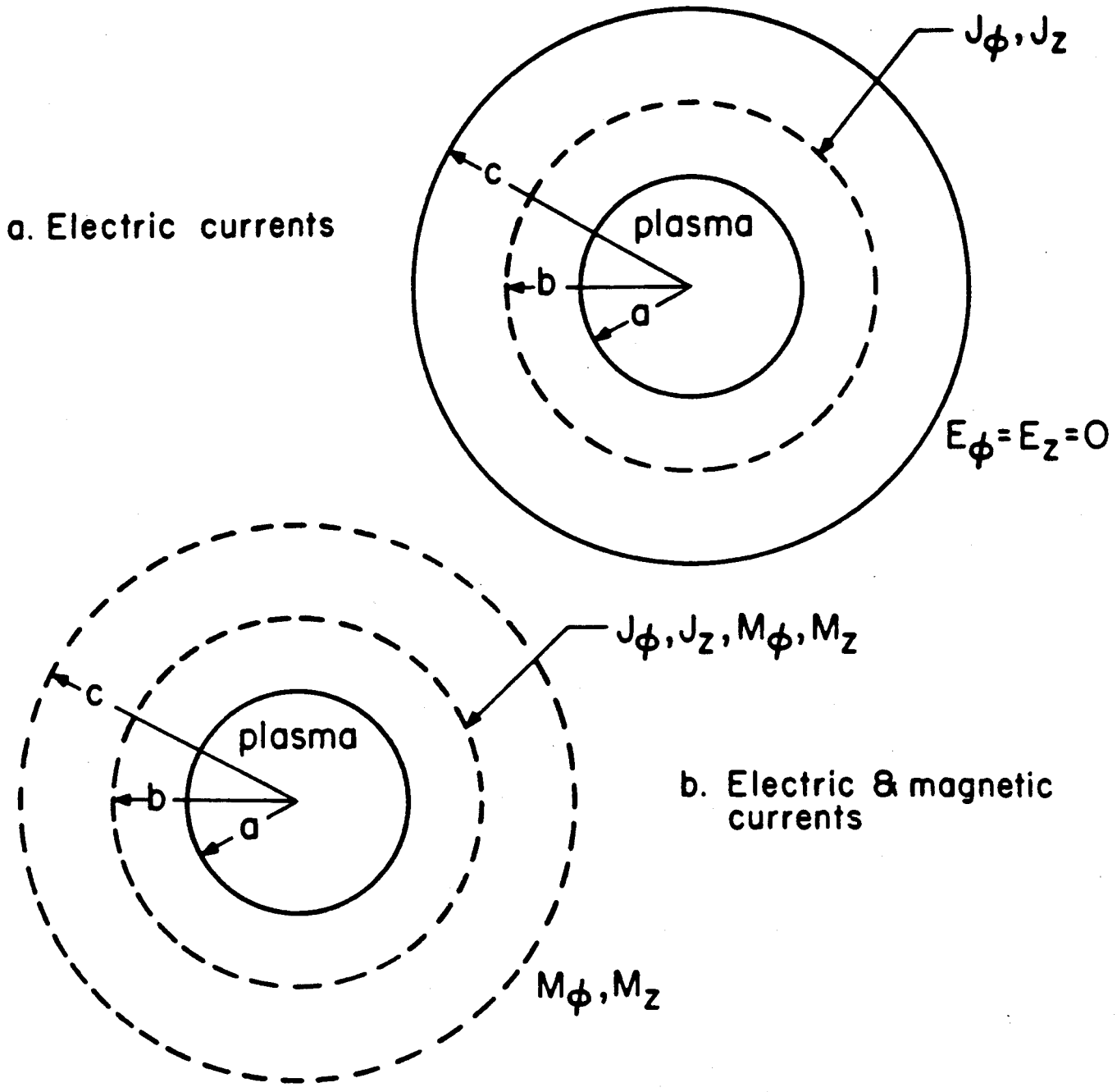

where ϵ is a short distance that approaches zero.

At r = b (the current sheet),

$$H_\phi(b + \epsilon) - H_\phi(b - \epsilon) = J_z(b) \qquad 2.4a$$

$$H_z(b - \epsilon) - H_z(b + \epsilon) = J_\phi(b) \qquad 2.4b$$

$$E_\phi(b - \epsilon) = E_\phi(b + \epsilon)$$

$$E_z(b - \epsilon) = E_z(b + \epsilon)$$

At r=c (the conducting wall),

$$E_\phi(c) = 0.$$

$$E_z(c) = 0.$$

The boundary conditions conserve power flow through the various interfaces. The boundary conditions at the plasma-vacuum interface will be discussed in more detail in Sec. 6.

2.c) Boundary conditions including magnetization currents: The boundary conditions at the current sheet can be generalized to include jump conditions in the transverse electric field. This possibility may be accommodated by introducing the magnetization current, $\hat{M}$, (refer to Fig. 2.3b).

$$E_\phi(b - \epsilon) - E_\phi(b + \epsilon) = M_z(b) \qquad 2.4c$$

$$E_z(b + \epsilon) - E_z(b - \epsilon) = M_\phi(b) \qquad 2.4d$$

At the conducting wall, introduction of the magnetization current can conveniently represent flush-mounted wave guide feeds.

$$E_\phi(c) = M_z(c) \qquad 2.5a$$

$$E_z(c) = -M_\phi(c) \qquad 2.5b$$

Imposition of boundary conditions summarized in Eqs. 2.3 to 2.5 uniquely determines the field solution.

2.d) Axial boundary conditions: The Fourier integral transform of Eqs. 2.1 and 2.2 describes an open-ended system. If the integral transform is replaced by a Fourier sum, boundary conditions can be imposed at axial positions defined by $z = \pm L/2$. Two idealized sets of boundary conditions can be accommodated by a Fourier sum.[20] First, periodic boundary conditions can be imposed.

$$\vec{E}(z = -L/2) = \vec{E}(z = L/2) \qquad 2.6$$

These boundary conditions can be used to model wave propagation in small aspect ratio tokamaks. A second set of boundary conditions forces the axial electric field to be zero.

$$E_z(z = \pm L/2) = 0 \qquad 2.7$$

These boundary conditions have been found to model wave propagation in some open ended systems. The requirement imposed by Eq. 2.7 is equivalent to having all particles reflect at the boundaries at $(z = \pm L/2)$.

3. Equivalent Source Currents and the Induction Theorem

In the previous section, two electric and four magnetic source currents were defined by Eq. 2.4 and 2.5. In this section, it is shown that field solution of a general antenna can be constructed using the six current sources. The current sources are referred to as equivalent current sources since their use provides only a method of solution to the boundary value problem and no apparent physical reality.

3.a) The induction theorem: The induction theorem provides the connection between the equivalent source currents and the geometry of the actual antenna[21]. Referring to Fig. 3.1a, we observe a current source radiating in the presence of an obstacle and the fields $\vec{E}$ and $\vec{H}$ are to be calculated. The incident fields ($\vec{E}^i$, $\vec{H}^i$) are defined as the fields of the current source with the obstacle removed, Fig. 3.1b. Next, the scattered fields are defined as the difference fields.

$$\vec{E}^s = \vec{E} - \vec{E}^i, \qquad \vec{H}^s = \vec{H} - \vec{H}^i \tag{3.1}$$

From the above definitions, the scattered field is a source-free field external to the obstacle. Further, the total field, $\vec{E}$ and $\vec{H}$ is source-free inside the obstacle. The source-free fields can be supported in their respective domain by introducing surface currents on the obstacle.

$$\vec{J}_s = \vec{n} \times (\vec{H}^s - \vec{H}) \qquad \vec{M}_s = (\vec{E}^s - \vec{E}) \times \vec{n} \tag{3.2}$$

where $\vec{n}$ is an outward normal on the obstacle. Equation 3.2 is a result of the equivalance principle which briefly states that current sources may be introduced to support the tangential components of fields on surfaces. Since specification of the tangential components of the fields over a

Fig. 3.1 Induction Theorem

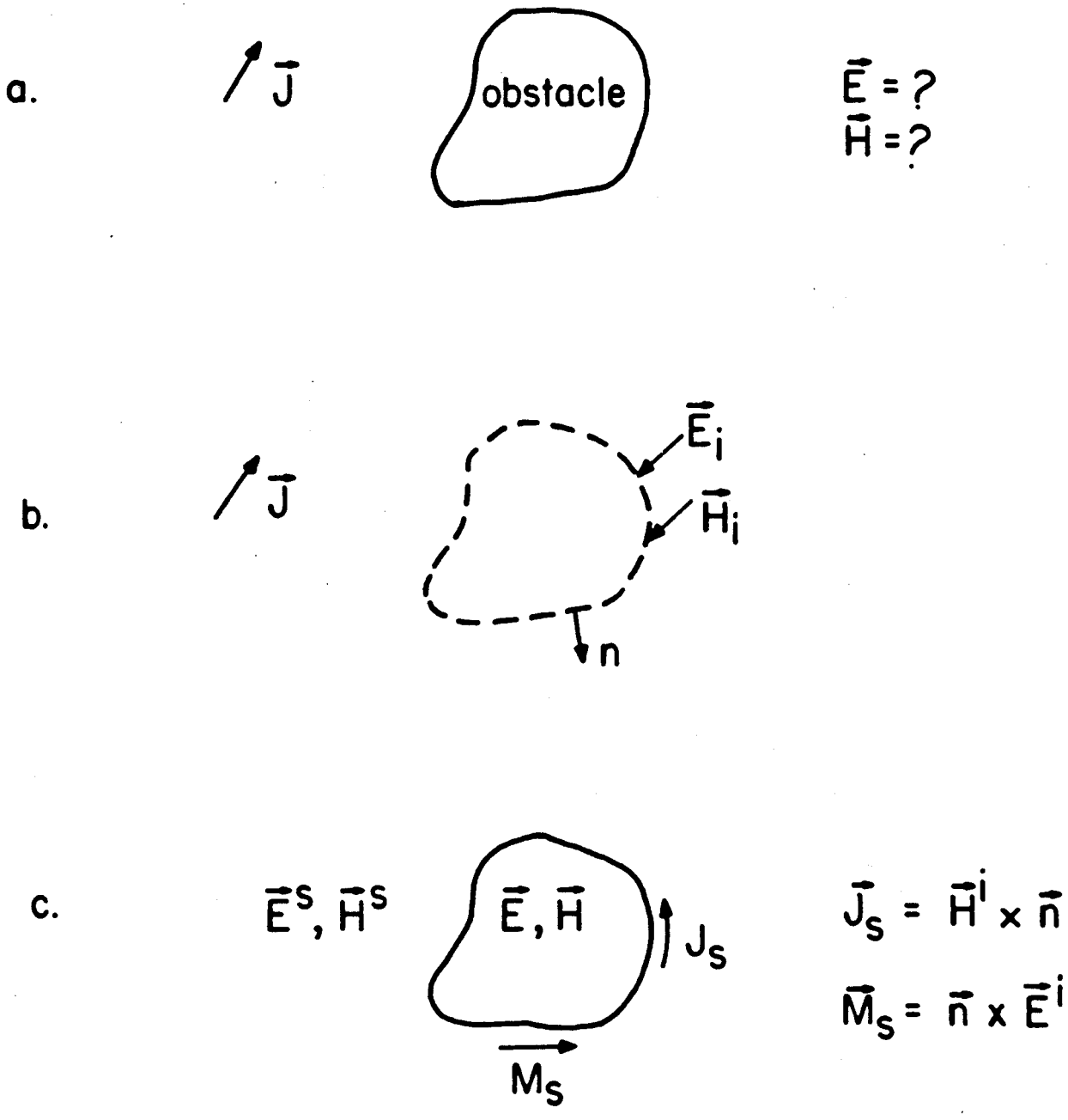

surface uniquely defines the field solution in the interior, the required current sources are also uniquely defined. Using Eq. 3.1 in Eq. 3.2, the surface currents of the obstacle are defined in terms of the incident fields.

$$\vec{J}_s = \vec{H}^i \times \vec{n} \qquad \vec{M}_s = \vec{n} \times \vec{E}^i \tag{3.3}$$

Comparing Figs. 3.1a and 3.1c, the original problem of a current source radiating in the presence of an obstacle has been replaced by a new problem of currents radiating from the surface of the obstacle. The generated fields are $\vec{E}$ and $\vec{H}$ interior to the obstacle and $\vec{E}^s$ and $\vec{H}^s$ exterior to the obstacle. The total fields outside the obstacle are given by the sum of incident and scattered fields.

$$\vec{E} = \vec{E}^i + \vec{E}^s$$

$$\vec{H} = \vec{H}^i + \vec{H}^s \tag{3.4}$$

Applying the induction theorem to the cylindrical antenna geometry of Fig. 1.2, we obtain the sequence of pictures diagrammed in Fig. 3.2. There are two obstacles present, the plasma column and the outer conducting vacuum tank. We enclose these obstacles with two cylindrical surfaces at r = b and r = c which also bound the radial extent of the antenna. The equivalent source currents to be calculated are $J_\phi(b)$, $J_z(b)$, $M_\phi(b)$, $M_z(b)$, $M_\phi(c)$, and $M_z(c)$ which radiate in the presence of the plasma and outer conducting tube. Note that the conducting tube shorts out the electric source currents at r = c. Only magnetization currents radiate from the surface of a perfect conductor. In terms of the incident fields from the antenna, the equivalent source currents are defined as follows:

Fig. 3.2 The Induction Theorem in Cylindrical Geometry

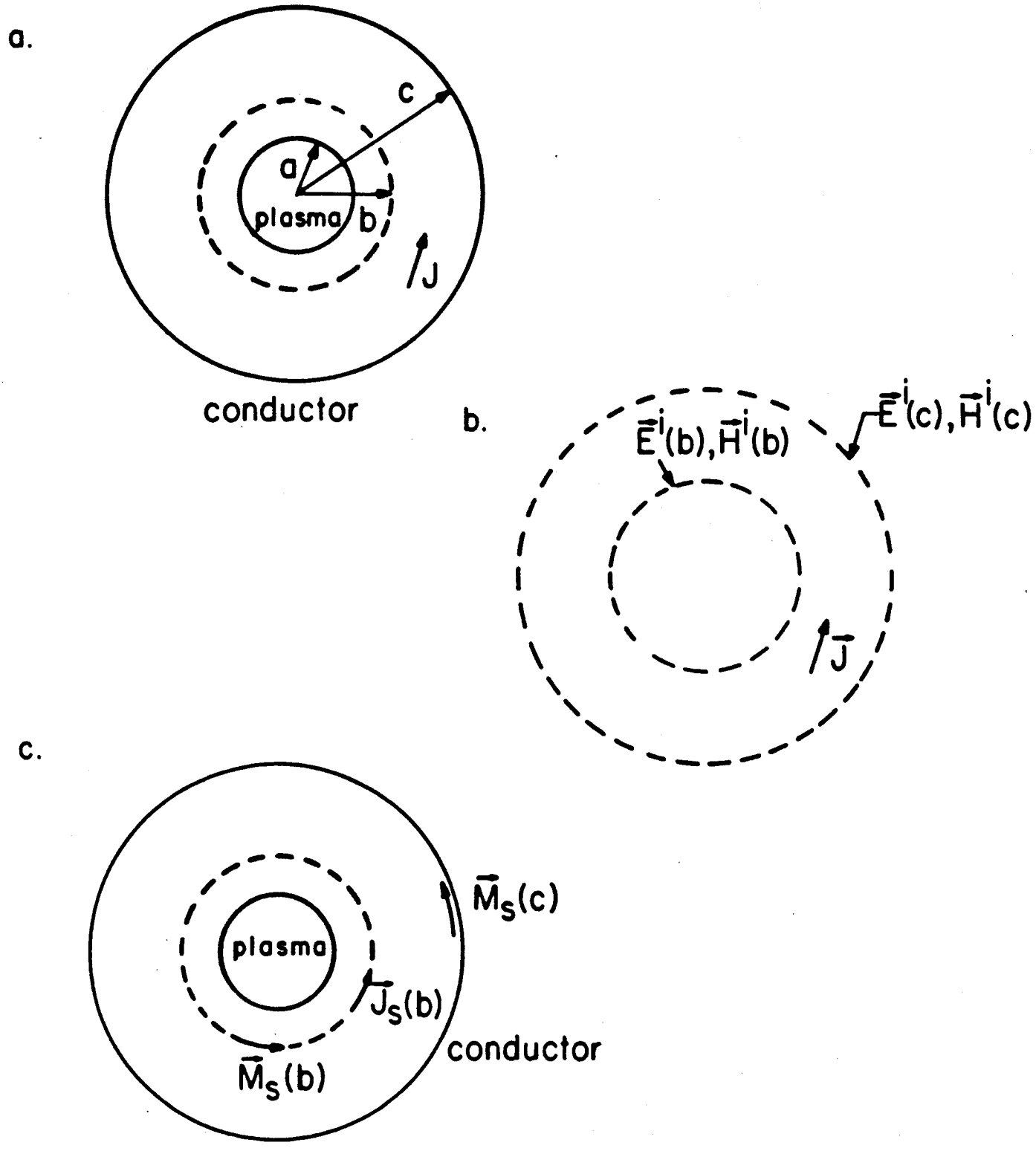

$$J_\phi(b, n, k_z) = H_z^i(b, n, k_z) \qquad 3.5a$$

$$J_z(b, n, k_z) = -H_\phi^i(b, n, k_z) \qquad 3.5b$$

$$M_\phi(b, n, k_z) = -E_z^i(b, n, k_z) \qquad 3.5c$$

$$M_z(b, n, k_z) = E_\phi^i(b, n, k_z) \qquad 3.5d$$

$$M_\phi(c, n, k_z) = E_z^i(c, n, k_z) \qquad 3.5e$$

$$M_z(c, n, k_z) = -E_\phi^i(c, n, k_z) \qquad 3.5f$$

The $n - k_z$ transform of the incident fields is required to define the source currents consistent with the current sheet representation in Sec. 2.

3.b) Equivalent source currents for the antennas of Fig. 1.1: Appendix C and D contain the details of the calculation of the equivalent source currents for the various antennas of Fig. 1.1. More detailed pictures of the various antenna configurations are contained in Appendix C. All of the antennas are assumed to be located at $z = \phi = 0$. For an antenna positioned at $z = z_o$ and $\phi = \phi_o$, the Fourier transforms calculated in Appendix C are multiplied by the factor $\exp(-ik_z z_o - in\phi_o)$.

4. Inductive Vacuum Fields

This section outlines the calculation of the vacuum fields for a given (n, k_z) mode.

4.a) Construction of the field solutions: The inductive vacuum fields refer to the electromagnetic field solution to the B.V.P. with the plasma removed (refer to Fig. 4.1). A calculation of the inductive vacuum fields is the first step in obtaining the E.M. field solution in the presence of plasma. We preface vacuum fields with "inductive" for the following reason. We have assumed a stationary current distribution ($\nabla \cdot \vec{J} = 0$) for the filamentary antennas of Fig. 1.1. The distribution of free charge along the antenna which would significantly contribute to the electric field in a vacuum has been neglected. The neglect of free charge on the antenna manifests itself in an electric field that has a non-zero tangential component on the surface of the antenna. However, in the stationary current approximation, the magnetic field is accurately calculated. Further, a thin surface layer of plasma or a Faraday shield will shield the electrostatic fields, due to free charge on the antenna, from the interior of the plasma.[20] In calculating the plasma fields, only the electric field associated with the time varying magnetic field via Faraday's law is significant in contributing to the total electric field. This electric field component is referred to as an inductive electric field. We note one antenna, the rectangular aperture, has an assumed distribution of free charge to meet the boundary condition tangential $\vec{E}$ being zero on the surface of the conductor.

The inductive vacuum field solution is constructed by writing down the source free field solution to Maxwell's equations in each of the three regions of Fig. 4.1. These fields are the well-known cylindrical waveguide

Fig. 4.1 Geometry of Vacuum Field Calculation

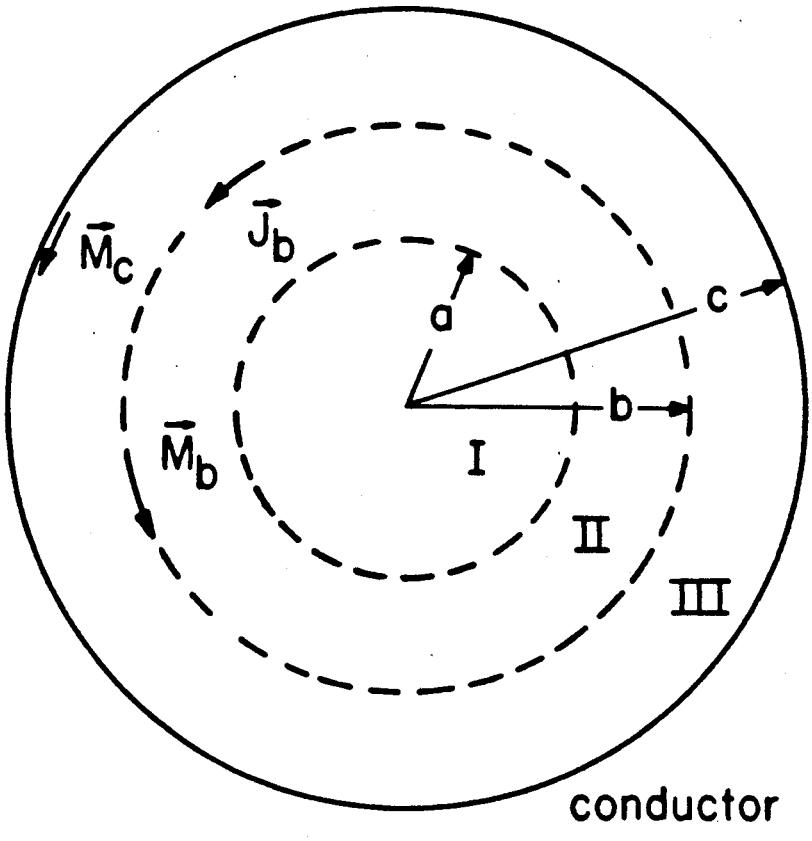

modes TE_z and TM_z (transverse electric and magnetic to the waveguide axis). The axial components, (H_z and E_z), satisfy the homogeneous Bessel's equation (Eqs. B.2 - B.4 of Appendix B), and the transverse field components are defined in terms of the axial fields (Eq. B.5). For the various regions of Fig. 4.1, the general field solutions for the axial fields have the form.

Region I:

$$H_z(r) = H_1^+ I_n(\nu r) \qquad 4.1a$$

$$E_z(r) = E_1^+ I_n(\nu r) \qquad 4.1b$$

Region II:

$$H_z(r) = H_2^+ I_n(\nu r) + H_2^- K_n(\nu r) \qquad 4.2a$$

$$E_z(r) = E_2^+ I_n(\nu r) + E_2^- K_n(\nu r) \qquad 4.2b$$

Region III:

$$H_z(r) = H_3^+ I_n(\nu r) + H_3^- K_n(\nu r) \qquad 4.3a$$

$$E_z(r) = E_3^+ I_n(\nu r) + E_3^- K_n(\nu r) \qquad 4.3b$$

In the above equations, it is assumed that $\nu^2 = k_z^2 - k_o^2 > 0$, and the radial variation of field quantities is expressed in terms of the modified Bessel functions which asymptotically have exponential behavior[22]. For $\nu^2 < 0$, Bessel functions of the first and second kind which asymptotically have sinusoidal behavior are used. In this case, we have the replacements,

$$J_n(\nu r) \rightarrow I_n(\nu r) \qquad 4.4a$$

$$Y_n(\nu r) \rightarrow K_n(\nu r) \qquad 4.4b$$

The ten unknown field amplitudes defined by Eqs. 4.1 to 4.3 are determined by imposition of the ten boundary conditions defined in Eqs. 2.3, 2.4a to d, and 2.5a and b. The axial components of the fields are given by the following expressions:

Region I:

$$H_z(r) = \frac{I_{nr}}{I_{nc'}} (h_1 + h_2 + h_3) \qquad 4.5a$$

$$E_z(r) = \frac{I_{nr}}{I_{nc}} (e_1 + e_2 + e_3) \qquad 4.5b$$

Region II:

$$H_z(r) = \frac{\Delta_{rc'}}{\Delta_{ac'}} H_z^a + \frac{\Delta_{ar}}{\Delta_{ac'}} (h_1 + h_2 + h_3) \qquad 4.6a$$

$$E_z(r) = \frac{\Delta_{rc}}{\Delta_{ac}} E_z^a + \frac{\Delta_{ar}}{\Delta_{ac}} (e_1 + e_2 + e_3) \qquad 4.6b$$

Region III:

$$H_z(r) = \frac{\Delta_{rc'}}{\Delta_{ac'}} H_z^a + \frac{\Delta_{rc'}}{\Delta_{ac'}} (h_4 + h_5) + \frac{\Delta_{ar}}{\Delta_{ac'}} h_6 \qquad 4.7a$$

$$E_z(r) = \frac{\Delta_{rc}}{\Delta_{ac}} E_z^a + \frac{\Delta_{rc}}{\Delta_{ac}} (e_4 + e_5) + \frac{\Delta_{ar}}{\Delta_{ac}} e_6 \qquad 4.7b$$

The excitation coefficients are defined by the following:

$$h_1 = -\nu b \, \Delta_{b'c'} J_\phi(b) \qquad 4.8a$$

$$h_2 = -i \, y_o \, \nu b \, \Delta_{bc'} M(b) \qquad 4.8b$$

$$h_3 = -i \, y_o \, M(c) \qquad 4.8c$$

where $$M(b) = \sigma_\nu M_z(b) + \frac{k_z}{\nu} \frac{n}{\nu b} M_\phi(b),$$

$$e_1 = -i \, z_o \, \nu b \, \Delta_{bc} J(b) \qquad 4.8d$$

$$e_2 = \nu b \, \Delta_{b'c} \, M_\phi(b) \qquad 4.8e$$

$$e_3 = -M_\phi(c) \qquad 4.8f$$

where $$J(b) = \sigma_\nu J_z(b) + \frac{k_z}{\nu} \frac{n}{\nu b} J_\phi(b),$$

$$h_4 = -\nu b \, \Delta_{ab'} \, J_\phi(b) \qquad 4.9a$$

$$h_5 = -i \, y_o \, \nu b \, \Delta_{ab} \, M(b) \qquad 4.9b$$

$$h_6 = -i \, y_o \, M(c) \qquad 4.9c$$

$$e_4 = -i \, z_o \, \nu b \, \Delta_{ab} \, J(b) \qquad 4.9d$$

$$e_5 = \nu b \, \Delta_{ab'} \, M_\phi(b) \qquad 4.9e$$

$$e_6 = -M_\phi(c) \qquad 4.9f$$

where $z_o = \nu/\omega\varepsilon_o$, $y_o = \nu/\omega\mu_o$, $\sigma_\nu = 1$ for $k_z > k_o$, $\sigma_\nu = -1$ for $k_z < k_o$, and in the above equations, a shorthand notation for Bessel functions and products of Bessel functions has been introduced. For example,

$$I_{nc} = I_n(\nu c) \qquad I_{nc'} = I_n'(\nu c)$$

$$\Delta_{ac'} = K_{na} \, I'_{nc} - K'_{nc} \, I_{na}$$

The other notation is defined in Appendix A. The symbols h_j and e_j are referred to as excitation coefficients that explicitly include the various source amplitudes ($J_\phi(b)$, $M_z(b)$, etc.), and the shielding of the nearby cylindrical vacuum tank (for example, terms such as $\Delta_{b'c'}$ in h_1). The symbols H_z^a and E_z^a are the field amplitudes at the boundary r = a.

Using the six boundary conditions outside r = a (Eqs. 2.4 and 2.5), the transverse to $\hat{a}_r$ fields at r=a can be expressed in terms of the two unknown wave amplitudes, H_2^+ and E_2^+,

$$H_z(r=a) = -\frac{\Delta_{ac'}}{K'_{nc}} H_2^+ + \frac{K_{na}}{K'_{nc}} (h_1 + h_2 + h_3) \qquad 4.10a$$

$$E_z(r=a) = -\frac{\Delta_{ac}}{K_{nc}} E_2^+ + \frac{K_{na}}{K_{nc}} (e_1 + e_2 + e_3) \qquad 4.10b$$

$$H_\phi(r=a) = -\frac{i\omega\varepsilon_o}{\nu} E'_z(r=a) + \frac{k_z}{\nu}\frac{n}{\nu a} H_z(r=a) \qquad 4.10c$$

$$E_\phi(r=a) = \frac{k_z}{\nu}\frac{n}{\nu a} E_z(r=a) + \frac{i\omega\mu_o}{\nu} H'_z(r=a) \qquad 4.10d$$

Prescribing $H_z(r=a) = H_z^a$ and $E_z(r=a) = E_z^a$, the fields outside r=a are explicitly given in terms of the excitation coefficients and the field amplitudes H_z^a and E_z^a (refer to Eqs. 4.6 and 4.7). When Region I is filled with plasma, Eqs. 4.6 and 4.7 remain unchanged, and the plasma reaction back on the antenna is contained in H_z^a and E_z^a. These field amplitudes can be generally thought of as the scattered fields out of Region I. For a vacuum, E_z^a and H_z^a are evaluated by Eq. 4.5 with r=a.

5. The Plasma Response

This section outlines a calculation of the linearized self-consistent current response of the plasma for a given (n, k_z) wave mode and discusses the various wave modes of the ICRF.

5.a) A calculation of the induced plasma currents: The electromagnetic fields from the antenna induce perturbed currents in the plasma. The plasma currents are calculated by determining the perturbed distribution function from the linearized Vlasov equation and integrating over velocity space.[23] The linearized, collisionless Vlasov equation has the form,

$$\frac{\partial f_1}{\partial t} + \vec{v} \cdot \frac{\partial f_1}{\partial \vec{r}} + (\vec{v} \times \vec{\omega}_{co}) \cdot \frac{\partial f_1}{\partial \vec{v}} = -\frac{q}{m} (\vec{E}_1 + \vec{v} \times \vec{B}_1) \cdot \frac{\partial f_o}{\partial \vec{v}} \qquad 5.1$$

where the subscript 1 indicates perturbed quantities, and f_o is the equilibrium distribution function. By the method of characteristics, the solution to Eq. 5.1 may be written dowm immediately.

$$f_1(\vec{r}, \vec{v}, t) = -\frac{q}{m} \int_{t-T}^{t} \vec{E}_1(\vec{r}', t') \cdot \frac{\partial f_o(\vec{v}')}{\partial \vec{v}'} \, dt' \qquad 5.2$$

In Eq. 5.2, the perturbed distribution function at $t' = t - T$ is assumed to be zero, and the equilibrium distribution function is assumed to be isotropic. The integration in Eq. 5.2 is performed along the characteristics or unperturbed trajectories of the particles. These trajectories are determined by the equilibrium confining field.

$$\vec{B}(\vec{r}) = B(r) \, \hat{a}_z$$

The characteristics have the form,

$$x' = x - v_x/\omega_c \sin(\omega_c \tau) + v_y/\omega_c (1 - \cos \omega_c \tau) \quad 5.3a$$

$$y' = y - v_x/\omega_c (1 - \cos \omega_c \tau) - v_y/\omega_c \sin(\omega_c \tau) \quad 5.3b$$

$$z' = z - v_z \tau \quad 5.3c$$

where $\tau = t - t'$ and $\omega_c = q\, B(r)/m$. In the unperturbed orbits, spatial dispersion in the transverse direction has been neglected. This is valid providing the gyro-radius is small compared to the scale length of variation of the magnetic field ($\rho_i/L_B \ll 1$).

In order to integrate Eq. 5.2 along the characteristics defined in Eq. 5.3, an explicit form of the electric field and the equilibrium distribution function is adopted. The equilibrium distribution function is assumed to be a local Maxwellian.

$$f_o(r, v) = n(r)\, \pi^{-3/2}\, v_\alpha^{-3}\, e^{-v^2/v_\alpha^2} \quad 5.4$$

where $v_\alpha^2 = \frac{2kT(r)}{m_i}$. For the electric field, a Taylor series expansion is used in the transverse directions, and an $e^{ik_z z'}$ dependence is assumed along the confining magnetic field. The Taylor series expansion is assumed to have the form,

$$\vec{E}(\vec{r}') = \vec{E}(\vec{r}) + (\vec{r}' - r) \cdot \nabla_t \vec{E}(\vec{r}) + \frac{(\vec{r}' - \vec{r})^2}{2} : \nabla_t \nabla_t \vec{E}(\vec{r}) \quad 5.5a$$

where $\vec{r}$ is a fixed position in space, and $\vec{r}'$ is the unperturbed trajectory of the particle. A local approximation is made,

$$\vec{E}(\vec{r}') = \vec{E}(r, \phi)\, e^{ik_z z'} \qquad 5.5b$$

The neglect of higher order terms in the expansion of the electric field is justified, providing,

$$\rho^i / L_E << 1 \qquad 5.6a$$

where L_E is the scale length of variation of the "wave" or perturbing electric field. It should be noted that derivative terms in Eq. 5.5a, generate additional plasma waves that are important near the harmonics of the cyclotron frequency (ion Bernstein waves). The inequality in Eq. 5.6a is supplemented with the further requirement,

$$\omega \neq n\omega_{ci} \qquad n = 2, 3, \text{ etc.} \qquad 5.6b$$

for the local approximation to be justified. Using Eqs. 5.3, 5.4 and 5.5b, the perturbed distribution function can be calculated using Eq. 5.2. Velocity moments of the perturbed distribution function define a local conductivity tensor which is related to an equivalent dielectric tensor that includes the free space displacement current ($\epsilon_o\, d\vec{E}/dt$).

$$\overleftrightarrow{\epsilon} = 1 + \frac{i\overleftrightarrow{\sigma}}{\omega\epsilon_o} \qquad 5.7a$$

Using Eq. 5.7, Ampere's law has the simple form,

$$\nabla \times \vec{H} = -i\omega\epsilon_o \overleftrightarrow{\epsilon} \cdot \vec{E} \qquad 5.7b$$

The dielectric tenor has the form,

$$\overleftrightarrow{\epsilon} = \begin{bmatrix} S & -iD & 0 \\ iD & S & 0 \\ 0 & 0 & P \end{bmatrix} \qquad 5.8$$

$$S = \frac{1}{2}(R + L) \qquad D = \frac{1}{2}(R - L) \qquad 5.8a$$

$$R = 1 + \sum_\alpha \frac{\omega_{p\alpha}^2}{\omega k_z v_\alpha} Z(\zeta_1) \qquad 5.8b$$

$$L = 1 + \sum_\alpha \frac{\omega_{p\alpha}^2}{\omega k_z v_\alpha} Z(\zeta_{-1}) \qquad 5.8c$$

$$P = 1 - \sum_\alpha \frac{\omega_{p\alpha}^2}{(k_z v_\alpha)^2} Z'(\zeta_o) \qquad 5.8d$$

$$\zeta_n = \frac{\omega + n\omega_{c\alpha}}{k_z v_\alpha} \qquad 5.8e$$

The plasma response defined by Eq. 5.8 assumes no collisions and a steady-state has been reached where t - T (the time of turn on of the electric field) approaches negative infinity. Collisions may be modelled in an approximate form by using a particle conserving Krook model.[24] In this model, the additional terms;

$$-\nu f_1 + \nu \frac{n_1}{n_o} f_o \qquad 5.9a$$

are added to the right-hand side of Eq. 5.1. In Eq. 5.9a, n_1 and n_o are the perturbed density, and equilibrium density, respectively. For the particle conserving Krook model, the dielectric tensor has the same form as Eq. 5.8 with the replacements,

$$\zeta_n = \frac{\omega + i\nu_\alpha + n\omega_{c\alpha}}{k_z v_\alpha} \qquad 5.9b$$

and

$$P = 1 - \sum_\alpha \frac{\omega_{p\alpha}^2}{(k_z v_\alpha)^2} \frac{Z'(\zeta_o)}{1 + \frac{i\nu_\alpha}{k_z v_\alpha} Z(\zeta_o)} \qquad 5.9c$$

Use of the collisional form of the equivalent dielectric tensor improves the numerical convergence of the inverse transform of Eq. 2.1.

5.b) ICRF wave modes: The form of the equivalent dielectric tensor and Maxwell's equations determine the characteristic modes or waves in the plasma. The wave propagation characteristics can be investigated by assuming a plane wave field variation.

$$\vec{E}(x, z) = \vec{E}_o \, e^{ik_x x + ik_z z} \qquad 5.10$$

Use of Eq. 5.10 in Eq. 5.7b and Eq. 6.1a, results in the following set of equations satisfied by the components of $\vec{E}_o$, and a dispersion relation.

$$\begin{bmatrix} k_o^2 S - k_z^2 & -ik_o^2 D & k_x k_z \\ ik_o^2 D & k_o^2 S - k_z^2 - k_x^2 & 0 \\ k_x k_z & 0 & k_o^2 P - k_x^2 \end{bmatrix} \begin{bmatrix} E_{xo} \\ E_{yo} \\ E_{zo} \end{bmatrix} = 0 \qquad 5.11a$$

$$Sk_x^4 + [k_z^2(S + P) - k_o^2(SP + RL)]\, k_x^2 + P(k_o^2 R - k_z^2)(k_o^2 L - k_z^2) = 0 \qquad 5.11b$$

The wave modes in the plasma can be discussed in the context of Eqs. 5.11a and b.

The quadratic dispersion relation of Eq. 5.11b has the following approximate roots providing $k_z^2 \neq k_o^2 S$.

$$k_{r1}^2 \approx \frac{(k_o^2 R - k_z^2)(k_o^2 L - k_z^2)}{(k_o^2 S - k_z^2)} \qquad 5.12a$$

$$k_{r2}^2 = \frac{P}{S}(k_o^2 S - k_z^2) \qquad 5.12b$$

For plasma parameters of interest ($P \gg R, L, S$), the above wave numbers define a fast wave branch (k_{r1}) and a slow wave branch (k_{r2}). The fast

magnetosonic wave is on the fast branch and has the following dispersion relation for propagation perpendicular to $\vec{B}_o$.

$$k_{r1} \backsim k_o \sqrt{\frac{RL}{S}} \backsim \frac{\omega_{pi}}{c} \frac{\omega}{\omega_{ci}} \qquad 5.13a$$

The fast wave may be efficiently excited when the perpendicular wavelength defined by Eq. 5.13a is comparable to the plasma radius. The exception to this is the n=1 fast wave (refer to Sec. 7). The wavelength of the fast wave is inversely proportional to the frequency and the square root of the density. For $\omega = \omega_{ci}$, the fast wave is circularly polarized in the right-hand sense; and for a finite value of k_z, this mode has a right-hand cut-off defined by $k_z^2 = k_o^2 R$. Below the ion cyclotron frequency, the ion cyclotron wave propogates along $\vec{B}_o$ with the approximate dispersion relation;

$$k_z^2 = k_o^2 L \qquad 5.14a$$

The ion cyclotron wave is left-hand polarized (i.e., in the sense of ion rotation), and there is a k_z window in which the wave propagates;

$$k_o^2 S \leq k_z^2 \leq k_o^2 L \qquad 5.14b$$

The lower bound in Eq. 5.14b defines the perpendicular ion cyclotron resonance where from Eq. 5.12a, $k_{r1} \rightarrow \infty$. In reality at this value of k_z, the fast and slow branches defined in Eq. 5.12 are coupled via Eq. 5.11b. The propagation characteristics on the slow branch are strongly dependent

upon the ratio of the parallel to $\vec{B}_o$ phase velocity compared to the electron thermal velocity. For $\omega/k_z >> v_e$

$$k_{r2}^2 \simeq -\frac{\omega_{pe}^2}{\omega^2}\frac{(k_o^2 S - k_z^2)}{S} \qquad 5.15a$$

and for $\omega/k_z << v_e$

$$k_{r2}^2 \simeq \frac{2\omega_{pe}^2}{k_z^2 v_e^2}\frac{(k_o^2 S - k_z^2)}{S} \qquad 5.15b$$

The cold plasma slow wave defined by 5.15a propagates for $\omega < \omega_{ci}$, and for $k_z^2 > k_o^2 S$. It has a polarization that couples it to the ion cyclotron wave near $k_z^2 \gtrsim k_o^2 S$. For $k_z=0$, the cold plasma slow wave is evanescent with an electric field polarized along $\vec{B}_o$, (similar to ECH o-mode), and a skin depth given by c/ω_{pe}. The slow wave defined by Eq. 5.15b propagates for $k_z^2 < k_o^2 S$ and $\omega < \omega_{ci}$. The mode is the higher frequency extension of the kinetic Alfven wave.

6. The Plasma Fields Using a Cylindrically Stratified Model

This section contains a general description of the numerical method (a stratified model) used to obtain the plasma fields for a given (n, k_z) wave mode; a calculation of the fields in a uniform strata; an analysis that interconnects the field solutions in all the strata; and defines various quantities of interest such as power flow, etc.

6.a) A general description of the numerical method: The plasma fields are obtained by solving the time harmonic form of Maxwell's equations with the imposition of appropriate boundary conditions.

$$\nabla \times \vec{E} = i\omega\mu_o \vec{H} \qquad 6.1a$$

$$\nabla \times \vec{H} = -i\omega\epsilon_o \overleftrightarrow{\epsilon}(r) \cdot \vec{E} \qquad 6.1b$$

The equivalent dielectric tensor is defined by Eq. 5.8, and the plasma parameters are assumed to be only a function of the radial coordinate. The requirement of the continuity of transverse electric and magnetic fields at the plasma-vacuum interface are imposed as boundary conditions (Eq. 2.3).

$$\Delta E_\phi(a) = \Delta E_z(a) = \Delta H_\phi(a) = \Delta H_z(a) = 0 \qquad 6.1c$$

$$\Delta f(a) = \lim_{\epsilon \to 0} [f(a + \epsilon) - f(a - \epsilon)]$$

The numerical scheme used to construct a solution to Eqs. 6.1a - c is the finite element method. The continuous variation of the plasma

parameters and consequently the dielectric elements, is replaced by a step-wise variation as diagrammed in Fig. 6.1. The step-wise profile is referred to as a stratified profile, and for each strata, a spatially uniform plasma has been assumed. Thus, Maxwell's equations can be solved assuming a uniform plasma.

$$\nabla \times \vec{H} = -i\omega\epsilon_o \overleftrightarrow{\epsilon}_j \cdot \vec{E} \qquad 6.1d$$

where $\overleftrightarrow{\epsilon}_j$ is a constant dyadic for the "j th" strata. The only question that remains is the connection of the solutions between adjacent strata.

The implications of the boundary conditions defined by Eq. 6.1c, and the validity of the above numerical scheme in obtaining the correct solution to Eq. 6.1 can be addressed by using the Poynting theorem associated with Eqs. 6.1a and b.

$$\int_S \vec{E} \times \vec{H}^* \cdot d\vec{s} + \int_V [i\omega\epsilon_o \vec{E} \cdot \overleftrightarrow{\epsilon}^* \cdot \vec{E}^* - i\omega\mu_o |\vec{H}|^2] \, dV = 0 \qquad 6.2a$$

For the geometry under consideration, the surface integral is performed over a cylindrical tube of inner and outer radius of r_{i-1} and r_i, (or 0 and a).

$$\int_S \vec{E} \times \vec{H}^* \cdot d\vec{s} = \Big|_{r_{i-1}}^{r_i} [E_\phi H_z^* - E_z H_\phi^*] \qquad 6.2b$$

The volume integral can be written in component form using the rotating field components E_+ and E_- ($E_\pm = E_x \pm iE_y$).

$$\int_V \left\{ i\omega\epsilon_o [L^*/2 \, |E_+|^2 + R^*/2 \, |E_-|^2 + P^* |E_z|^2] - i\omega\mu_o |\vec{H}|^2 \right\} dv \qquad 6.2c$$

Fig. 6.1 Plasma Profiles

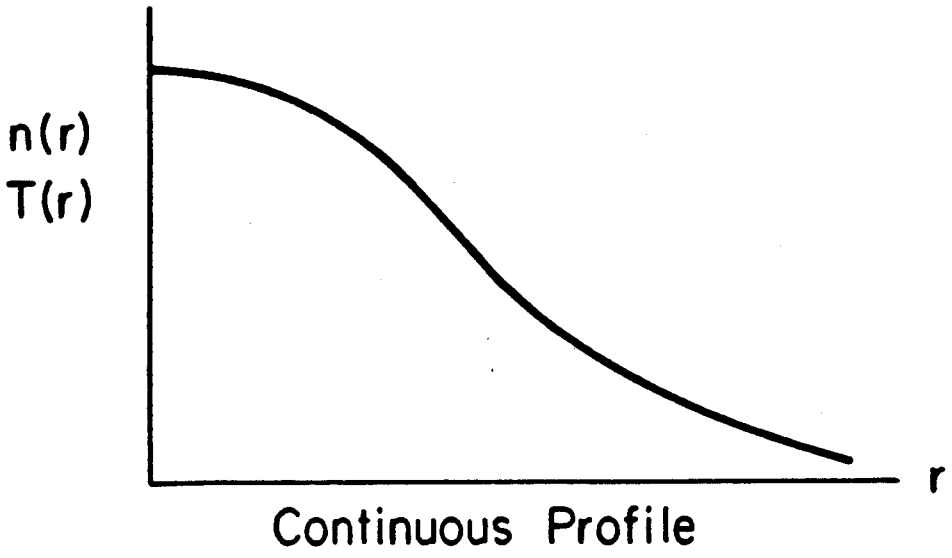

Continuous Profile

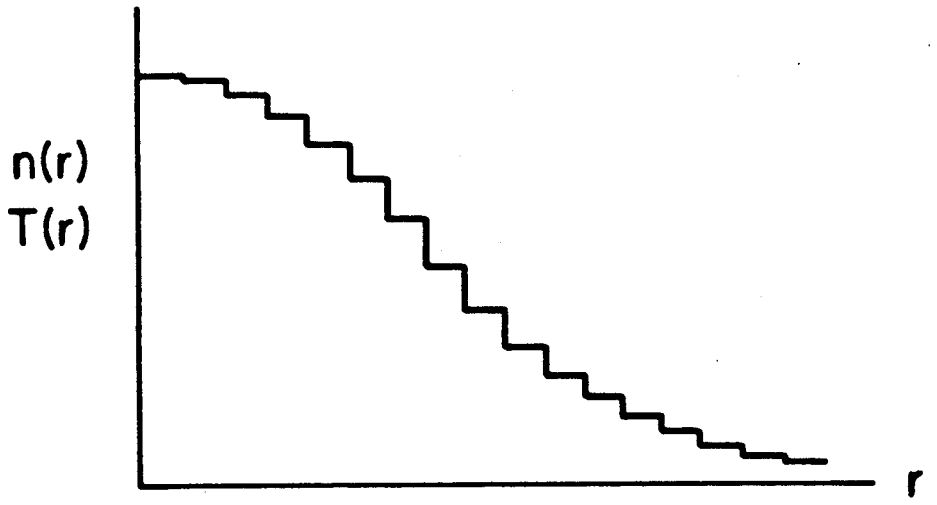

Stratified Profile

The boundary conditions of Eq. 6.1c provide a unique solution to Maxwell's equations over the domain $r \leq a$, if the plasma is dissipative. To show this, consider two separate solutions to Eqs. 6.1a - c, $\vec{E}_1$ and $\vec{E}_2$; and the difference solution $\vec{E}_d = \vec{E}_1 - \vec{E}_2$. For a unique solution it must be shown that $\vec{E}_d \equiv 0$ everywhere in V ($r \leq a$). The difference field satisfies Poynting's theorem. Further, if we require that both $\vec{E}_1$ and $\vec{E}_2$ are equal to prescribed values of E_ϕ, E_z, H_ϕ, H_z at $r = a$; the surface integral vanishes for the difference fields, and the volume integral (Eq. 6.2c) is identically zero. For a Maxwellian plasma (i.e., a dissipative system), the real part of Eq. 6.2c is positive definite unless $|\vec{E}_d| \equiv 0$ everywhere in V. Thus, the boundary conditions Eq. 6.1c (or Fig. 2.3) define a unique solution in the interior of the plasma $r \leq a$. It is also recognized that the Poynting theorem is a power conservation relation, and the boundary conditions preserve power flow through the plasma-vacuum interface.

Poynting's theorem, derived directly from Maxwell's equations, can be viewed as a variational principle for calculating the fields. An approximate solution defined by, $\vec{E} = \vec{E}_o + \delta\vec{e}$, is stationary about the exact solution $\vec{E}_o$. Designating Eq. 6.2c as $J(\vec{E})$ and substitution of the approximate solution, the previous statement is verified.

$$\frac{\partial J}{\partial \delta} = \int_V \vec{e}^* \cdot [\nabla \times \nabla \times \vec{E}_o - k_o^2 \, \epsilon \cdot \vec{E}_o] \, dV \equiv 0 \qquad 6.3$$

Thus, a numerical solution that renders J stationary provides a good approximation to the exact solution.

Next, consider the stratified profile (Fig. 6.1b) as an approximation to the continuous profile. Poynting's theorem can be applied to each of the individual strata and the result summed. An obvious simplification occurs if we assume the following boundary conditions at the interface between strata.

$$\Delta E_\phi(r_i) = \Delta E_z(r_i) = \Delta H_\phi(r_i) = \Delta H_z(r_i) = 0 \qquad 6.4$$

$$\Delta f(r_i) = \lim_{\epsilon \to 0} [f(r_i + \epsilon) - f(r_i - \epsilon)]$$

Again, Eq. 6.4 has the practical implication of conserving power through the interface between adjacent strata. The Poynting theorem for the stratified profile has the form;

$$\int_{r=a} \vec{E} \times \vec{H}^* \cdot \hat{a}_r \, ds + \sum_{j=1}^{m_s} \int_{V_i} [i\omega\epsilon_o \vec{E} \cdot \overleftrightarrow{\epsilon}^* \cdot \vec{E}^* - i\omega\mu_o |\vec{H}|^2] \, dV_j \qquad 6.5$$

where m_s is the number of strata in the profile. Two observations can be made from Eq. 6.5. First, following the previous arguments, Eq. 6.1a, c, d and boundary conditions Eq. 6.4 define a unique solution to the boundary value problem that uses a stratified profile. Second, as $m_s \to \infty$, Eq. 6.5 is identical to Eq. 6.2 which can be viewed as a variational principle for the continuous profile case. The field solution to the stratified profile approaches the exact field solution for the continuous profile as $m_s \to \infty$. Thus, the stratified profile provides an approximate solution to Maxwell's equations (Eq. 6.1a and b) which include continuous inhomogeneous plasma profiles.

Constructing a field solution from a stratified profile has a strong physical attraction. Viewing the plasma as locally homogeneous, the familiar wave modes of uniform plasma theory can be identified. In particular, the dispersion relations at the end of the previous section and in the next section can be used to interpret the results of numerical solutions of the total fields. A discussion of the numerical efficiency of the stratified profile will be presented at the end of the Sec. 7.

6.b) Field solution in a uniform strata: The field solution in a strata of uniform plasma parameters is calculated[25]. In analogy with the vacuum case, the field solution can be expressed in terms of modes nearly TE_z and TM_z. This division is exact for perpendicular propagation of the waves ($k_z \equiv 0$).

Nearly TE_z modes, fast modes

$$\frac{d^2}{dr^2} H_{z1} + \frac{1}{r}\frac{d}{dr} H_{z1} + \left[k_{r1}^2 - \frac{n^2}{r^2}\right] H_{z1} = 0 \qquad 6.6a$$

$$E_{z1} = z_1 H_{z1} \qquad 6.6b$$

$$z_1 = \frac{i\omega\mu_o k_z D}{P(k_z^2 - k_o^2 S) + k_{r1}^2 S} \qquad 6.6c$$

Nearly TM_z modes, slow modes

$$\frac{d^2}{dr^2} E_{z2} + \frac{1}{r}\frac{d}{dr} E_{z2} + \left[k_{r2}^2 - \frac{n^2}{r^2}\right] E_{z2} = 0 \qquad 6.7a$$

$$H_{z2} = y_2 E_{z2} \tag{6.7b}$$

$$y_2 = \frac{-i\omega\epsilon_o k_z PD}{S(k_{r2}^2 + k_z^2) - RLk_o^2} \tag{6.7c}$$

The total axial fields are given by,

$$H_z = H_{z1} + y_2 E_{z2} \tag{6.8a}$$

$$E_z = z_1 H_{z1} + E_{z2} \tag{6.8b}$$

The radial wave numbers are defined by,

$$S\,k_{ri}^4 + k_{ri}^2\,[k_z^2(S + P) - k_o^2(SP + RL)] + P(k_z^2 - k_o^2 R)\,(k_z^2 - k_o^2 L) = 0 \tag{6.9}$$

which is the same as Eq. 5.11b. The smaller root (k_{r1}) of Eq. 6.9 is labeled as the fast mode or the nearly TE_z mode, and the larger root (k_{r2}) labeled as the slow mode or the nearly TM_z mode. The transverse plasma fields E_r, E_ϕ, H_r, and H_ϕ are defined in terms of the axial components. The relations are contained in Appendix E, Eqs. E.1 to 8.

The axial field components $H_{z1}(r)$ and $E_{z2}(r)$ each separately satisfy Bessel's equation and define radially propagating modes with wave numbers

k_{r1} and k_{r2}, respectively. The solution to 6.6a for the "j th" strata is written as,

$$H_{z1}(j) = A_{2j-1}\, H_1^n[k_{r1}(j)\, r] + A_{2j}\, H_2^n[k_{r1}(j)\, r] \qquad 6.10a$$

where (j) designates $r_{j-1} < r < r_j$ where r_j defines the outer boundary of the "j th" strata. Similarly, the solution to Eq. 6.7a is,

$$E_{z2}(j) = B_{2j-1}\, H_1^n[k_{r2}(j)\, r] + B_{2j}\, H_2^n[k_{r2}(j)\, r] \qquad 6.10b$$

The functions H_1^n and H_2^n represent the two independent solutions to Bessel's equation. The above notation implies the two Hankel functions as solutions; however, J_n and Y_n are also valid solutions and for small arguments, these functions are used to provide the numerically distinct solutions. Asymptotically,

$$H_1^n(kr) \sim e^{ikr}, \qquad H_2^n(kr) \sim e^{-ikr} \qquad 6.11$$

so the two independent solutions may be viewed as inward and outward radially propagating waves.

6.c) Interconnection between strata: With reference to Fig. 6.2, in each cylindrical strata four independently propagating modes are present with the exception of the innermost cylinder. The requirement that the solution be regular at the origin implies, $H_2^n(kr) = J_n(kr)$ and

Fig. 6.2 Waves in a Uniform Strata

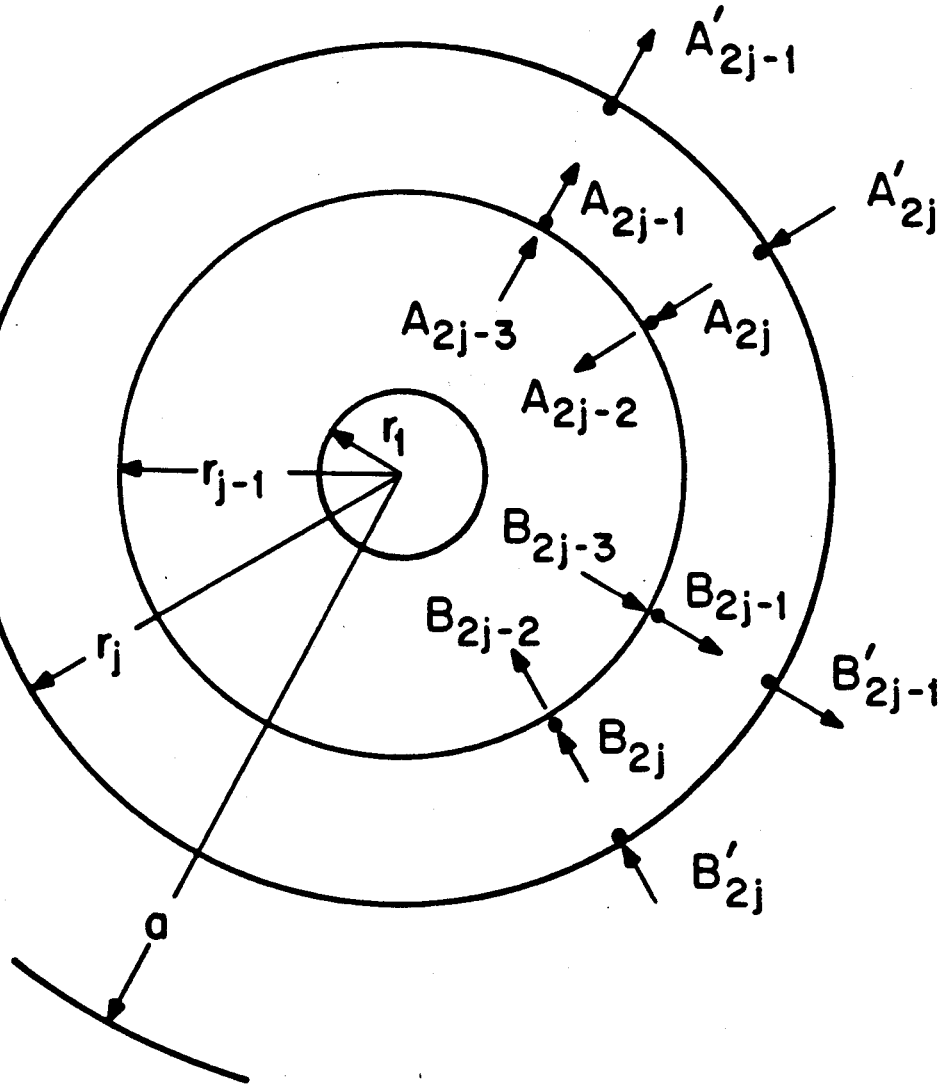

$$A_1 = B_1 = 0 \qquad 6.12$$

For m strata, and including the eight unknown field amplitudes for the vacuum fields, there are a total of 4 m + 8 unknowns. The six vacuum boundary conditions (Eq. 2.4 and 2.5), m times the 4 boundary conditions at the strata interface (Eq. 6.4) and Eq. 6.12 provide 4 k + 8 constraints that are used to determine the wave amplitudes throughout the system. Scattering parameters (S-parameters) or addition formulas are used to relate field amplitudes in adjacent strata (refer to Fig. 6.2)[26]. Each strata represents a two-port network where the outgoing wave amplitudes (i.e., the scattered fields) are defined in terms of the incoming waves. For the interface between the j and j-1 strata, we have,

$$\vec{O}_{j-1} = [S^j]\ \vec{I}_j \qquad 6.13a$$

where the incoming and outgoing wave four-component vectors are given by,

$$\vec{I}_j = \begin{bmatrix} A_{2j-3} \\ A_{2j} \\ B_{2j-3} \\ B_{2j} \end{bmatrix} \qquad \vec{O}_j = \begin{bmatrix} A_{2j-2} \\ A_{2j-1} \\ B_{2j-2} \\ B_{2j-1} \end{bmatrix} \qquad 6.13b$$

and the scattering matrix is a 4 × 4 matrix with elements $S_{k\ell}$ ($k = 1, 4$, $\ell = 1, 4$). The elements of the scattering matrix are defined by the four

simultaneous equations generated by imposing the boundary conditions of Eq. 6.4 at the interface $r=r_{j-1}$ between the "j-1" and "j th" strata. Explicit expressions for the transverse fields E_ϕ and H_ϕ in terms of the wave amplitudes are given by Eqs. E.4b and E.4d. S-parameters are used so that exponentially growing or decaying waves can be accommodated without a loss of accuracy. If the exponential factor exp [ik(j)r] is factored from the amplitude of a wave in the "j th" strata, the wave amplitudes at $r = r_{j-1}$ (A_{2j}) and at r_j (A'_{2j}) are connected through the relations (refer to Fig. 6.2).

$$
\begin{aligned}
A'_{2j-1} &= e^{ik_{r1}(j)\,\Delta} A_{2j-1} \\
A_{2j} &= e^{ik_{r1}(j)\,\Delta} A'_{2j} \\
B'_{2j-1} &= e^{ik_{r2}(j)\,\Delta} B_{2j-1} \\
B_{2j} &= e^{ik_{r2}(j)\,\Delta} B'_{2j}
\end{aligned}
\qquad 6.14
$$

where $\Delta = r_j - r_{j-1}$. Relations defined by Eqs. 6.13 and 6.14 provide a connection between wave amplitudes at $r_{j-1} - \epsilon$ and $r_j - \epsilon$ where $\epsilon \to 0$.

Using the relations for cascading two-port networks characterized by a scattering matrix, a composite s-matrix, S, a can be obtained that relates field amplitudes in the innermost strata to those at the plasma edge, r=a (refer to Fig. 6.3a).

Fig. 6.3 Composite S matrices

a. S matrices for the fields at $r=r_1, a$

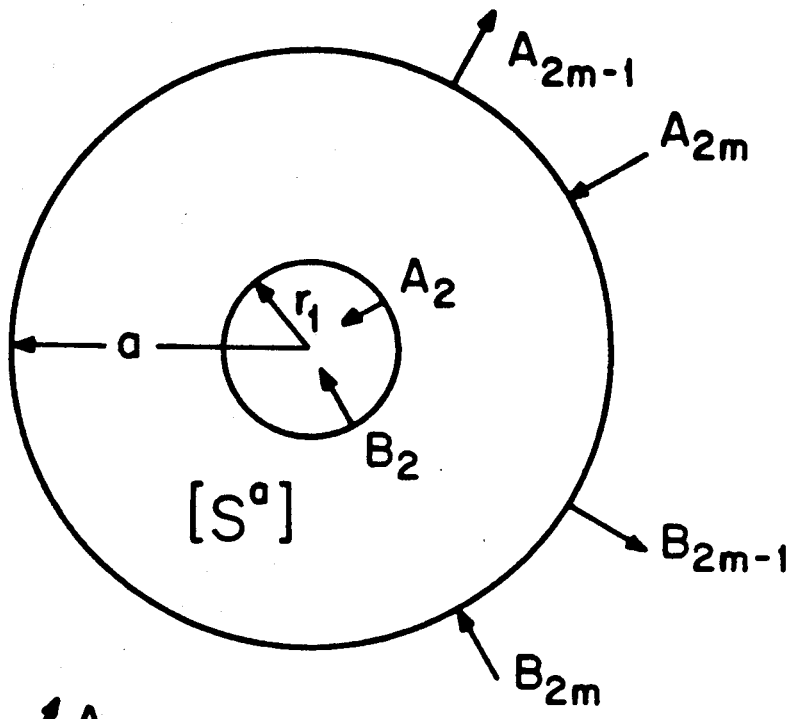

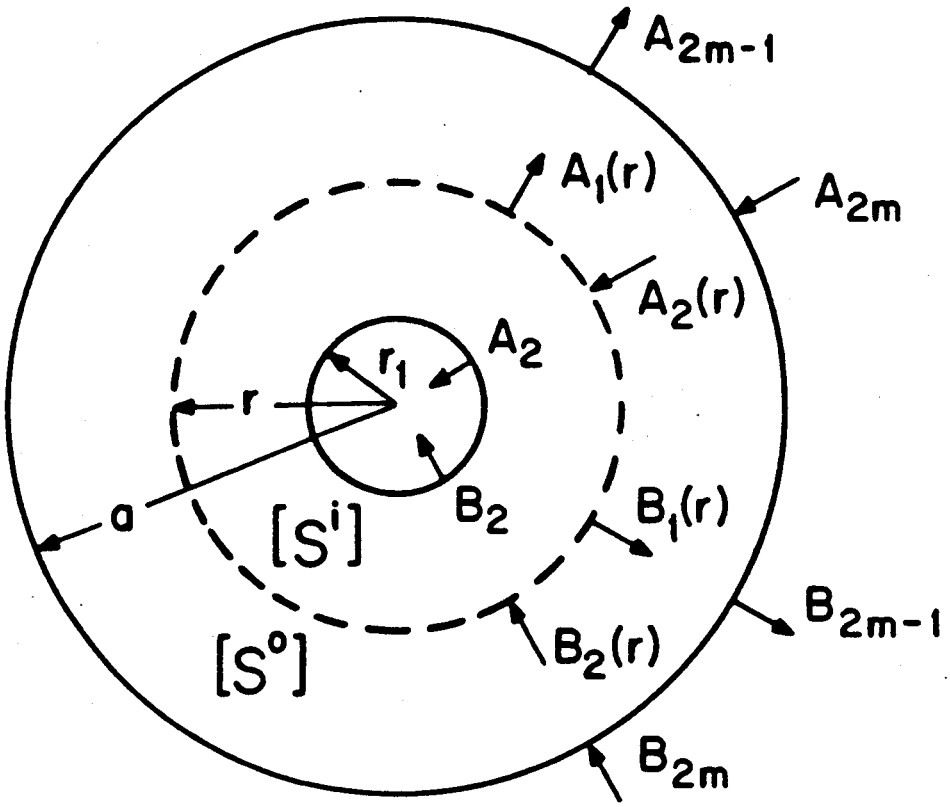

b. S matrices for the field at r

$$A_2 = S^a_{12}\, A_{2m} + S^a_{14}\, B_{2m} \qquad 6.15a$$

$$B_2 = S^a_{32}\, A_{2m} + S^a_{34}\, B_{2m} \qquad 6.15b$$

$$A_{2m-1} = S^a_{22}\, A_{2m} + S^a_{24}\, B_{2m} \qquad 6.15c$$

$$B_{2m-1} = S^a_{42}\, A_{32} + S^a_{44}\, B_{2m} \qquad 6.15d$$

where m is the number strata and we have used Eq. 6.12. The unknown constants A_{2m-1}, B_{2m-1}, A_{2m}, B_{2m}, H_2^+ and E_2^+ can be determined from Eqs. 4.10 and 6.15. In Eq. 4.10, the plasma fields at r = a are determined by Eq. 6.8, and Eq. 6.10 with j = m and Eqs. E.1b and d. The incoming wave amplitudes (A_{2m}, B_{2m}) at r=a are given by the solution of the following two simultaneous equations when Eqs. 6.15c and a are used to eliminate the outgoing waves.

$$\alpha_{11}\, A_{2m-1} + \alpha_{12}\, A_{2m} + \alpha_{13}\, B_{2m-1} + \alpha_{14}\, B_{2m} = F_1 \qquad 6.16a$$

$$\alpha_{21}\, A_{2m-1} + \alpha_{22}\, A_{2m} + \alpha_{23}\, B_{2m-1} + \alpha_{24}\, B_{2m} = F_2 \qquad 6.16b$$

where the forcing or driving functions are given by

$$F_1 = \frac{i(h_1 + h_2 + h_3)}{y_o\, \nu a\, \Delta_{ac'}} \cdot \sigma_\nu \qquad 6.17a$$

$$F_2 = \frac{-i(e_1 + e_2 + e_3)}{z_o\, \nu a\, \Delta_{ac}} \cdot \sigma_\nu \qquad 6.17b$$

and the α_{ik} coefficients are defined in Eq. E.9a and b.

Having determined the fields at the plasma edge, the fields at an arbitrary position in the plasma may be calculated. Referring to Fig. 6.3b, scattering matrices S^i and S^o are defined that relate the wave amplitudes at the plasma edge and the innermost strata to those at an arbitrary position, "r". Four of the eight relations may be used to determine the wave amplitudes at "r". For a position inside the innermost strata, Eq. 6.15 may be used to determine the incoming wave amplitudes.

6.d) Power flow, plasma heating, and antenna loading: The calculation of the self-consistent plasma electric and magnetic fields was outlined in Secs. 6b and c. In addition to these fields, quadratic forms or products of field quantities are of interest. In particular, the time averaged power flow per cross-sectional area is obtained from Poynting's theorem.

$$P(w/m^2) = \frac{1}{2} \text{Re} \left[\vec{E}(\vec{r}) \times \vec{H}^*(\vec{r})\right] \cdot \hat{a}_r$$

Averaging over a cylinder of radius, r_o, and using Parseval's theorem, the inward power flow through a cyclinder of radius r_o is equal to,

$$P(r=r_o) = \frac{-r_o}{2} \sum_n \int_{-\infty}^{\infty} \text{Re}[E_\phi H_z^* - E_z H_\phi^*] \, dk_z \qquad 6.18$$

In the local approximation, the plasma currents in phase with the electric field determine the power absorbed by the plasma. The plasma currents are determined by the conductivity tensor multiplied by the self-consistent plasma fields. The conductivity tensor is implicitly defined in terms of the equivalent dielectric tensor by Eq. 5.7a. The local, time-averaged power transferred to the plasma is given by

$$p(w/m^3) = \frac{1}{2} R_e(\vec{E} \cdot \vec{J}_\alpha^*)$$

where the subscript on $\vec{J}$ indicates the contribution to the current density by species α. Integrating over the length of a field line and averaging over the circumference of a cylinder of radius r_o, the power absorbed by the plasma is given by

$$p(r_o, w/m^2) = \frac{1}{4\pi} \sum_n \int_{-\infty}^{\infty} Re\ (\vec{E} \cdot \vec{J}_\alpha^*)\ dk_z \qquad 6.19$$

From an electrical engineering viewpoint, the complex impedance of the antenna is of interest. The power transferred out of the antenna region is given by,

$$P_c = -\frac{1}{2} \int \vec{E} \cdot \vec{J}^*\ d\vec{v}$$

Performing the ϕ and z integrations, we have;

$$P_c(w) = -\frac{1}{2} \sum_n \int_{-\infty}^{\infty} dk_z \int_b^c dr\ (\vec{E} \cdot \vec{J}^*) \qquad 6.20a$$

where the r integration is performed over the radial extent of the antenna. The source impedance follows directly from Eq. 6.20.

$$Z = \frac{2P_c(w)}{|I|^2} \qquad 6.21a$$

In addition, mutual impedance between coils may be calculated. For example, the mutual impedance between coil 1 and 2 is of the form

$$Z_{12} = \frac{-\sum_{n} \int_{-\infty}^{\infty} dk_z \int_{b}^{c} dr \, (\vec{E}_2 \cdot \vec{J}_1^*)}{I_2 \, I_1} \qquad 6.21b$$

where the product $\vec{E}_2 \cdot \vec{J}_1^*$ is field due to coil 2 evaluated at coil 1. For magnetization current sources, $\vec{E} \cdot \vec{J}^*$ is replaced by $\vec{H}^* \cdot \vec{M}$.

7. Sample Results from "ANTENA"

In this section, we present a sampling of results from the computer code "ANTENA". For the antennas of Fig. 1.1, the code numerically performs the inverse ($n - k_z$) transformation defined by Eq. 2.2 of the transformed fields calculated in Sec. 4-6. As examples, we first investigate the loading impedance of various ICRF antenna configurations; and then investigate, in detail, the coupling characteristics of the Nagoya-type III coil. As a final topic, the convergence of the field solution is examined as a function of the number of strata in a radial profile. The plasma and antenna parameters that are assumed in this section are contained in Table 7.1

7.a) Loading impedance: Shown in Fig. 7.1 is the loading impedance of six different antennas as a function of frequency for ($.2 \leq \omega/\omega_{ci} \leq 1.2$). The solid line is the antenna reactance which corresponds to the left-hand scale. The value of loading resistance is defined by the scale on the right. The most notable feature of the dashed curves is the peak in the loading resistance due to the generation of the ion cyclotron wave. The location of the peak (relative to ω_{ci}) is dependent upon the particular antenna. The antennas in the left panel are longer coils which have a current pattern that is distributed along the z-axis. These coils generate a broader k_z- spectrum, and optimal ion cyclotron wave generation occurs at lower frequencies. The full turn loop exclusively excites $n = 0$ modes, the half turn loop excites both $n = 0$ and ± 1, and the dual half turn only $n = \pm 1$. The location of the loading resistance peak in the right panel of Fig. 7.1 indicates the shift in frequency of the ion cyclotron wave due to azimuthal wave number. The magnitude of the loading resistance is largest for the long coils, Nagoya-type III and rectangular aperture. The rectangular aperture has the advantage of a lower inductance compared to the Nagoya-type III, and the aperture coil defines a very low Q load. There is

Table 7.1 Parameters for Figs. 7.1 - 11

Figs. 7.1 - 6

$a = 15cm.$, $b = 20cm.$, $c = 35cm.$

$B_o = 2KG$, $n_e = 5 \times 10^{12}\ cm^{-3}$, $T_i = T_e = 100eV$, square profile.

$b = 20cm$ for all coils

Nagoya-type III:	$I = 1000a$,	$w = 10cm.$,	$L = 40cm.$
Half Nagoya:	$I = 1000a$,	$w = 10cm.$,	$L = 40cm.$
Rectangular aperture:	$B = 30G$,	$w = 14cm.$,	$L = 40cm.$,
	$b = c = 20cm.$		

Full turn loop:	$I = 1000a$,	$w = 10cm.$	
Half loop:	$I = 1000a$,	$w = 10cm.$,	$\theta = 180°$
Dual half turns:		$w = 10cm$	$\theta = 180°$
	$I_1 = 1000a$,	$I_2 = -1000a$,	
	$\phi_o(1) = 0°$,	$\phi_o(2) = 180°$,	

Figs. 7.5 - 7.11 use the Nagoya-type III coil

Figs. 7.7 and 7.9

$r = 15cm.$, $\phi = 0$, $z = 5cm.$

$\omega/\omega_{ci} = .5$ for 7.7

$\omega/\omega_{ci} = 1.3$ for 7.9

All other parameters the same as above.

Figs. 7.8 and 7.10

$\omega/\omega_{ci} = .7$ for 7.8

$\omega/\omega_{ci} = 1.6$ for 7.10

Parabolic profile $w_n = 15.2cm.$ $w_T = 30cm.$

All other parameters as same as Fig. 7.7

Fig. 7.11 same parameters as Fig. 7.8

FIG. 7.1

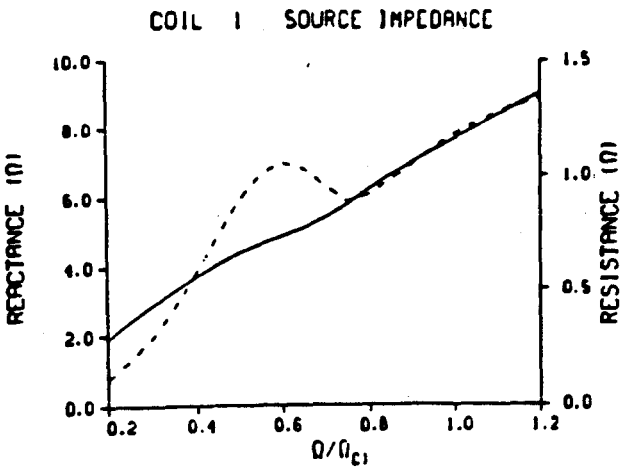

NAGOYA TYPE III

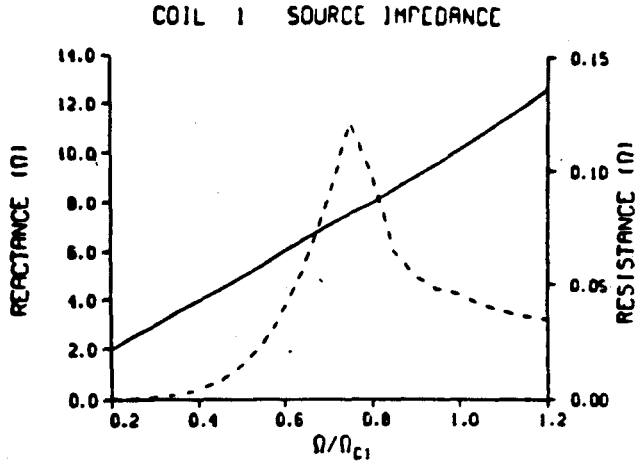

FULL TURN LOOP

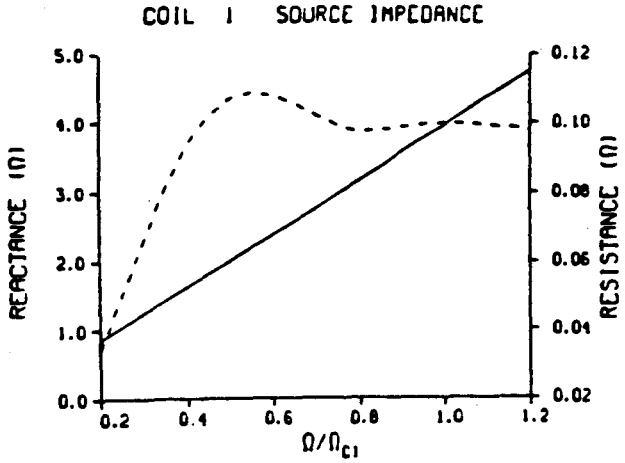

HALF NAGOYA

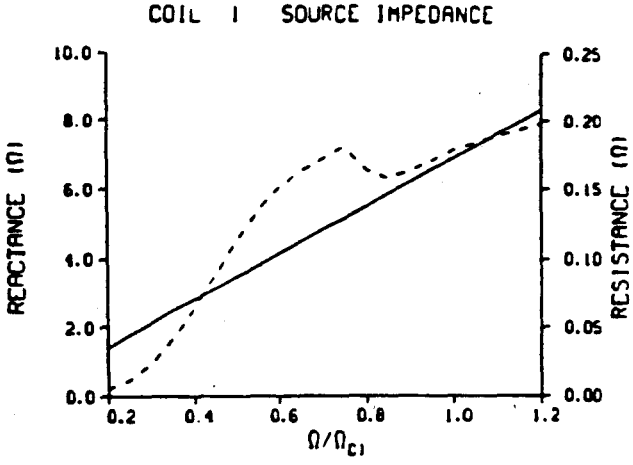

HALF TURN LOOP

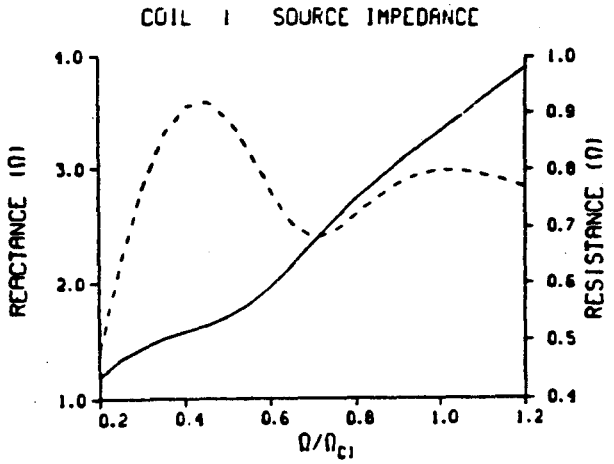

RECTANGULAR APERTURE

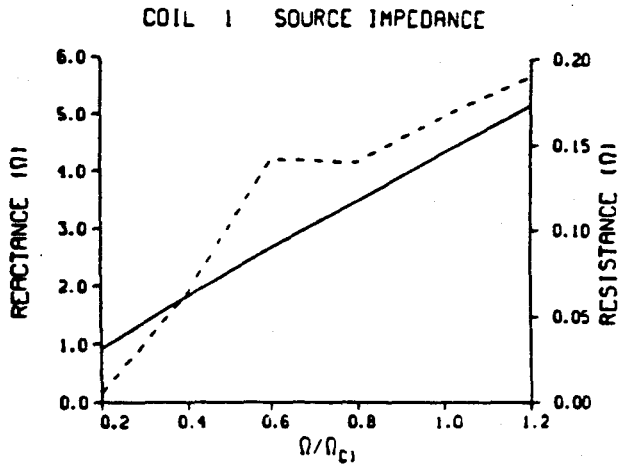

DUAL HALF TURNS

a dramatic drop in the loading resistance when comparing the half-Nagoya and the Nagoya-type III. This is presumably due to a reduction in the magnetic flux coupled to the plasma when using the former coil. For all the antennas, the reactance tends to be a linear function of frequency suggesting that the inductance remains constant. The notable deviations from lienarity occur near loading resistance peaks of the aperture and type III coils.

Shown in Fig. 7.2 is the loading impedance (of the same set of antennas as Fig. 7.1) as a function of frequency for ($.8 \leq \omega/\omega_{ci} \leq 6$). Again, the most striking features are the distinct peaks of the loading resistance due to generation of the fast magnetosonic waves. The frequency at which the loading peaks occur is dependent upon the ($n - k_z$) spectrum of the antenna. The full and half-turn loops excite $n = 0$ modes which have a large loading resistance. The height of the loading peaks is indicative of the fact that the $n = 0$ fast mode has a small value of k_z and weakly damped in the context of the present model. In a real experiment, nonlinear processes or plasma turbulence would broaden the loading spikes of the $n = 0$ modes. Comparing the loading resistance curves for the half turn loop and the dual half-turn indicates $n = 0$ modes dominate the $n = \pm 1$ modes for the half turn. The succession of loading peaks as ω/ω_{ci} increases are due to higher order radial modes. Finally, the half Nagoya coil efficiently excites $n \neq 0$ fast waves, a result that is not obvious from the orientation of this coil. The loading peaks of the Nagoya-type III coil will be examined in more detail in the following section.

The relationship of the loading impedance as a function of the plasma density is illustrated in Fig. 7.3. This variation is of particular importance when ICRF heating is used to build up the plasma density. The loading impedance of the rectangular aperture is compared to that of dual half turn loops. The most dramatic constrast is the larger loading resistance of the aperture antenna, and the fact that the inductance of this

FIG. 7.2

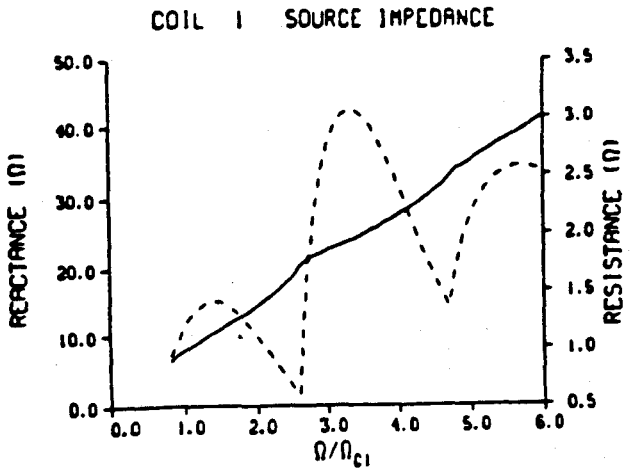

NAGOYA TYPE III

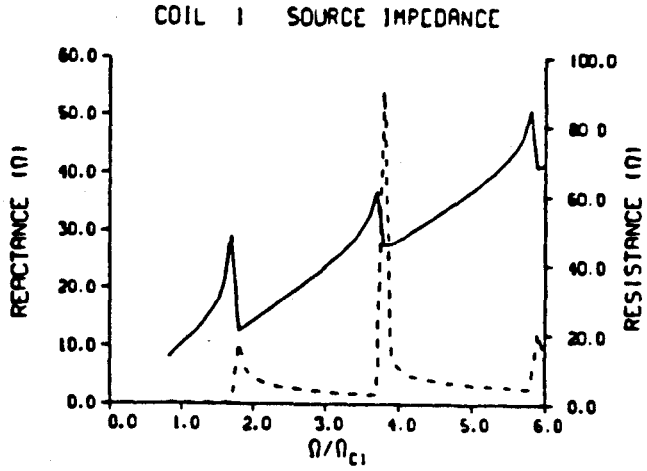

FULL TURN LOOP

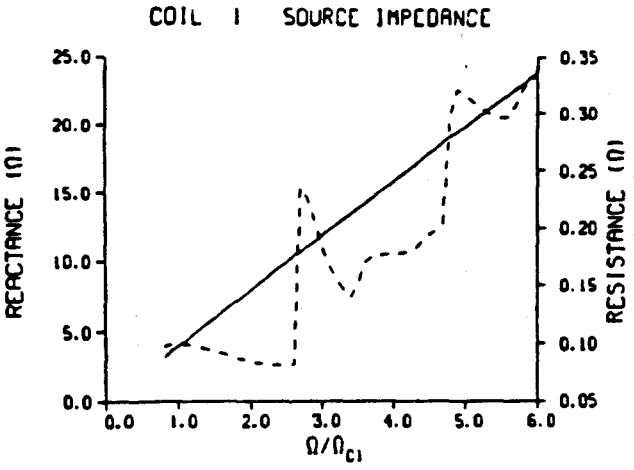

HALF NAGOYA

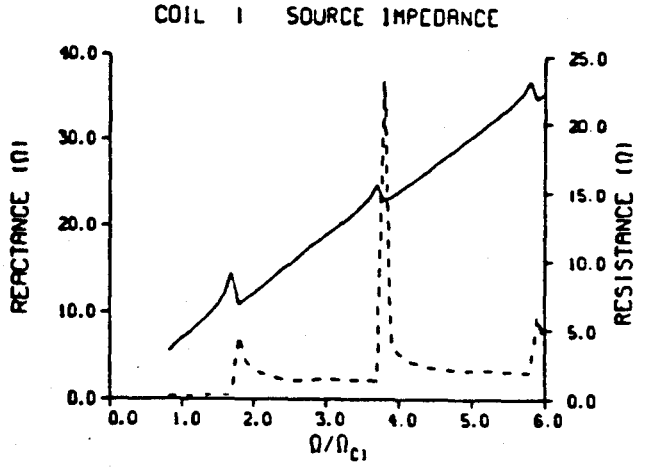

HALF TURN LOOP

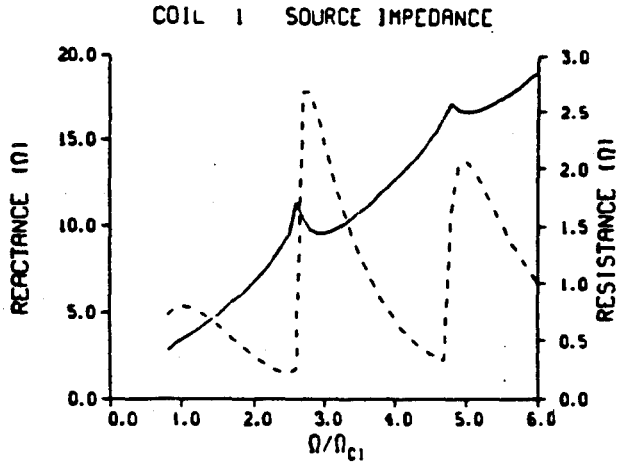

RECTANGULAR APERTURE

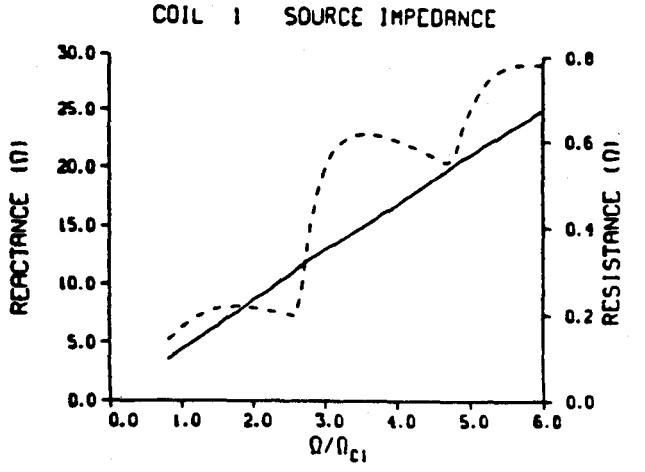

DUAL HALF TURNS

FIG. 7.3

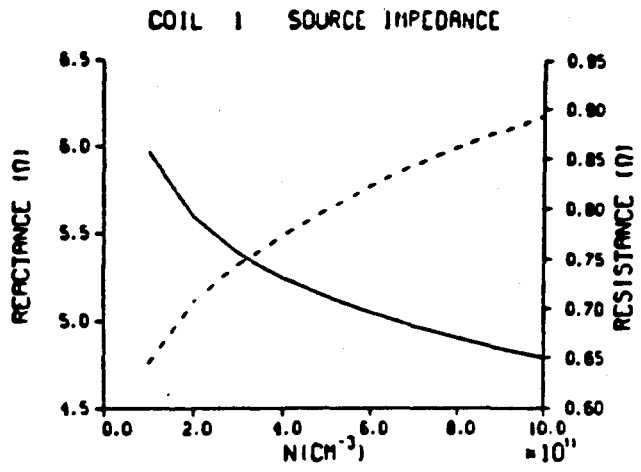
COIL 1 SOURCE IMPEDANCE
REACTANCE (Ω)
RESISTANCE (Ω)
N(CM⁻³)
×10¹¹
RECTANGULAR APERTURE
W/WC(1) = 1.00E+00

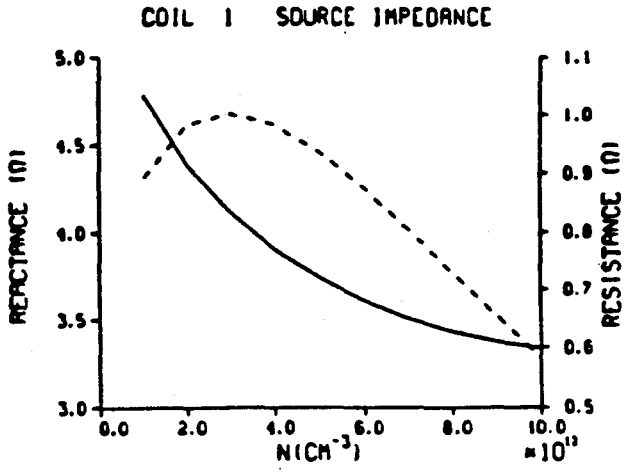
COIL 1 SOURCE IMPEDANCE
REACTANCE (Ω)
RESISTANCE (Ω)
N(CM⁻³)
×10¹³
RECTANGULAR APERTURE
W/WC(1) = 1.00E+00

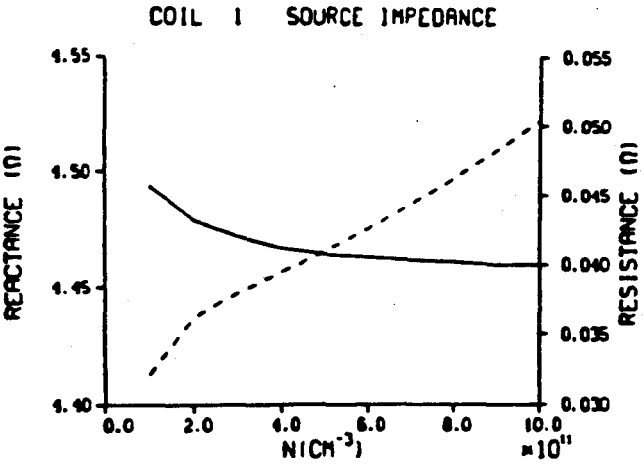
COIL 1 SOURCE IMPEDANCE
REACTANCE (Ω)
RESISTANCE (Ω)
N(CM⁻³)
×10¹¹
DUAL HALF TURNS
W/WC(1) = 1.00E+00

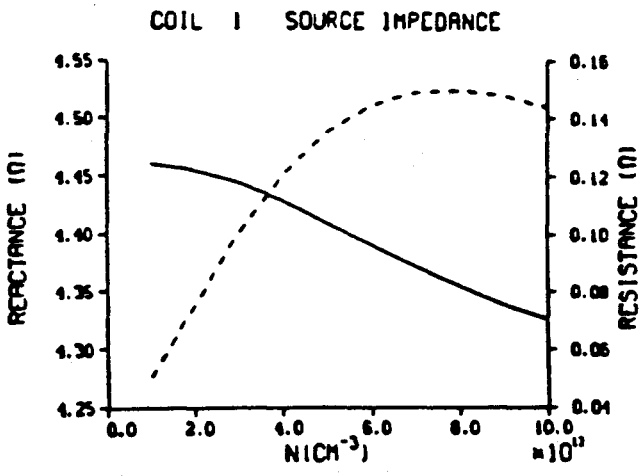
COIL 1 SOURCE IMPEDANCE
REACTANCE (Ω)
RESISTANCE (Ω)
N(CM⁻³)
×10¹³
DUAL HALF TURNS
W/WC(1) = 1.00E+00

coil changes with plasma density. The rectangular aperture forms a low Q circuit whereas the half-turn loop antenna would be much higher Q. The loading resistance peak observed in Fig. 7.3 is due to excitation of a n = 1 fast wave.

The mutual impedance between a pair of antennas is examined in Fig. 7.4. The upper left-hand graph shows the mutual inductive reactance between a pair of isolated current loops as a function of the separation distance between the coils. The results are in agreement with classical field calculations.[27] The next three graphs are the mutual impedance between half turn loops inside a conducting cylinder of 35 cm radius. The diagonally opposite graphs show the effect of plasma on the coupling between coils at $\omega = \omega_{ci}$. At this frequency, the only effect of the plasma is to add a small mutual resistance between coils that decreases with separation distance. The last graph plots the mutual impedance as a function of frequency for two half turn loops separated by a distance of 20 cm. The loading peaks are due to coupling between the antennas due to excitation by n = 0 fast waves.

7.b) The Nagoya-type III coil: The loading impedance as a function of frequency for a Nagoya-type III coil is shown in the upper left graph of Figs. 7.1 and 7.2. In this section, we investigate in more detail the coupling characteristics of this coil. Shown in Figs. 7.5 and 7.6 are the polarization and the azimuthal dependence (n = azimuthal mode number) of the various loading resistance peaks as a function of frequency. In these figures, the graphs labeled right or left-hand rotation were generated by superimposing two type III coils with one oriented at an angle of $\phi = 90^{o}$ from the other. Further, by delaying or advancing the current by 90^{o}, the applied field may be rotated in the sense of the ion gyro motion (left-hand rotation) or in the sense of electron gyration (right-hand rotation). The graphs labeled n = __ mode were generated from a single type III coil by retaining only that mode number in the Fourier sum over n. Examination of Fig. 7.5 indicates that the loading resistance peak below ω_{ci} is due to n = -1, left-hand polarized ion cyclotron wave. The n = 1 mode is responsible for the linear with frequency increase in the loading resistance for $\omega < 1.2\ \omega_{ci}$, and the n = ± 3 components of the total field solution are down by a

FIG. 7.4

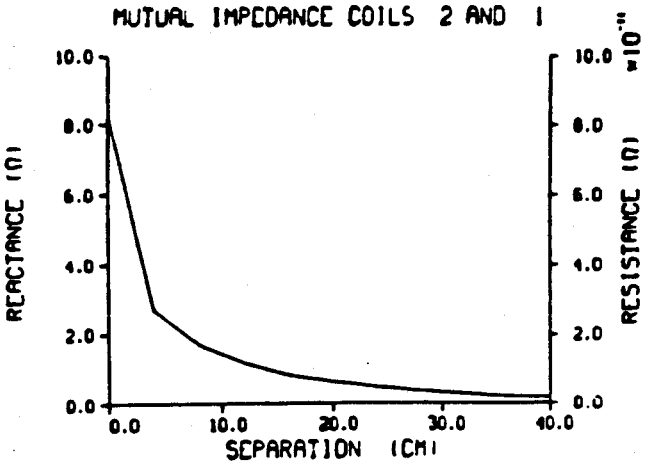

FULL TURN LOOPS C-1.E10

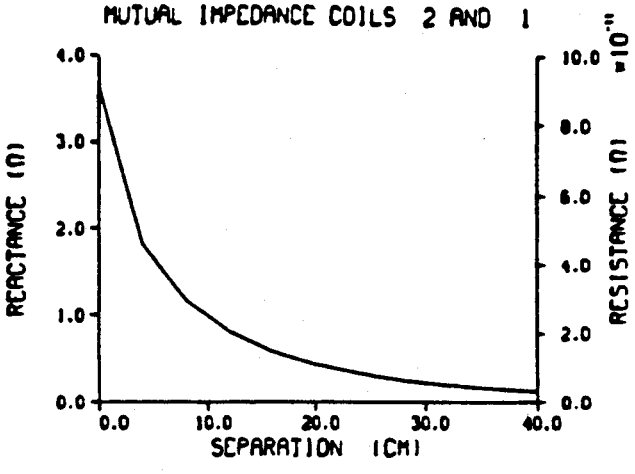

HALF TURN LOOPS C-35 CM.

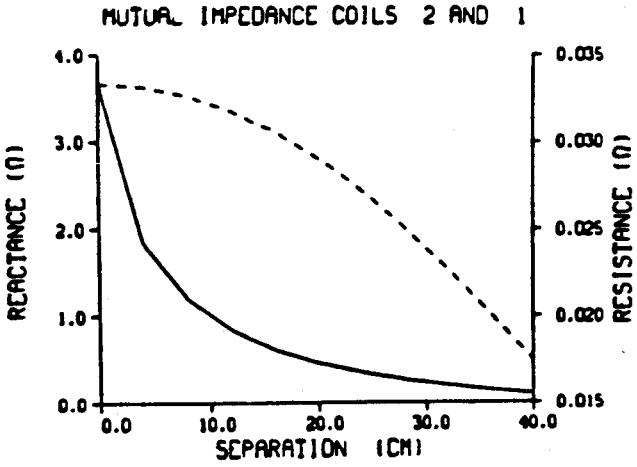

HALF TURN LOOPS C-35 CM.

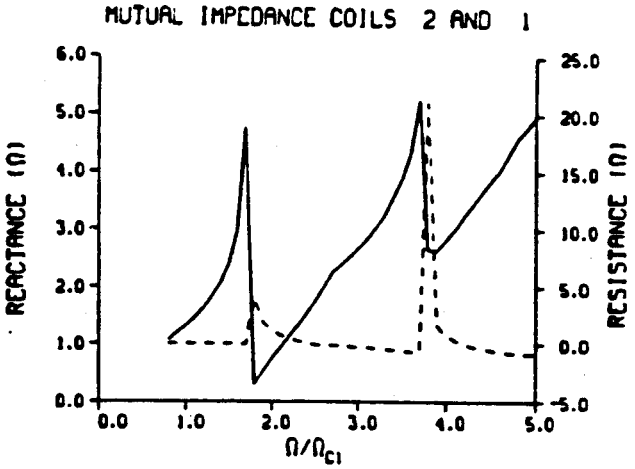

HALF TURN LOOPS ZO-20 CM.

FIG. 7.5

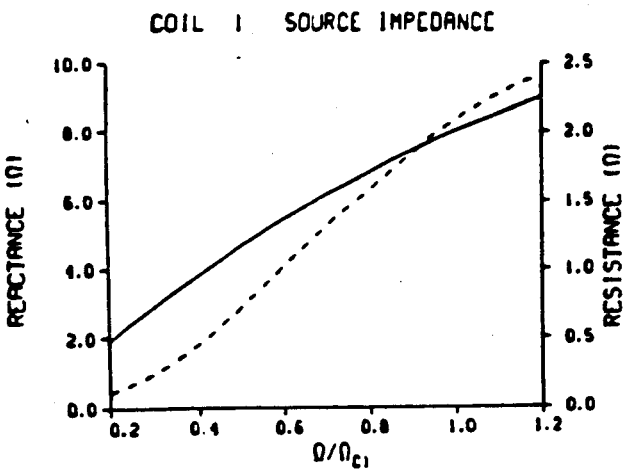

NAGOYA TYPE III RIGHT-HAND ROTATION

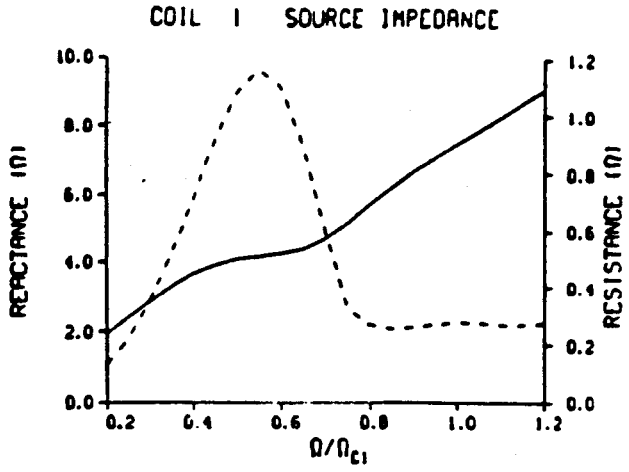

NAGOYA TYPE III LEFT-HAND ROTATION

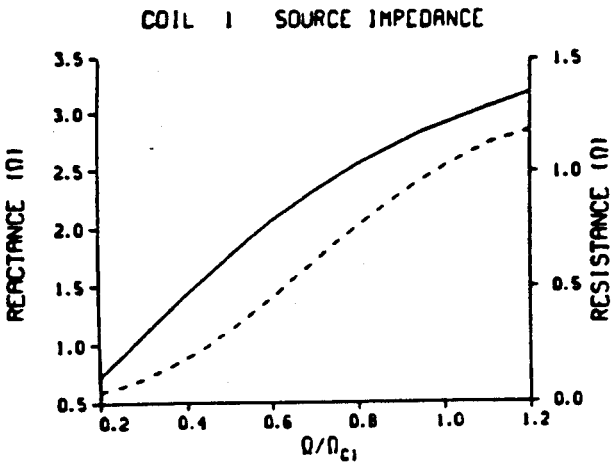

NAGOYA TYPE III N=1 MODE

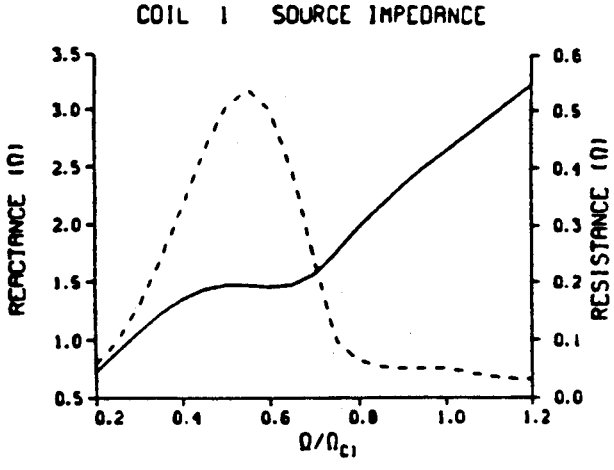

NAGOYA TYPE III N=-1 MODE

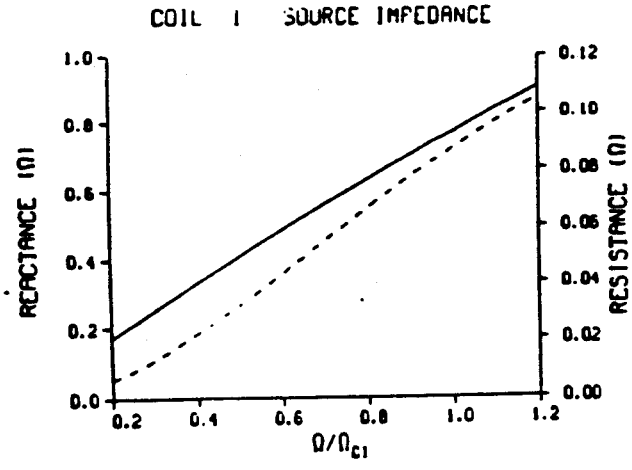

NAGOYA TYPE III N=3 MODE

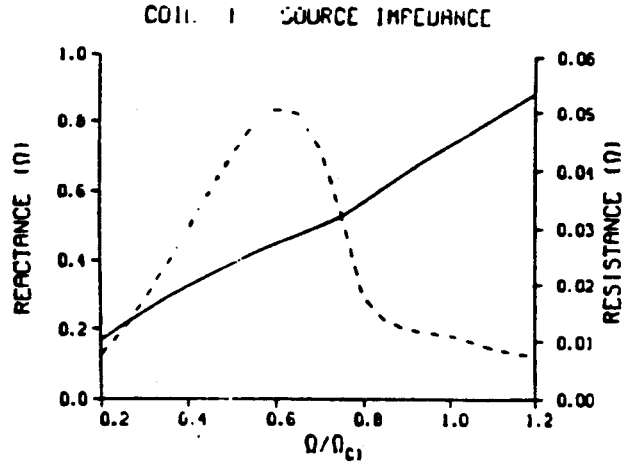

NAGOYA TYPE III N=-3 MODE

FIG. 7.6

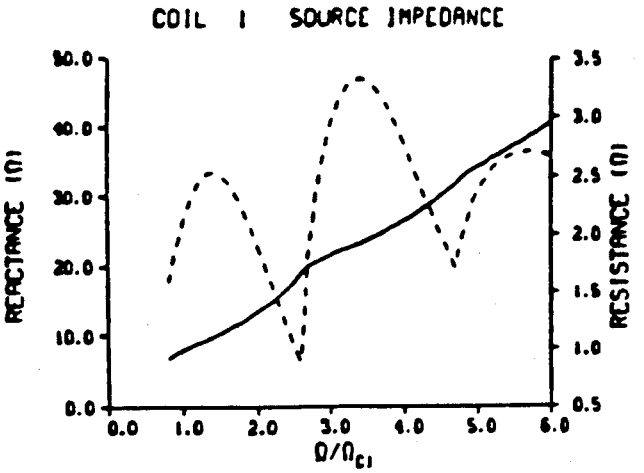

NAGOYA TYPE III RIGHT-HAND ROTATION

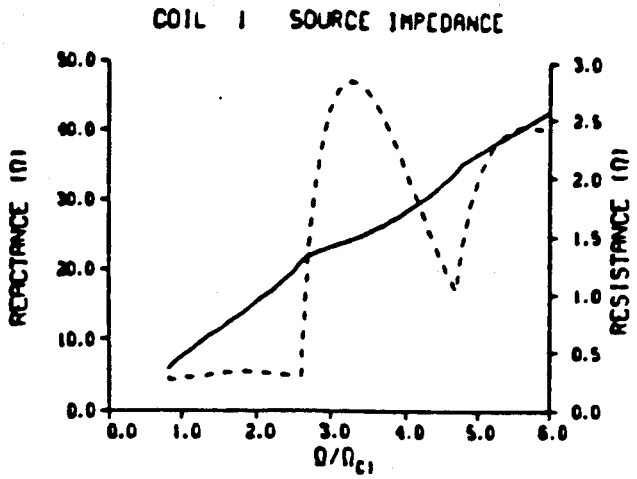

NAGOYA TYPE III LEFT-HAND ROTATION

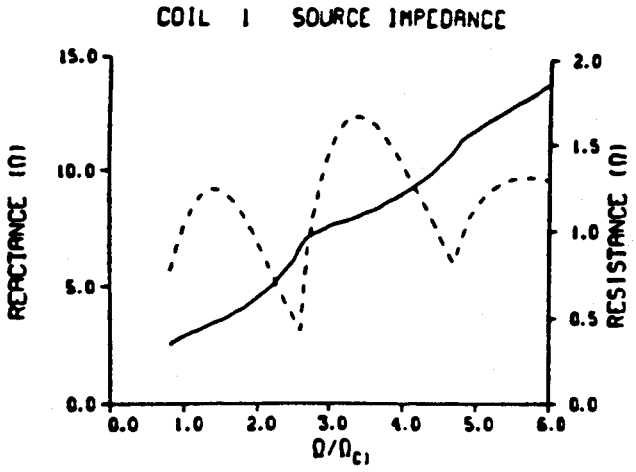

NAGOYA TYPE III N-1 MODE

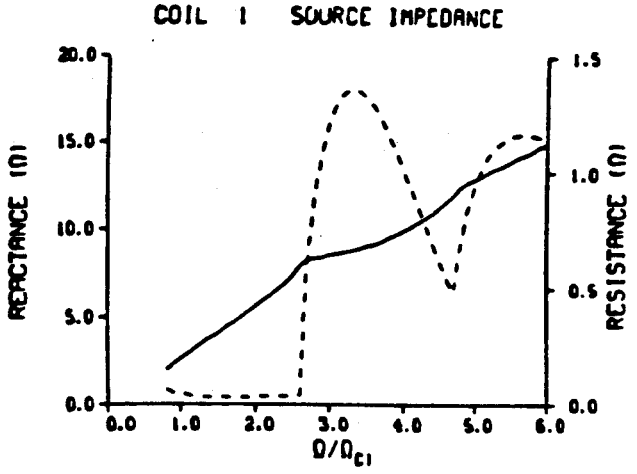

NAGOYA TYPE III N--1 MODE

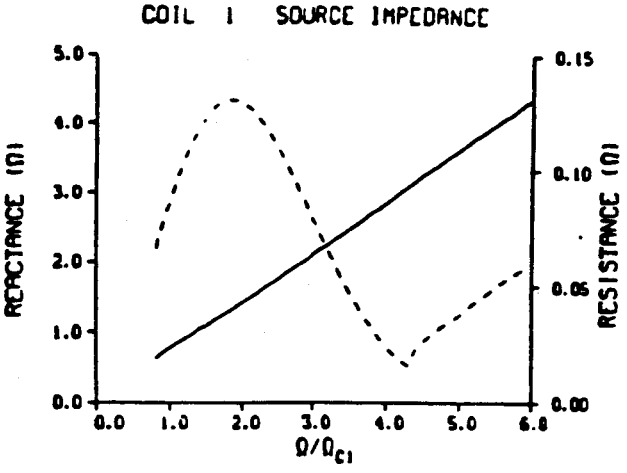

NAGOYA TYPE III N-3 MODE

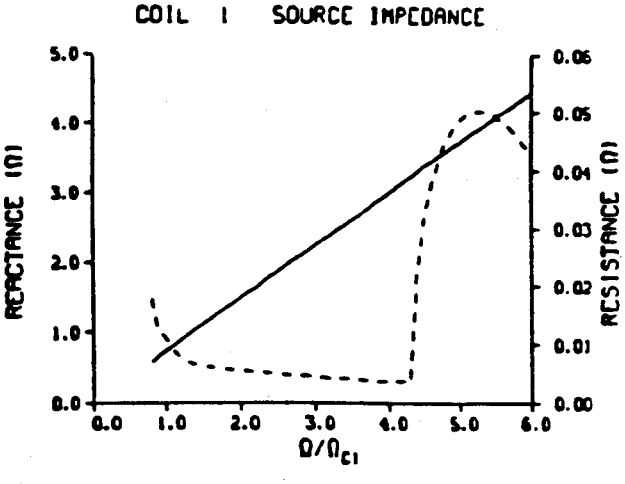

NAGOYA TYPE III N--3 MODE

factor of 10. Referring to Fig. 7.6, three loading resistance peaks are observed in the frequency range of .8 to 6 ω_{ci}. The loading resistance peak near $\omega = 1.2\ \omega_{ci}$ is a n = 1 right-hand polarized fast wave mode. This is the fast wave mode with the lowest cut-off frequency. The n = 3 fast wave has a much lower amplitude with a peak at a slightly higher frequency as observed in the lower left graph of Fig. 7.6. The loading peak at $\omega = 3.3\ \omega_{ci}$ is a combination of $n = \pm 1$ modes with mixed polarizations. The $n = \pm 3$ modes are absent at this frequency. Finally, the last peak $\omega = 5.5\ \omega_{ci}$ is due to $n = \pm 1$ and -3 modes with the amplitude of the last mode down by a factor of 10. The wave exhibits mixed polarization at this frequency.

We further examine the ion cyclotron wave near $\omega = .5\ \omega_{ci}$(Figs. 7.7, 7.8), and the n = 1 fast wave at $\omega \backsim 1.3\ \omega_{ci}$ (Figs. 7.9, 7.10). Shown in Fig. 7.7 are the k_z spectrums of B_x field of the antenna in vacuum (upper left) with plasma (upper right) and the two wave numbers defined by Eq. 6.9. The fast mode refers to the smaller root of Eq. 6.9 and the slow mode to the larger root. The solid line corresponds to the left-hand scale and the dashed line corresponds to the right-hand scale. The k_z - spectrum is calculated for the n = -1 mode. The k_z - spectrum in a vacuum is a smooth function of k_z, peaking at a value of $\backsim .05\ cm^{-1}$. When plasma is introduced, excitation of the ion cyclotron wave significantly narrows the k_z- spectrum with the peak centered at the peak of the k_z - spectrum in vacuum. The perpendicular wave numbers near this peak indicate that the wave propagates in the window defined by 5.14b, with the wave numbers of comparable value. In particular, the slow mode is weakly damped and can propagate to the core of the plasma. Shown in Fig. 7.8 are the polarization characteristics of the fast and slow modes as a function of plasma radius. The sawtooth behavior is due to the assumption of only ten strata in the density profile. As discussed in Sec. 6, the fast mode is nearly TE and the slow mode is TM_z. The magnitude of the transverse fields of each mode are comparable. Shown in Fig. 7.9 and 10, are the k_z - spectrum and polarization characteristics of the fast and slow modes that comprise the

FIG. 7.7

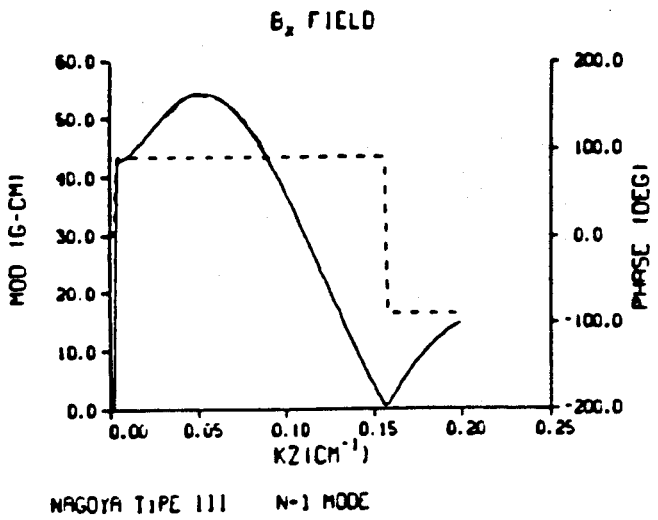
B_x FIELD
MOD IG-CMI
PHASE IDEGI
KZ(CM^{-1})
NAGOYA TYPE III N-1 MODE

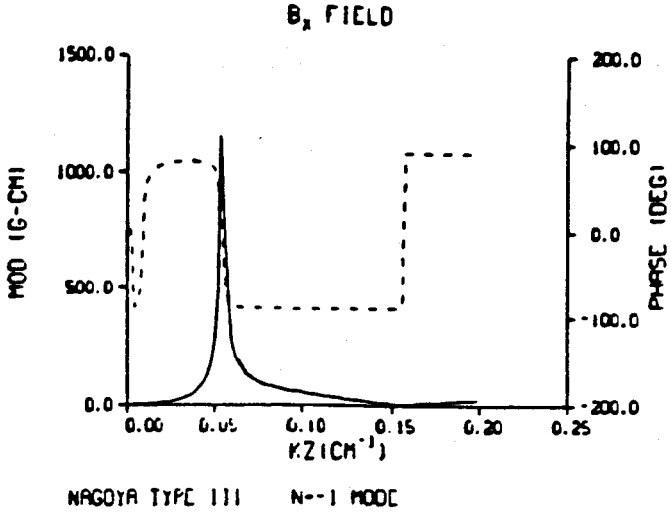
B_x FIELD
MOD IG-CMI
PHASE IDEGI
KZ(CM^{-1})
NAGOYA TYPE III N--1 MODE

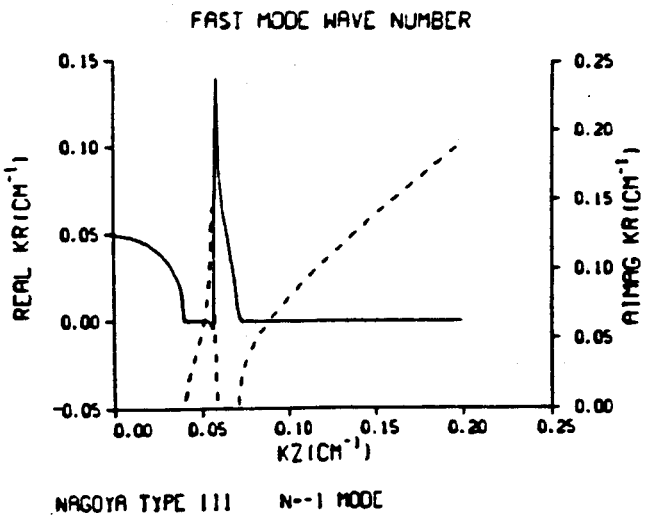
FAST MODE WAVE NUMBER
REAL KR(CM^{-1})
AIMAG KR(CM^{-1})
KZ(CM^{-1})
NAGOYA TYPE III N--1 MODE

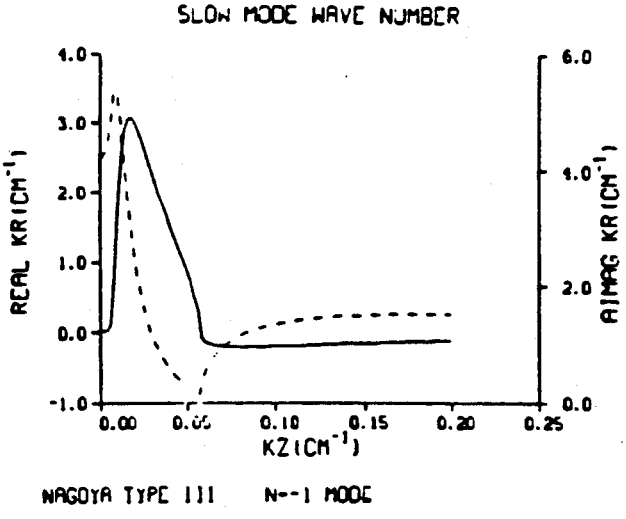
SLOW MODE WAVE NUMBER
REAL KR(CM^{-1})
AIMAG KR(CM^{-1})
KZ(CM^{-1})
NAGOYA TYPE III N--1 MODE

FIG. 7.8

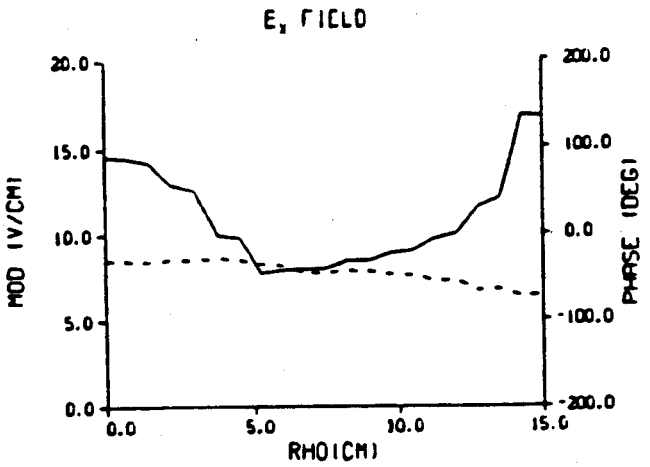

NAGOYA TYPE III FAST MODE

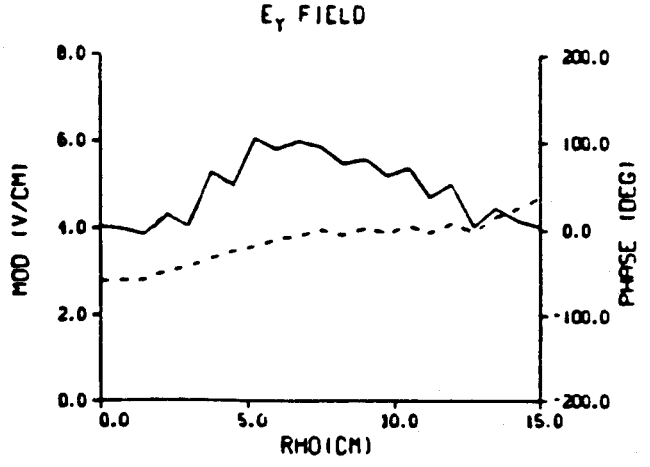

NAGOYA TYPE III FAST MODE

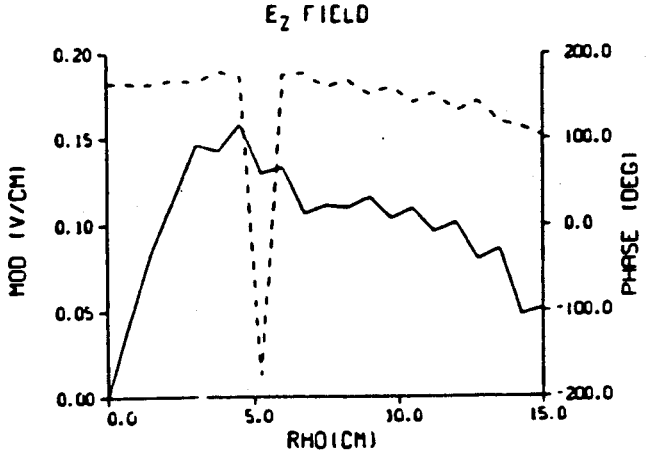

NAGOYA TYPE III FAST MODE

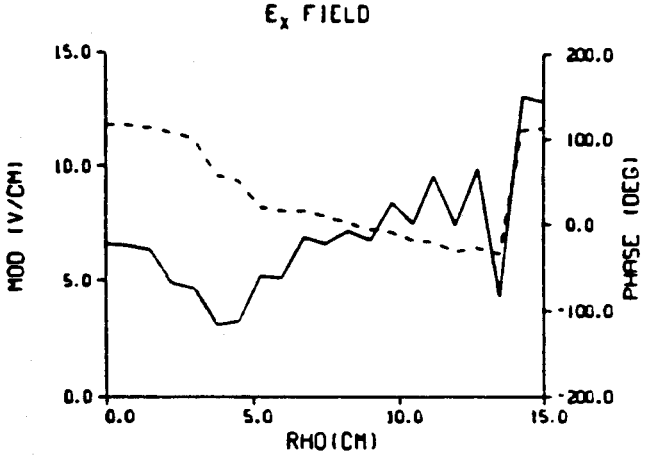

NAGOYA TYPE III SLOW MODE

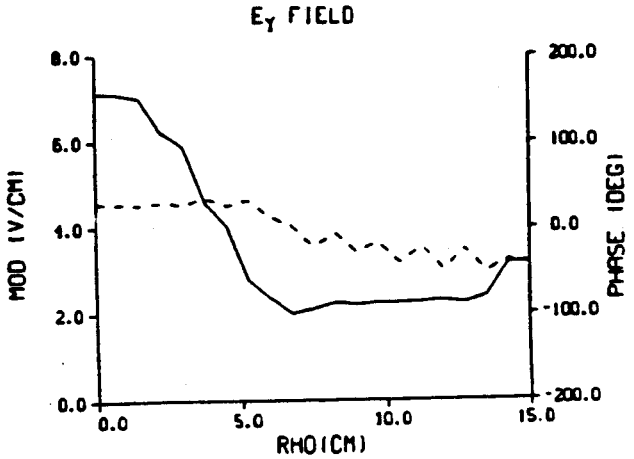

NAGOYA TYPE III SLOW MODE

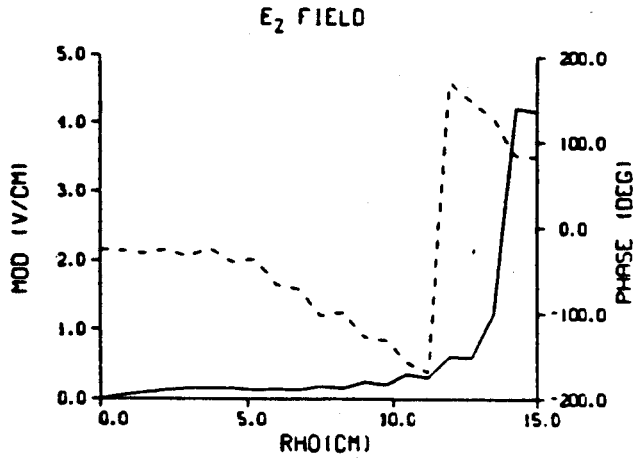

NAGOYA TYPE III SLOW MODE

FIG. 7.9

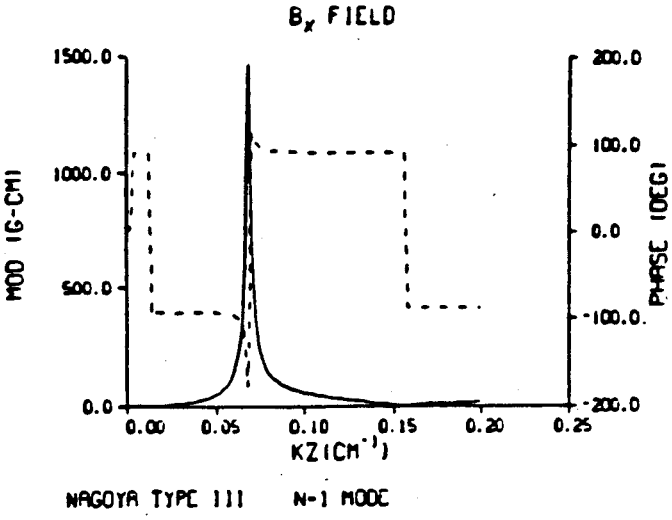
B_x FIELD
MOD IG-CMI
PHASE (DEG)
KZ(CM^{-1})
NAGOYA TYPE III N-1 MODE

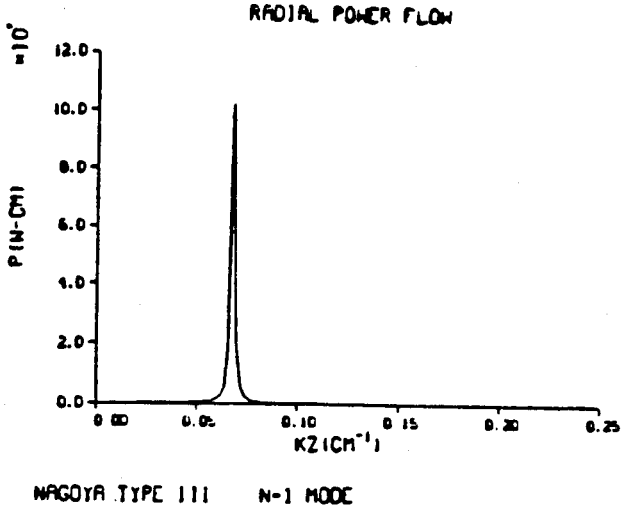
RADIAL POWER FLOW
P(N-CM)
KZ(CM^{-1})
NAGOYA TYPE III N-1 MODE

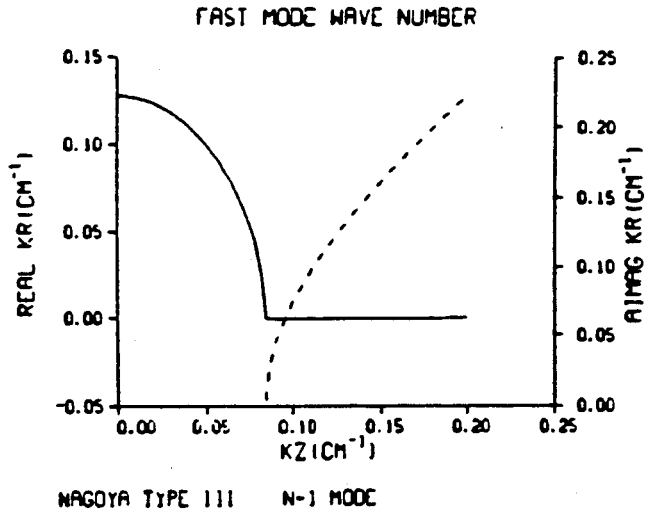
FAST MODE WAVE NUMBER
REAL KR(CM^{-1})
AIMAG KR(CM^{-1})
KZ(CM^{-1})
NAGOYA TYPE III N-1 MODE

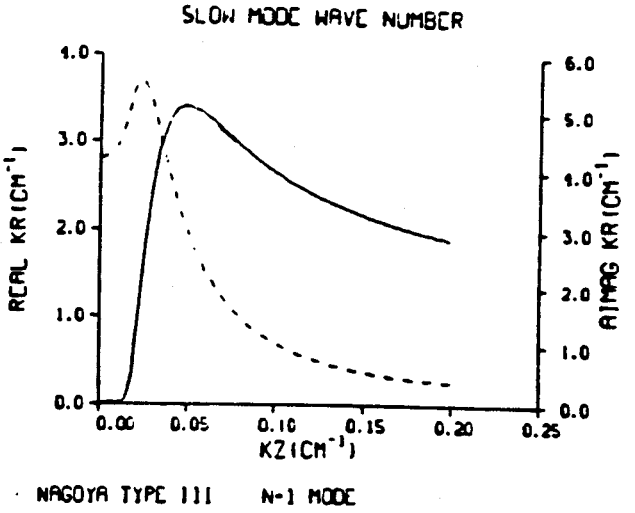
SLOW MODE WAVE NUMBER
REAL KR(CM^{-1})
AIMAG KR(CM^{-1})
KZ(CM^{-1})
NAGOYA TYPE III N-1 MODE

FIG. 7.10

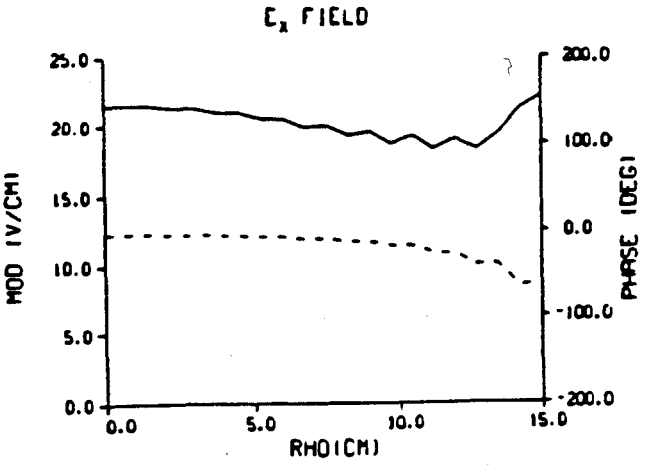

NAGOYA TYPE III FAST MODE

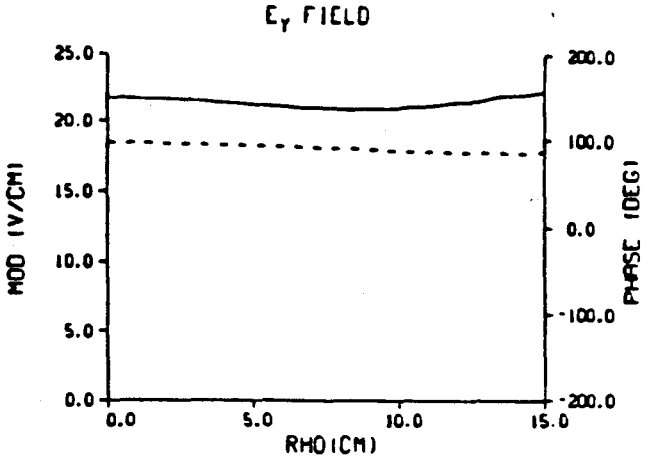

NAGOYA TYPE III FAST MODE

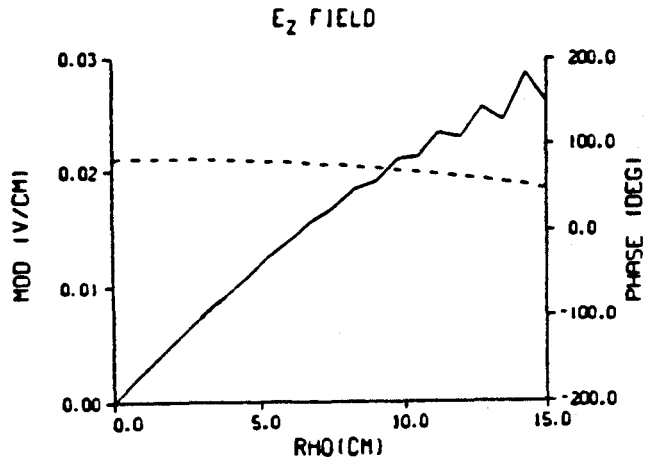

NAGOYA TYPE III FAST MODE

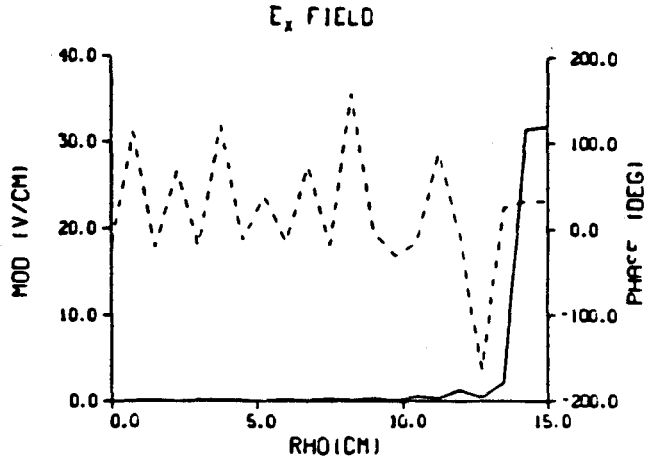

NAGOYA TYPE III SLOW MODE

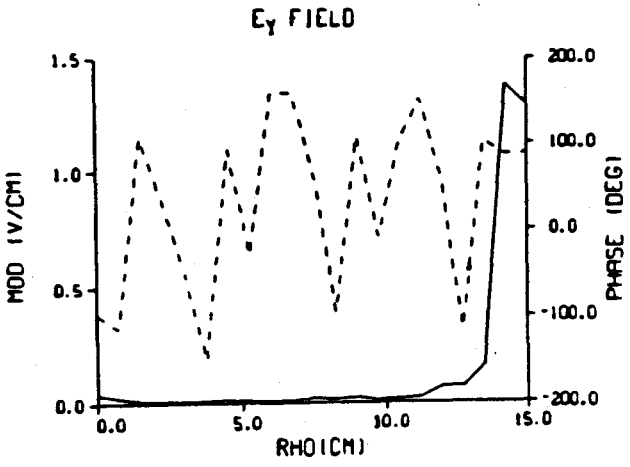

NAGOYA TYPE III SLOW MODE

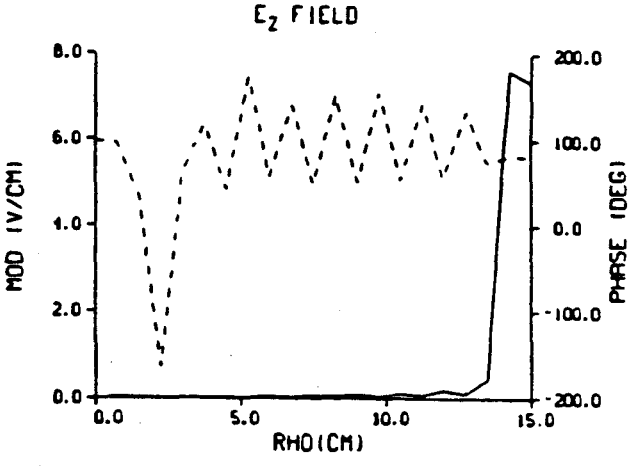

NAGOYA TYPE III SLOW MODE

fields of the n = 1 fast wave at $\omega = 1.3\ \omega_{ci}$. The k_z - spectrum of the B_x field and the radial power flow peak near $k_z \sim .05\ cm^{-1}$ as in the case considered previously. This value of k_z is below the $k_z^2 = k_o^2 R$ cut-off of the fast mode. The wave numbers of the fast and slow modes are signficantly different in this case. The fast mode is only weakly damped; and in contrast, the slow mode is strongly damped. This is observed in Fig. 7.10 where the amplitude of the slow mode rapidly attenuates from the edge of the plasma. In this case, the slow mode tends to heat electrons near the surface of the plasma.

7.c) Convergence of the stratified model: In Sec. 6.1, it was demonstrated that the stratified model approximates a continuous profile as the number of strata "m" approaches a large number such as ∞. In this section, a practical comparison is made using a finite number of strata. Fig. 7.11 contains the radial field profiles for a 10 and 100 strata radial density profile. The 100 strata case, at least to the eye, approaches a continuum. Radial profiles of the y-component of the electric field and the radial power flow are graphed. The agreement between the two is close with the largest discrepancy near the surface of the plasma. In general, the results are sufficiently close so that in the practical application, the 10 strata profile could be used with a considerable savings of computer time. Table 7.2 indicates the numerical convergence of selected field quantities as the number of strata in the profile is increased. It can be observed that the field quantities are converging with less than a one percent change as the strata increases from 80 - 100. The above analysis provides a demonstration of the accuracy of the numerical method used to solve the radial boundary value problem.

FIG.7.11

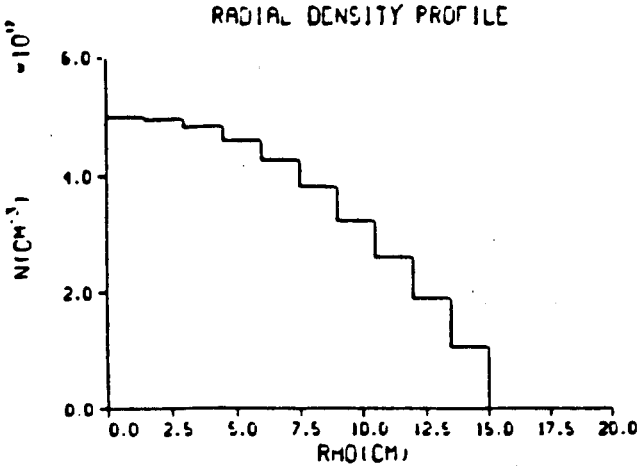
RADIAL DENSITY PROFILE
*10^12
N(CM^-3)
6.0
4.0
2.0
0.0
0.0 2.5 5.0 7.5 10.0 12.5 15.0 17.5 20.0
RHO(CM)

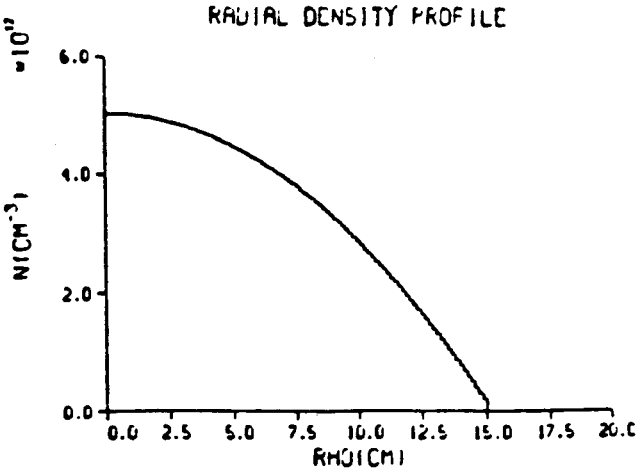
RADIAL DENSITY PROFILE
*10^12
N(CM^-3)
6.0
4.0
2.0
0.0
0.0 2.5 5.0 7.5 10.0 12.5 15.0 17.5 20.0
RHO(CM)

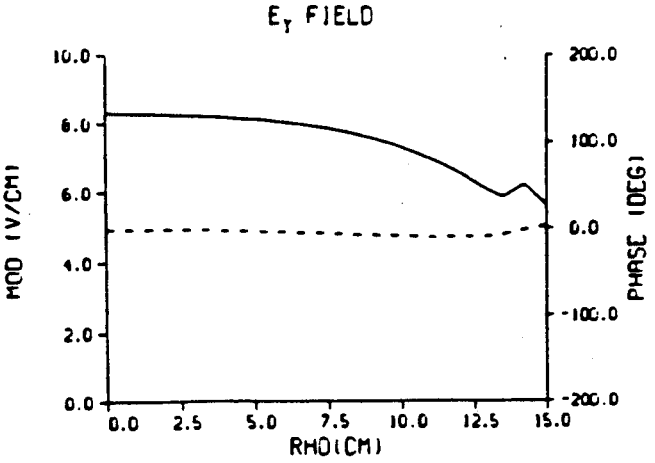
E_Y FIELD
MOD (V/CM)
10.0
8.0
6.0
4.0
2.0
0.0
PHASE (DEG)
200.0
100.0
0.0
-100.0
-200.0
0.0 2.5 5.0 7.5 10.0 12.5 15.0
RHO(CM)

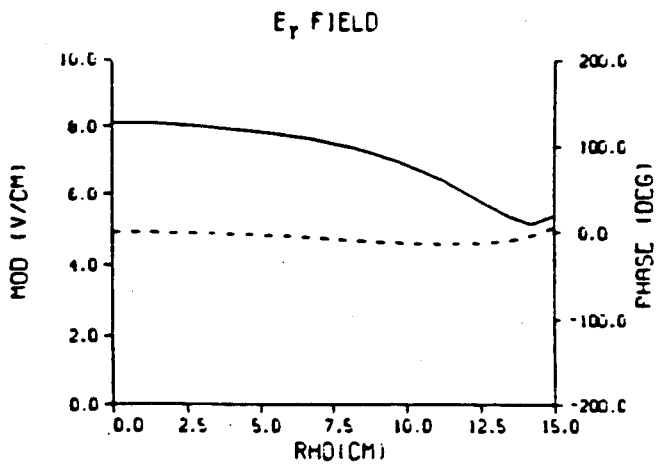
E_Y FIELD
MOD (V/CM)
10.0
8.0
6.0
4.0
2.0
0.0
PHASE (DEG)
200.0
100.0
0.0
-100.0
-200.0
0.0 2.5 5.0 7.5 10.0 12.5 15.0
RHO(CM)

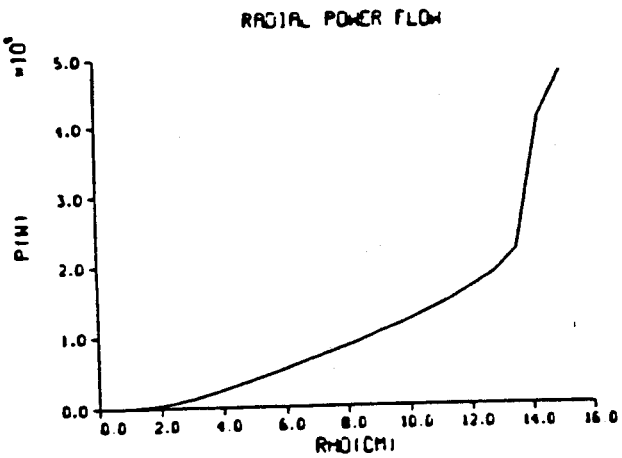
RADIAL POWER FLOW
*10^9
P(W)
5.0
4.0
3.0
2.0
1.0
0.0
0.0 2.0 4.0 6.0 8.0 10.0 12.0 14.0 16.0
RHO(CM)

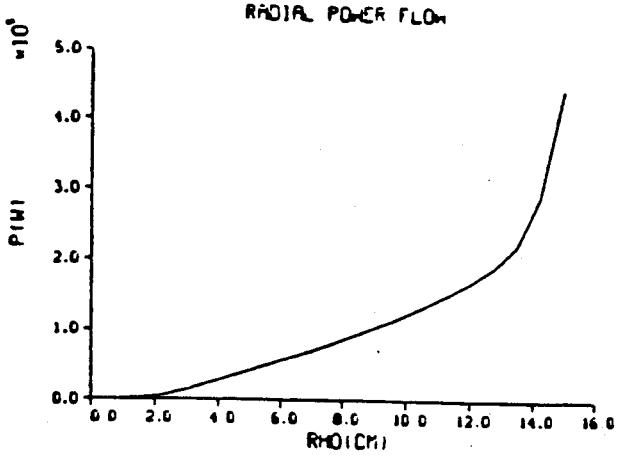
RADIAL POWER FLOW
*10^9
P(W)
5.0
4.0
3.0
2.0
1.0
0.0
0.0 2.0 4.0 6.0 8.0 10.0 12.0 14.0 16.0
RHO(CM)

Table 7.2 Convergence of the fields vs. number of strata

m	$Re\ B_x$	$Im\ B_x$	$Re\ E_y$	$Im\ E_y$	P_r
10	1.386	13.32 G	7.825	-.8540 V/cm	77390 W
20	1.685	13.09	7.664	-1.029	78480
40	1.834	12.95	7.565	-1.112	78930
60	1.883	12.91	7.534	-1.138	79070
80	1.907	12.88	7.517	-1.150	79130
100	1.922	12.87	7.506	-1.158	79170

Appendix A: Glossary of Symbols

This appendix contains a list of the symbols used in this report.

r, ϕ, z	cylindrical coordinates
n	azimuthal mode number
k_z	axial wave number
a	plasma radius
b	inner radius of antenna
c	vacuum chamber
$\vec{E} = (E_r, E_\phi, E_z)$	electric field intensity
$\vec{H} = (H_r, H_\phi, H_z)$	magnetic field intensity
$\vec{J} = (J_r, J_\phi, J_z)$	electric currents
$\vec{M} = (M_\phi, M_z)$	magnetization currents
$k_o = \omega/c$	free space wave number
$\nu^2 = k_z^2 - k_o^2$	vacuum radial wave number
σ_ν	sign of $k_z^2 - k_o^2$
J_n, Y_n	Bessel functions of the first and second kind
I_n, K_n	modified Bessel functions
H_1^n, H_2^n	Hankel functions
e_i, h_i	excitation coefficients (see Sec. 4)
ε	equivalent dielectric tensor
S, D, R, L, P	dielectric elements
k_{r1}, k_{r2}	radial wave numbers with plasma

H_{z1}	fast mode fields
E_{z2}	slow mode fields
A_j, B_j	plasma wave amplitudes
S_{ij}	scattering matrix
I	antenna current
w	antenna width
L	antenna length
θ	azimuthal extent of antenna

Appendix B: Maxwell's Equations for a Vacuum Filled Cylindrical Waveguide

The field solution to Maxwell's equations in a hollow cylindrical tube is conveniently represented by defining modes TE_z (transverse electric) and TM_z (transverse magnetic) to the waveguide axis oriented along the z-axis. The axial field components (H_z and E_z) each separately satisfy Bessel's equation, and the transverse field components are defined in terms of the axial field components. Expressing the (ϕ, z) variation of the field using the ($n - k_z$) inverse transform of Eq. 2.1, a free space radial wave number ν can be defined.

$$\nu^2 = k_z^2 - k_o^2 \qquad \text{B.1}$$

Through Bessel's equation, the wave number (ν) determines the scale length of variation in the radial direction. The axial fields satisfy Bessel's equation.

$$H_z'' + \frac{1}{r} H_z' - (\nu^2 + n^2/r^2) H_z = 0 \qquad \text{B.2a}$$

$$E_z'' + \frac{1}{r} E_z' - (\nu^2 + n^2/r^2) E_z = 0 \qquad \text{B.2b}$$

where the prime indicates differentiation with respect to r. For $\nu^2 > 0$, the general solution to B.2 is expressed in terms of modified Bessel functions.

$$H_z(r) = H_1 I_n(\nu r) + H_2 K_n(\nu r) \qquad \text{B.3a}$$

$$E_z(r) = E_1 I_n(\nu r) + E_2 K_n(\nu r) \qquad \text{B.3b}$$

For $\nu^2 < 0$, Bessel functions of the first and second kind are the appropriate solutions.

$$H_z(r) = H_1 J_n(\nu r) + H_2 Y_n(\nu r) \qquad \text{B.4a}$$

$$E_z(r) = E_1 J_n(\nu r) + E_2 Y_n(\nu r) \qquad \text{B.4b}$$

The transverse fields are expressed in terms of the axial fields.

$$E_r(r) = \frac{-ik_z}{\nu} E_z'(\nu r) + \frac{\omega\mu_o}{\nu} \frac{n}{\nu r} H_z(\nu r) \qquad \text{B.5a}$$

$$E_\phi(r) = \frac{k_z}{\nu} \frac{n}{\nu r} E_z(\nu r) + \frac{i\omega\mu_o}{\nu} H_z'(\nu r) \qquad \text{B.5b}$$

$$H_r(r) = \frac{-\omega\epsilon_o}{\nu} \frac{n}{\nu r} E_z(\nu r) - \frac{ik_z}{\nu} H_z'(\nu r) \qquad \text{B.5c}$$

$$H_\phi(r) = \frac{-i\omega\epsilon_o}{\nu} E_z'(\nu r) + \frac{k_z}{\nu} \frac{n}{\nu r} H_z(\nu r) \qquad \text{B.5d}$$

The prime indicates differentiation with respect to the argument, νr. Note for the Bessel function solutions of Eq. B.4, $\nu^2 < 0$, and the transverse fields reverse direction.

Appendix C: Equivalent Source Currents

The equivalent source currents defined by Eqs. 2.4 and 2.5 or Eq. 3.5, characterizing the various antenna configurations of Fig. 1.1, are calculated in this appendix. The $n - k_z$ transform of the currents defined by Eq. 2.2 are required.

C.1) Notation: In order to represent the spatial extent of the current distribution for the antennas, it is convenient to define the following notation.

$$u_z(-L,L) = u_z(\pm L) = 1, \text{ for } -L < z < L \qquad \text{C.1}$$

$$= 0, \text{ otherwise.}$$

$$\delta_z(L) = \delta(z - L) \qquad \text{C.2}$$

where δ is the Dirac delta function. The $n - k_z$ transform can be applied directly to current distributions contained in a cylindrical surface defined by a constant radius. In essence, a spatially localized current pattern is resolved into a current sheet with the spatial variation expressed as a sum of complex exponentials $[\exp(in\phi + ik_z z)]$.

C.2 Full-turn loop: The full turn loop is diagrammed in Fig. C.1. The current pattern is defined by,

Fig. C.1 Full Turn Loop

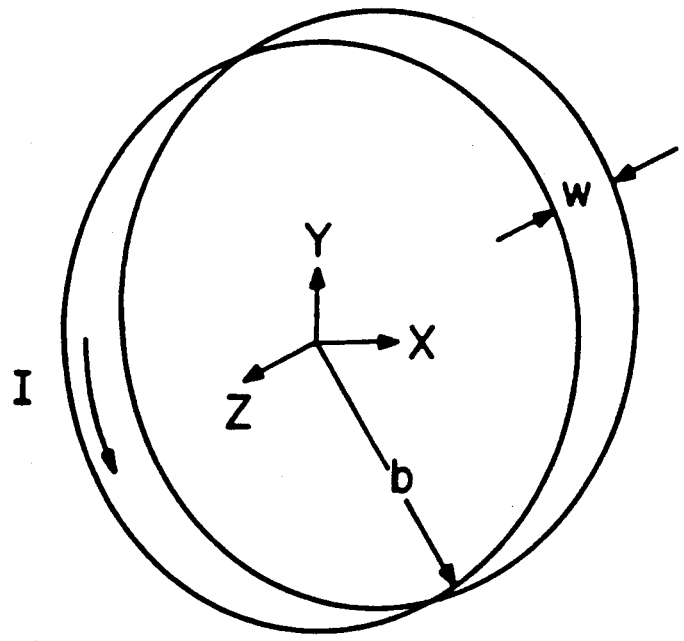

$$J_\phi(r,\ \phi,\ z) = \frac{I}{w}\ \delta_r(b)\ u_z(\pm w/2) \qquad C.3$$

The $n - k_z$ transform of Eq. C.3 becomes,

$$J_\phi(r,\ n=0,\ k_z) = I\ \frac{\sin(k_z w/2)}{k_z w/2}\ \delta_r(b) \qquad C.4$$

C.3 Saddle coil: The saddle coil is diagrammed in Fig. C.2. The azimuthal current density of the filamentary version is defined by the following.

$$J_\phi(r,\ \phi,\ z) = I\ \delta_r(b)\ u_\phi(\pm\theta/2)\ [\delta_z(L/2) - \delta_z(-L/2)] \qquad C.5$$

The $n - k_z$ transform of Eq. C.5 is,

$$J_\phi(r,\ n,\ k_z) = \frac{-2i}{\pi}\ I\ \frac{\sin(n\theta/2)}{n}\ \sin(k_z L/2)\ \delta_r(b) \qquad C.6$$

The filamentary coil of Fig. C.2a can sweep out the current pattern of the finite width coil by translation and rotation.

$$\frac{1}{w}\int_{-w/2}^{w/2} (\text{Eq. C.6})\ e^{-in\theta_o\ -ik_z z_o}\ dz_o$$

and $\theta_o = z_o/b$ coupling the translation and rotation. The $n - k_z$ transform of the finite width coil in Fig. C.2b is,

$$J_\phi(r,\ n,\ k_z) = \frac{-4i}{\pi}\ \frac{I}{w}\ \frac{\sin(n\theta/2)}{n}\ \sin(k_z L/2)$$

Fig. C.2 Saddle Coil

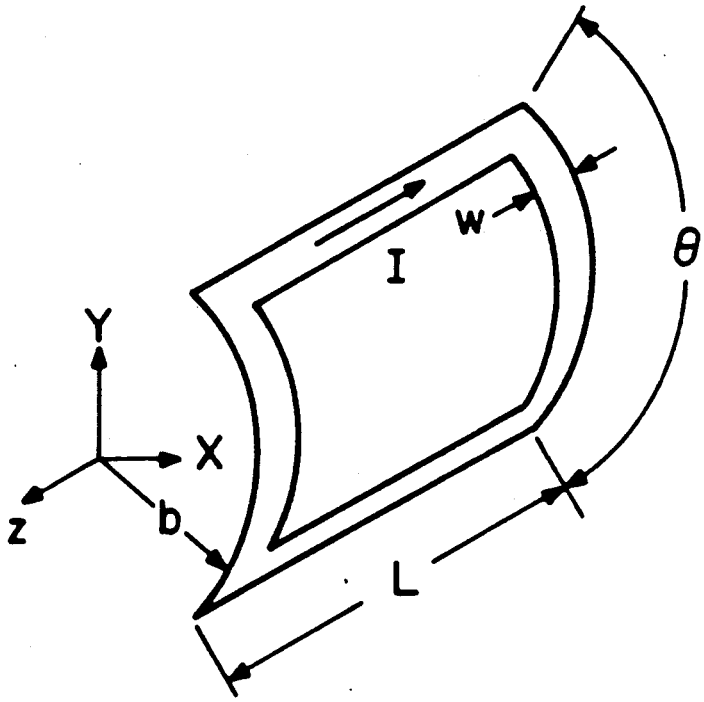

$$\cdot \frac{\sin\left[(k_z + n/b)\, w/2\right]}{k_z + n/b}\, \delta_r(b) \qquad \text{C.7}$$

C.4 Nagoya Type III: The Nagoya Type III coil is diagrammed in Fig. C.3. The azimuthal current density of the filamentary version is defined in the following.

$$J_\phi(r, \phi, z) = I/2\ \delta_r(b)\ [u_\phi(\pm\pi/2) - u_\phi(\pi/2, 3\pi/2)]$$

$$\cdot\ [\delta_z(L/2) - \delta_z(-L/2)] \qquad \text{C.8}$$

Following the derivation of Eq. C.7, the finite width Nagoya Type III coil has the $n - k_z$ transform,

$$J_\phi(r, n, k_z) = -\frac{4}{\pi}\, i^n\, \frac{I}{wn} \sin(k_z L/2)$$

$$\cdot \frac{\sin\left[(k_z + n/b)\, w/2\right]}{k_z + n/b}\, \delta_r(b) \qquad \text{C.9}$$

The axial (z) component of the current density for the last two coils is given in terms of the azimuthal component by the $n - k_z$ transform of the continuity equation.

$$J_z = \frac{-n}{bk_z}\, J_\phi \qquad \text{C.10}$$

Fig. C.3 Nagoya Type III

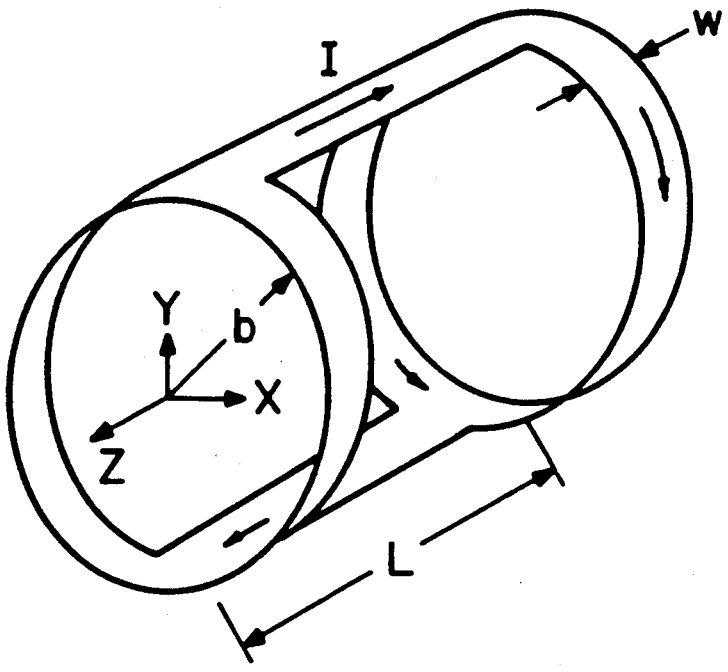

C.5 Rectangular aperture: For the three coils that have been discussed, the geometry of the conductor determines the current paths. The assumption of current uniformity over the cross-section is a reasonable approximation. For the aperture antenna diagrammed in Fig. C.4a, the current path flows around the periphery of rectangular cut out and the axial extent of the flow is not well defined. As an alternative, the RF excitation of the aperture can be defined by assuming a uniform (in ϕ and z) radial magnetic field over the rectangular cut out.

The rectangular aperture is modelled as diagrammed in Fig. C.4b. Shown is an unraveled view of the cylindrical surface r = c. A uniform magnetic field is assumed over the two rectangular ports of dimensions w × L. Outside the ports, the tangential components of the field are required to go to zero ($E_\phi = E_z = 0$) due to the assumed infinite conductivity of the metallic vacuum chamber. The time varying magnetic field (B_r) supports an inductive electric field over the aperture (E_ϕ^1, E_z^1) consistent with Faraday's law. At the edges of the aperture, electrostatic fields (E_ϕ^2, E_z^2) are required in order to satisfy Faraday's law for the various line integral paths indicated in Fig. C.4b (for example, paths $\S_2$, $\S_3$). Finally, the induced EMF due to the total magnetic flux through the aperture results in electric field, E_z^3, across the slots that interconnect the rectangular ports. For the rectangular aperture, the equivalent magnetization currents M_ϕ and M_z need to be calculated. In terms of the imposed fields,

$$M_\phi(c) = -E_z(c) = -(E_z^1 + E_z^2 + E_z^3)$$

$$M_z(c) = E_\phi(c) = E_\phi^1 + E_\phi^2 \qquad \text{C.11}$$

Fig. C.4a Rectangular Aperture

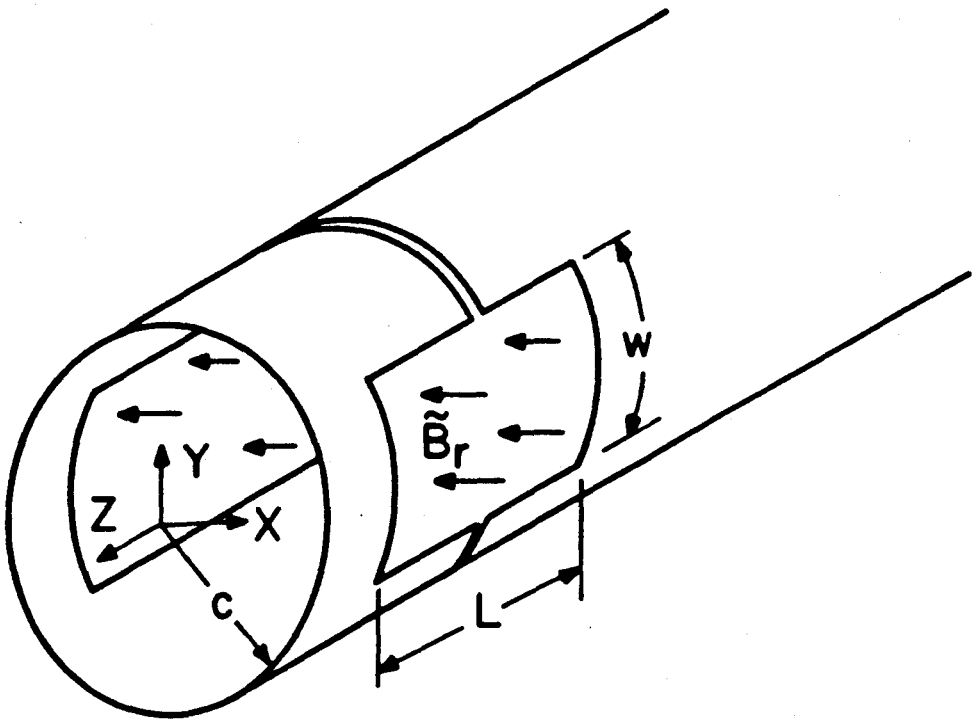

Fig. C.4b Rectangular Aperture

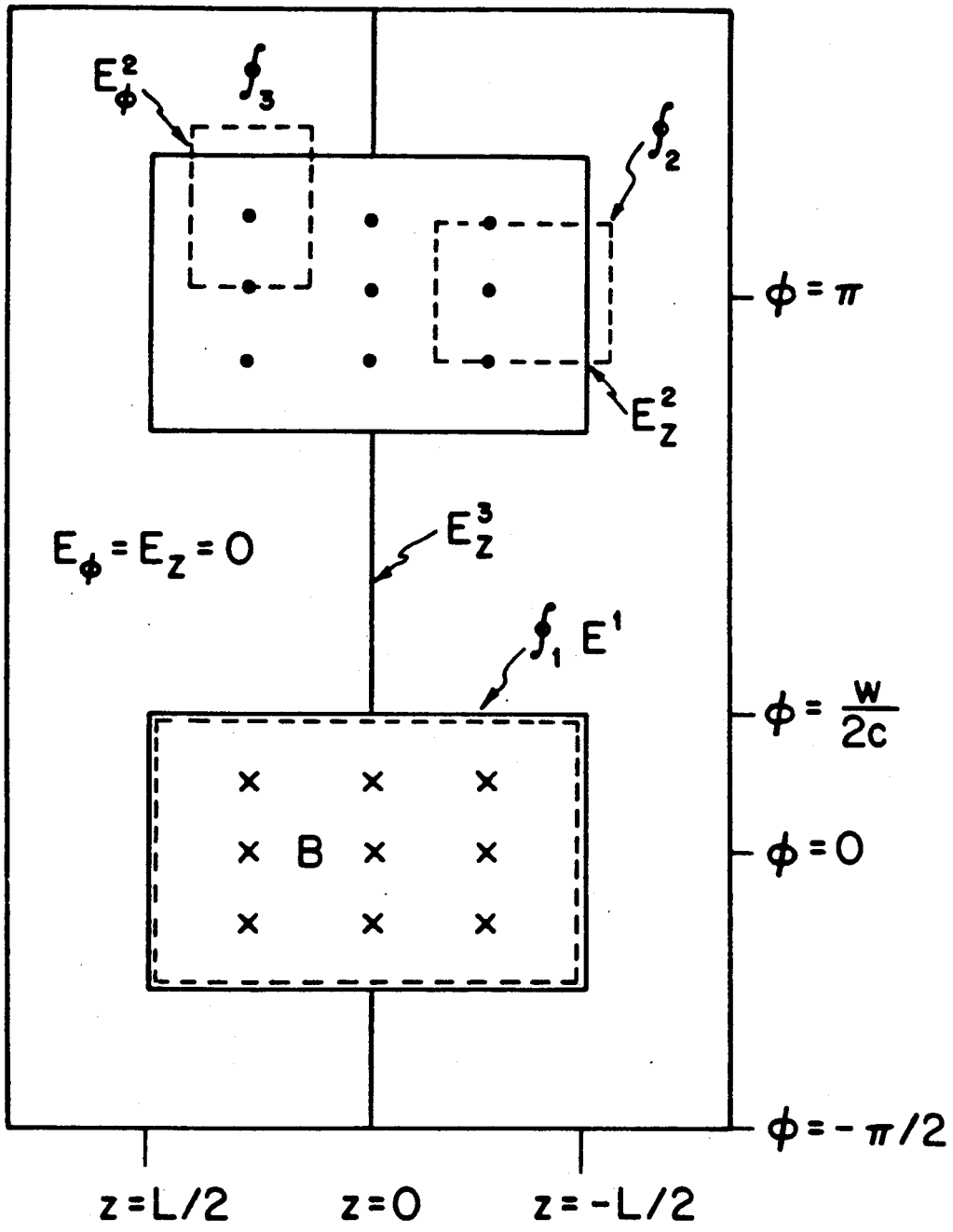

The electric fields E_z and E_ϕ are composed of the electric field components 1, 2, and 3 discussed above. The inductive electric field component (1) will be calculated first. The electric field around the periphery of the rectangular port (just inside the metallic conductor) is calculated from Faraday's law using path 1 defined in Fig. C.4.

$$E_a = \frac{i\ \omega\ B\ w\ L}{2(w + L)} \qquad \text{C.12}$$

The inductive electric field is assumed to be uniformly distributed along path 1. From symmetry considerations, $E_z = E_\phi = 0$ at $\phi = z = 0$. This implies a linear spatial variation of the field components.

$$E_\phi^1 = \frac{2z}{L} E_a \qquad z \text{ - variation over the aperture}$$

$$E_z^1 = -\phi/\phi_o\ E_a \qquad \phi \text{ - variation over the aperture}$$

where $\phi_o = \frac{w}{2c}$. The inductive components of the field are defined by,

$$E_\phi^1(\phi, z) = \frac{2z}{L} E_a\ [u_\phi(\pm \phi_o) - u_\phi(\pi \pm \phi_o)]\ u_z(\pm L/2) \qquad \text{C.13}$$

$$E_z^1(\phi, z) = E_a\ [-\phi/\phi_o\ u_\phi(\pm \phi_o) + \frac{(\phi - \pi)}{\phi_o} u_\phi(\pi \pm \phi_o)]\ u_z(\pm L/2)$$

The required electrostatic fields at the edges of the aperture are determined by consideration of the line integral paths 2 and 3 in Fig. C.4b. The z-component is calculated from path 2.

$$E_z^2(\phi, z) = E_a \frac{w}{2} \left[\frac{-\phi}{\phi_o} u_\phi(\pm \phi_o) + \frac{(\phi - \pi)}{\phi_o} u_\phi(\pi \pm \phi_o) \right]$$

$$\cdot [\delta_z(L/2) + \delta_z(-L/2)] \qquad \text{C.14}$$

The gap voltage across the inner connecting slot is given by (refer to Eq. C.12),

$$E_z^3(\phi, z) = - (w + L) E_a [u_\phi(\phi, \pi - \phi) - u_\phi(\pi + \phi, -\phi)] \delta_z(0) \qquad \text{C.15}$$

Finally, the required azimuthal component of the electrostatic field at the edge of the aperture can be calculated from line integral path 3.

$$E_\phi^2(\phi,z) = - \frac{E_a}{c} \left[\frac{(w + L)}{2} - z \right] f(\phi) u_z(0,L)$$

$$+ \frac{E_a}{c} \left[\frac{(w + L)}{2} + z \right] f(\phi) u_z(-L,0) \qquad \text{C.16}$$

where

$$f(\phi) = \delta_\phi(\phi_o) + \delta_\phi(-\phi_o) - \delta_\phi(\pi - \phi_o) - \delta_\phi(\pi + \phi_o)$$

With the assumed electric field pattern defined by Eqs. C.13 to C.16, the $n - k_z$ transform of the equivalent magnetization currents (Eq. C.11) can be obtained.

$$M_\phi(c) = - \frac{4i}{\pi} E_a \frac{c}{n} \left[\frac{2}{nk_z w} \sin(k_z L/2) \sin(n\phi_o) + f(n, k_z) \right]$$

C.17

$$M_z(c) = \frac{-4i}{\pi} E_a \frac{1}{k_z} \left[\frac{2}{nk_zL} \sin(k_zL/2) \sin(n\phi_o) - f(n, k_z) \right]$$

where

$$f(n, k_z) = \frac{(w + L)}{2c} \cos(n\phi_o) - \sin(k_zL/2) \frac{\cos(n\phi_o)}{k_zc}$$

C.17a

$$+ \cos(k_zL/2) \left[\frac{\sin(n\phi_o)}{n} - \phi_o \cos(n\phi_o) \right]$$

Equation C.17 defines the equivalent magnetization currents that characterize the aperture antenna.

C.6 Non-cylindrical coils: The remaining coils in Fig. 1.1 are not contained in a cylindrical surface (r = constant), and the induction theorem (discussed in Sec. 3) is used to obtain a set of equivalent source currents. The equivalent currents are defined by the fields of a particular coil imbedded in free space (the plasma and outer vacuum chamber removed). These fields are referred to as the incident fields, and the $(n - k_z)$ transform of these fields are required on various cylindrical surfaces bounding the source region. Since the transform of the incident fields are required, it is convenient to perform the calculation as a sum over cavity eigenmodes as the cavity size is allowed to be unbounded. This development is essentially the Green's function method or the method of normal mode analysis. We follow the development of Harrington which is summarized in Appendix D.

C.7 Line current: For the line current diagrammed in Fig. C.5, a rectangular set of coordinates is appropriate. It is required to calculate the transverse fields on the cylindrical surface r = b. Only TE fields are present, and the axial magnetic intensity (H_z) will be calculated first. The current distribution for the line current and an image current is expressed as,

$$J_y(x, z) = \frac{I}{w} u_z(\pm w/2) [\delta_x(b) - \delta_x(b + \Delta)] \qquad C.18$$

where $\Delta = 2(c - b)$. The axial magnetic intensity can be obtained from the formulas D.12a, D.11a, and D.3. The excitation coefficient is,

$$a_j = \frac{I}{\sqrt{\epsilon_o}} \frac{\sin(k_z w/2)}{w k_z} e^{-ik_x b} (1 - e^{-ik_x \Delta}) \qquad C.19$$

From D.11a, the axial magnetic intensity has the integral representation;

$$H_z(x) = i\sqrt{\epsilon_o} \int_{-\infty}^{\infty} \frac{dk_x \, e^{ik_x x}}{k_x^2 + \nu^2} \, a_j \qquad C.20$$

Evaluation of the above integral for $x < b$ and $\nu > 0$ yields,

$$H_z(x < b) = \frac{I}{w} \frac{\sin(k_z w/2)}{k_z} e^{-\nu(b-x)} (1 - e^{-\nu\Delta}) \qquad C.21$$

Using cylindrical coordinates, $r = x \cos \phi$, and taking the n - transform of C.21, an expression for the equivalent electric current J_ϕ is derived,

$$J_\phi(b) = H_z(b) \qquad C.22$$

Fig. C.5 Line Current

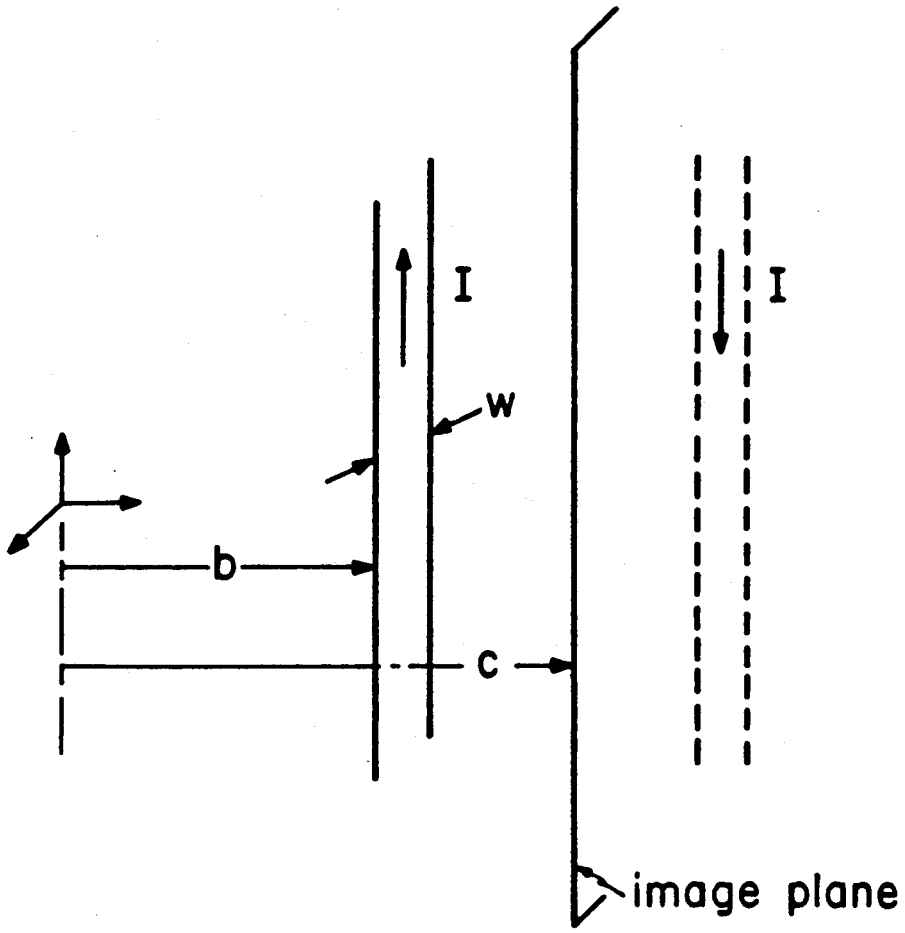

$$H_z(r, n, k_z) = \frac{I}{2} \frac{\sin(k_z w/2)}{k_z w/2} I_n(\nu r)\, e^{-\nu b}\,(1 - e^{-\nu\Delta})$$

The magnetization source current,

$$M_z(b) = E_\phi(b) = \frac{i\omega\mu_o}{\nu} H_z'(b) \qquad \text{C.23}$$

is obtained from Eq. B.5b. Note Eq. C.22 was derived assuming $\nu > 0$. For $k_o > k_z$, the analytic continuation of C.22 is,

$$H_z(r, n, k_z) = \frac{I}{2} \frac{\sin(k_z w/2)}{k_z w/2} e^{-in\pi/2} J_n(\nu b) \qquad \text{C.24}$$

$$\cdot\, e^{i\nu b}\,(1 - e^{i\nu\Delta})$$

C.8 Partial-turn loop: The partial-turn loop is diagrammed in Fig. C.6. The current pattern is composed of the following two components,

$$J_r(r, \phi, z) = \frac{I}{w} \frac{u_r(b, c)}{r} u_z(\pm w/2)\,[\delta_\phi(\theta/2) - \delta_\phi(-\theta/2)] \qquad \text{C.25}$$

$$J_\phi(r, \phi, z) = \frac{I}{w} u_\phi(\pm \theta/2)\, u_z(\pm w/2)\,[\delta_r(b) - \delta_r(c)]$$

Since $J_z = 0$, only TE_z modes are excited by the partial-turn loop. The equivalent source currents are determined by a calculation of the axial

Fig. C.6 Partial Turn Loop

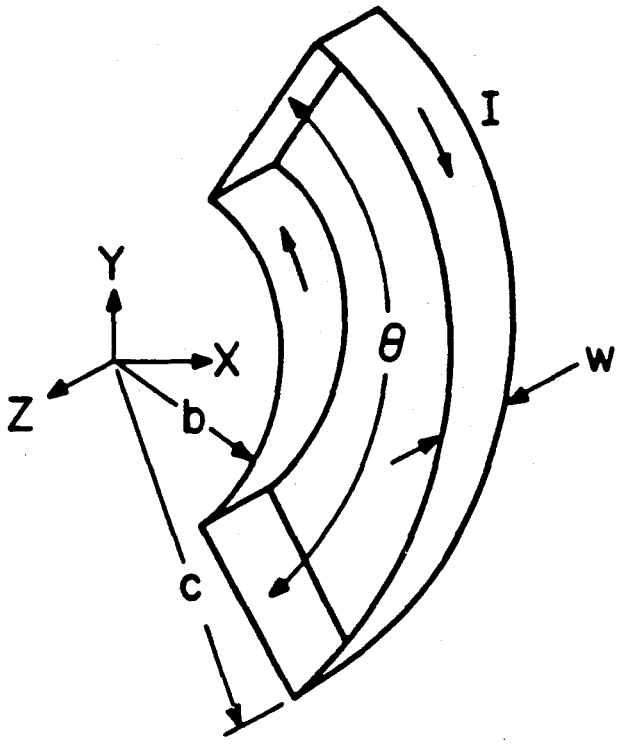

magnetic field on the cylindrical surfaces r = b and r = c. The H_z field is calculated using Eqs. D.7, D.3, and D.8. The excitation coefficient is determined by Eq. D.3.

$$a_j = \frac{i}{\sqrt{\epsilon_o}} \; I_o(n, k_z) \left[b \, J_n'(k_r b) - c J_n'(k_r c) \right. \tag{C.26}$$

$$\left. + n \int_b^c \frac{n \, J_n(k_r r) \, dr}{k_r r} \right]$$

$$I_o(n, k_z) = \frac{I \sin(k_z w/2)}{k_z w/2} \; \frac{\sin(n\theta/2)}{n\pi} \tag{C.27}$$

Using Eq. D.7, the axial magnetic field becomes,

$$H_z(r, n, k_z) = -I_o(n, k_z) \int_o^\infty \frac{k_r^2 \, dk_r}{k_r^2 + \nu^2} \; J_n(k_r r) \; S(k_r) \tag{C.28}$$

$$S(k_r) = b \, J_n'(k_r b) - c \, J_n'(k_r c) + n \int_b^c \frac{n \, J_n(k_r x)}{k_r x} \, dx$$

For $\nu^2 > 0$, the integral over the k_r integration is tabulated. That integral along with its analytic continuation for $\nu^2 < 0$ is contained in a

short integral table at the end of Appendix D. With the aid of this table, the H_z field for $r \leq b$ becomes,

$$H_z(r, n, k_z) = -I_o(n, k_z)\, I_n(\nu r) \left[\nu b\, K_n'(\nu b)\right. \tag{C.29a}$$

$$\left. - \nu c\, K_n'(\nu c) + n \int_b^c \frac{n\, K_n(\nu x)}{x}\, dx\right]$$

for $r \geq c$,

$$H_z(r, n, k_z) = -I_o(n, k_z)\, K_n(\nu r) \left[\nu b\, I_n'(\nu b) - \nu c\, I_n'(\nu c)\right. \tag{C.29b}$$

$$\left. + n \int_b^c \frac{n\, I_n(\nu x)}{x}\, dx\right]$$

Using Eq. C.29, the equivalent source currents for the partial-turn loop are,

$$J_\phi(b) = H_z(b) \tag{C.30a}$$

$$M_z(b) = E_\phi(b) = \frac{i\omega\mu_o}{\nu} H_z'(b) \tag{C.30b}$$

$$M_z(c) = -E_\phi(c) = \frac{-i\omega\mu_o}{\nu} H_z'(c) \tag{C.30c}$$

For $\nu^2 < 0$, the modified Bessel functions in Eq. C.29 are replaced by Bessel functions of the first and second kind ($I_n \rightarrow J_n$ and $K_n = -\pi/2\ Y_n$).

C.9 Half-Nagoya coil: The half-Nagoya coil is diagrammed in Fig. C.7. The current pattern is composed of radial and axial components.

$$J_r(r, \phi, z) = \frac{I}{w}\frac{b}{r}\, u_r(b, c)\, u_\phi(\pm w/2b)\, [\delta_z(L/2) - \delta_z(-L/2)] \qquad \text{C.31}$$

$$J_z(r, \phi, z) = \frac{I}{w}\, [\delta_r(b) - \frac{b}{c}\,\delta_r(c)]\, u_\phi(\pm w/2b)\, u_z(\pm L/2)$$

Since $J_z \neq 0$, both TE_z and TM_z modes are excited by the half-Nagoya coil. The equivalent source currents are defined in terms of the axial field components, H_z and E_z. The calculation of these fields follows that outlined in the discussion of the partial-turn loop. For $r < b$, the axial fields have the form,

$$H_z(r) = -I_1(n, k_z)\, I_n(\nu r) \int_{\nu b}^{\nu c} \frac{n\, K_n(x)}{x}\, dx \qquad \text{C.32a}$$

$$E_z(r) = \frac{i\omega\mu_o}{k_z}\, I_1(n, k_z)\, I_n(\nu r)\, [K_n(\nu b) - K_n(\nu a)] \qquad \text{C.32b}$$

$$I_1(n, k_z) = \frac{I}{\pi}\,\frac{\sin(nw/2b)}{nw/2b}\, \sin(k_z L/2) \qquad \text{C.32c}$$

For $r > c$,

Fig. C.7 Half Nagoya

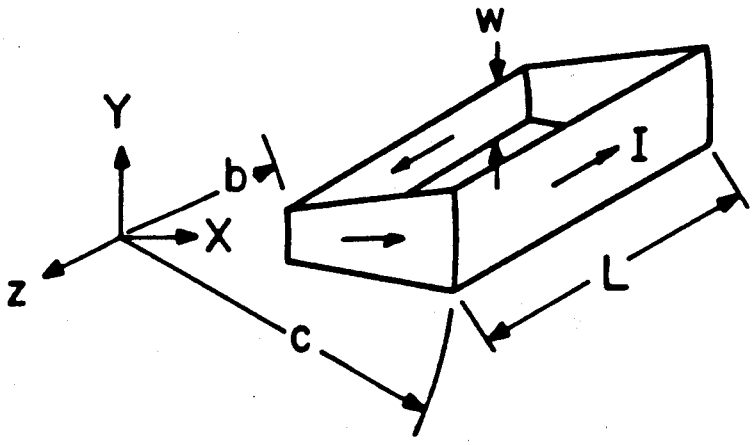

$$H_z(r) = -I_1(n, k_z)\, K_n(\nu r) \int_{\nu b}^{\nu c} \frac{n\, I_n(x)}{x}\, dx \qquad \text{C.33a}$$

$$E_z(r) = \frac{i\omega\mu_o}{k_z}\, I_1(n_1, k_z)\, K_n(\nu r)\, [I_n(\nu b) - I_n(\nu c)] \qquad \text{C.33b}$$

The equivalent sources currents are given by,

$$J_\phi(b) = H_z(b), \qquad J_z(b) = -H_\phi(b)$$

$$M_\phi(b) = -E_z(b), \qquad M_z(b) = E_\phi(b) \qquad \text{C.34}$$

and

$$M_\phi(c) = E_z(c), \qquad M_z(c) = -E_\phi(c)$$

The transverse fields are calculated from Eqs. C.33 - 34 and Eqs. B.5a - d.

Appendix D Normal Mode Analysis of the Incident Fields of Non-cylindrical Current Sources

A normal mode analysis is used to calculate the incident fields, and as a consequence, the equivalent source currents of antennas with radial feeders. This appendix summarizes the results of an analysis by Harrington who calculates the excitation of normal modes in a cavity by a current source[21]. After the results of the normal mode analysis are presented, the incident fields which contribute to the total vacuum field solution are calculated for the line current, partial-turn, and half-Nagoya.

D.1 General formulation of the normal mode analysis: The electric and magnetic field inside a cavity excited by an electric source current ($\vec{J}$) can be represented as a sum over the normal modes of the cavity. As the cavity size becomes unbounded, the summation goes over to an integration and the normal modes become a continuum.

$$\vec{E}(\vec{r}) = \int_{\vec{k}} d\vec{k} \; \frac{i\omega \, E_j(\vec{k})}{\omega_j^2 - \omega^2} \; a_j \qquad \text{D.1}$$

$$\vec{H}(\vec{r}) = \int_{\vec{k}} d\vec{k} \; \frac{i\omega_j \, H_j(\vec{k})}{\omega_j^2 - \omega^2} \; a_j \qquad \text{D.2}$$

$$a_j = \int_{\vec{r}} d\vec{r} \; \vec{J} \cdot \vec{E}_j^* \qquad \text{D.3}$$

$$\omega_j^2 = (\varepsilon_o \mu_o)^{-1} \quad (k_r^2 + k_z^2) \qquad \text{D.4}$$

$$\int_{\vec{k}} d\vec{k} = \int_0^{\infty} k_r \, dk_r \sum_{n=-\infty}^{\infty} \int_{-\infty}^{\infty} \frac{dk_z}{2\pi} \qquad \text{D.5}$$

$$\int_{\vec{r}} d\vec{r} = \int_0^{\infty} r \, dr \int_0^{2\pi} \frac{d\phi}{2\pi} \int_{-\infty}^{\infty} dz \qquad \text{D.6}$$

Equations D.4 to D.6 were defined assuming a cylindrical coordinate system. Equations D.1 to D.3 state that the fields in an unbounded domain can be represented as a sum over the normal modes of the system ($\vec{E}_j$, $\vec{H}_j$) weighted by the excitation coefficient (a_j) of that mode due to the specified current source. The form of the denominator in Eqs. D.1 and D.2 is also plausible. For a bounded cavity, the denominator indicates a singularity at the resonant frequency of a particular eigenmode. For an unbounded system, the singularity represents the radiation condition for non-stationary ($\nabla \cdot \vec{J} \neq 0$) current sources. For stationary current sources, the apparent singularity in the denominator is removed by zeros of the numerator (a stationary current source does not radiate). Since the $n - k_z$ transform of the fields is required of the equivalent source currents, it is only necessary to perform the k_r integration in Eq. D.5.

$$\vec{E}(r, n, k_z) = \int_0^{\infty} dk_r \frac{i\omega k_r \vec{E}_j}{\omega_j^2 - \omega^2} a_j \qquad \text{D.7a}$$

$$\vec{H}(r, n, k_z) = \int_0^{\infty} dk_r \frac{i\omega_j k_r \vec{H}_j}{\omega_j^2 - \omega^2} a_j \qquad \text{D.7b}$$

The normal modes of the system are field solutions TE_z or TM_z. The modes with the electric field transverse to z have the component form,

$$H_z^j = J_n(k_r r)\ f(\phi,z)\ H_j \qquad \text{D.8a}$$

$$H_r^j = \frac{ik_z}{k_r}\ J_n'(k_r r)\ f(\phi,z)\ H_j \qquad \text{D.8b}$$

$$H_\phi^j = \frac{-k_z}{k_r}\ \frac{n\ J_n(k_r r)}{k_r r}\ f(\phi,z)\ H_j \qquad \text{D.8c}$$

$$E_r^j = \frac{\omega_j\ \mu_o}{k_z}\ H_\phi^j \qquad \text{D.8d}$$

$$E_r^j = \frac{-\omega_j\ \mu_o}{k_z}\ H_r^j \qquad \text{D.8e}$$

$$H_j = \frac{k_r}{\omega_j\ \mu_o \sqrt{\epsilon_o}} \qquad \text{D.8f}$$

The modes with the magnetic field transverse to z have the component form.

$$E_z^j = J_n(k_r r)\ f(\phi,z)\ E_j \qquad \text{D.9a}$$

$$E_r^j = \frac{ik_z}{k_r} J_n'(k_r r)\, f(\phi,z)\, E_j \qquad \text{D.9b}$$

$$E_\phi^j = \frac{-k_z}{k_r} \frac{n J_n(k_r r)}{k_r r} f(\phi,z)\, E_j \qquad \text{D.9c}$$

$$H_r^j = \frac{-\omega_j \epsilon_o}{k_z} E_\phi^j \qquad \text{D.9d}$$

$$H_\phi^j = \frac{\omega_j \epsilon_o}{k_z} E_r^j \qquad \text{D.9e}$$

$$E_j = \frac{k_r}{\omega_j \epsilon_o \sqrt{\mu_o}} \qquad \text{D.9f}$$

and

$$f(\phi,z) = e^{in\phi + ik_z z} \qquad \text{D.10}$$

For the line-current diagrammed in Fig. C.5, a normal mode expansion is made in rectangular coordinates. Assuming uniformity in the y-direction, Eqs. D.7 to D.8 become,

$$\vec{H}(x, k_z) = \int_{-\infty}^{\infty} dk_x \frac{i\omega_j}{\omega_j^2 - \omega^2} \vec{H}_j a_j \qquad \text{D.11a}$$

$$\vec{E}(x, k_z) = \int_{-\infty}^{\infty} dk_x \frac{i\omega}{\omega_j^2 - \omega^2} \vec{E}_j a_j \qquad \text{D.11b}$$

Since only TE_z modes are excited and $k_y = 0$, the normal modes have only the following three components.

$$H_z^j = H_j f(x, z) \qquad \text{D.12a}$$

$$H_x^j = \frac{-k_z}{k_x} H_j f(x, z) \qquad \text{D.12b}$$

$$E_y^j = \frac{\omega_j \mu_o}{k_x} H_j f(x, z) \qquad \text{D.12c}$$

$$H_j = \frac{k_x}{\omega_j \mu_o \sqrt{\epsilon_o}} \qquad \text{D.12d}$$

and

$$f(x, z) = e^{ik_x x + ik_z z} \qquad \text{D.12e}$$

D.2 Incident fields: In the remainder of the appendix, the incident fields of the line current, partial turn, and half-Nagoya coil are calculated. The calculation utilizes the normal mode analysis presented above, and the various steps in the calculation follow those used in obtaining the

equivalent source currents for these coils (see the latter part of Appendix C).

D.3 Line current: For the line current, the field solution defined by spatial region $b < x < b + \Delta/2$ ($\Delta = 2\,(c - b)$) is required. An integral expression for $H_z(x)$ is defined by Eqs. C.19 and C.20. Evaluating this integral, using contour integration around the poles at $k_x = \pm i\nu$, the following result is obtained for $\nu > 0$.

$$H_z^i(x, k_z) = \frac{-I}{2} \frac{\sin(k_z w/2)}{k_z w/2} \left[e^{-\nu(x-b)} + e^{-\nu(d-x)} \right] \qquad \text{D.13}$$

where $d = b + \Delta$. The transverse fields are obtained from Eqs. D.11 and D.12. For $\nu < 0$, we have the same result above with $\nu \to i\nu$.

D.4 The partial-turn loop: The incident fields of the partial-turn loop are defined in the region $b \leq r \leq c$. The integral expression Eq. C.28 can be used to evaluate the axial magnetic field.

$$H_z^i(r, n, k_z) = - I_o(n, k_z) \left\{ K_n(\nu r) \left[\nu b\, I_n'(\nu b) + n \int_{\nu b}^{\nu r} \frac{n\, I_n(x)}{x}\, dx \right] \right.$$

$$\left. + I_n(\nu r) \left[-\nu c\, K_n'(\nu c) + n \int_{\nu r}^{\nu c} \frac{n\, K_n(x)}{x}\, dx \right] \right\} \qquad \text{D.14}$$

Since $b < r < c$ is a source region, the incident fields can no longer be obtained from a direct application of Eqs. B.5a - d. A proper procedure is to develop k_r-integral expressions for the transverse fields using Eqs. D.7

and D.8. The integral expressions can then be evaluated with reference to the table at the end of the appendix.

$$H_r^i(r, n, k_z) = \frac{-ik_z}{\nu} H_z^{i'}(r, n, k_z) \qquad \text{D.15a}$$

$$H_\phi^i(r, n, k_z) = \frac{k_z}{\nu} \frac{n}{\nu r} H_z^i(r, n, k_z) + \frac{k_z}{\nu} I_o(n, k_z) \frac{n}{\nu r} \qquad \text{D.15b}$$

$$E_r^i = \frac{\omega\mu_o}{k_z} H_\phi^i \qquad \text{D.15c}$$

$$E_\phi^i = \frac{-\omega\mu_o}{k_z} H_r^i \qquad \text{D.15d}$$

Note that Eq. D.15 is the same as Eq. B.5 with the addition of a second term in Eq. D.15b which eliminates a spurious singularity at $\nu = 0$. This term is required to insure the continuity of the electric field through the source region.

D.5 The half-Nagoya coil: The incident fields of the half-Nagoya coil in the region $b < r < c$ can be obtained using the same procedure as with the partial-turn loop.

$$H_z^i(r, n, k_z) = -I_1(n, k_z) \left\{ K_n(\nu r) \int_{\nu b}^{\nu r} \frac{n\, I_n(x)}{x}\, dx \right. \qquad \text{D.16a}$$

$$+ I_n(\nu r) \int_{\nu r}^{\nu c} \frac{n K_n(x)}{x} dx \Bigg\}$$

$$E_z^i (r, n, k_z) = \frac{i\omega\mu_o}{k_z} I_1(n, k_z) [K_n(\nu r) I_n(\nu b) - I_n(\nu r) K_n(\nu c)] \qquad \text{D.16b}$$

$$E_\phi^i = \frac{k_z}{\nu} \frac{n}{\nu r} E_z^i + \frac{i\omega\mu_o}{\nu} H_z^{i'} \qquad \text{D.16c}$$

$$H_r^i = \frac{-\omega\epsilon_o}{\nu} \frac{n}{\nu r} E_z^i - \frac{ik_z}{\nu} H_z^{i'} \qquad \text{D.16d}$$

$$E_r^i = \frac{\omega\mu_o}{\nu} \frac{n}{\nu r} H_z^i - \frac{ik_z}{\nu} E_z^{i'} + \frac{\omega\mu_o}{\nu^2 r} I_1(n, k_z) \qquad \text{D.16e}$$

$$H_\phi^i = \frac{1}{i\omega\mu_o} \left[i k_z E_r^i - \frac{\partial E_z^i}{\partial r} \right] \qquad \text{D.16f}$$

The second term in Eq. D.16e was added to insure the continuity of E_r through the source region.

D.6 Useful integrals: The following short table of integrals[28] is helpful in calculating the equivalent source currents and incident fields for the partial-turn and half-Nagoya coils.

$\nu^2 > 0,$

$$\int_0^\infty \frac{dk_r}{k_r^2 + \nu^2} \; k_r \, J_n(k_r r) \, J_n(k_r b) = \begin{cases} I_n(\nu r) \, K_n(\nu b) & r < b \\ K_n(\nu r) \, I_n(\nu b) & r > b \end{cases} \qquad \text{D.17a}$$

$\nu^2 = k_z^2 - k_o^2 < 0,$

$$\int_0^\infty \frac{dk_r}{k_r^2 + \nu^2} \; k_r \, J_n(k_r r) \, J_n(k_r b) = \begin{cases} \frac{-\pi}{2} J_n(\nu r) \, Y_n(\nu b) & r < b \\ \frac{-\pi}{2} Y_n(\nu r) \, J_n(\nu b) & r > b \end{cases} \qquad \text{D.17b}$$

Appendix E Transverse Plasma Fields

The transverse fields are calculated in terms of the wave amplitudes A_j, B_j (defined in Sec. 6) in this appendix. The transverse plasma fields are defined in terms of the axial field components, H_z and E_z (Eqs. 6.8a and b).

$$E_r = \omega\mu_o(\delta_o H_z' + \delta_1 \frac{n}{r} H_z) - ik_z(\delta_1 E_z' + \delta_o \frac{n}{r} E_z) \qquad \text{E.1a}$$

$$E_\phi = i\omega\mu_o(\delta_1 H_z' + \delta_o \frac{n}{r} H_z) + k_z(\delta_o E_z' + \delta_1 \frac{n}{r} E_z) \qquad \text{E.1b}$$

$$H_r = -i\, k_z(\delta_1 H_z' + \delta_o \frac{n}{r} H_z) - \omega\epsilon_o(\delta_z E_z' + \delta_2 \frac{n}{r} E_z) \qquad \text{E.1c}$$

$$H_\phi = k_z(\delta_o H_z' + \delta_1 \frac{n}{r} H_z) - i\omega\epsilon_o(\delta_2 E_z' + \delta_z \frac{n}{r} E_z) \qquad \text{E.1d}$$

where,

$$\delta_o = k_o^2 D\, \delta_3^{-1} \qquad \text{E.2a}$$

$$\delta_z = k_z^2 D\, \delta_3^{-1} \qquad \text{E.2b}$$

$$\delta_1 = (k_z^2 - k_o^2 S)\ \delta_3^{-1} \qquad \text{E.2c}$$

$$\delta_2 = (k_z^2 S - k_o^2 R L)\ \delta_3^{-1} \qquad \text{E.2d}$$

$$\delta_3 = (k_o^2 R - k_z^2)\ (k_o^2 L - k_z^2) \qquad \text{E.2e}$$

The transverse fields may be expressed in terms of the wave amplitudes. Using Eq. 6.10 and Eq. 6.8 as expressions for the axial fields, and defining;

$$a_1 = A_{2j-1}, \quad a_2 = A_{2j}, \quad a_3 = B_{2j-1}, \quad a_4 = B_{2j} \qquad \text{E.3}$$

the transverse fields are:

$$E_r = \sum_{\ell=1}^{4} e_r^{\ell} a_{\ell} \qquad \text{E.4a}$$

$$E_\phi = \sum_{\ell=1}^{4} e_\phi^{\ell} a_{\ell} \qquad \text{E.4b}$$

$$H_r = \sum_{\ell=1}^{4} h_r^{\ell} a_{\ell} \qquad \text{E.4c}$$

$$H_\phi = \sum_{\ell=1}^{4} h_\phi^\ell a_\ell \qquad \text{E.4d}$$

The coefficients $e_r^\ell(j)$, etc. are given by,

$$e_r^\ell = -i\, e_2^\ell\, G'_\ell - i\, e_1^\ell B_\ell \qquad \text{E.5a}$$

$$e_\phi^\ell = e_1^\ell\, G'_\ell + e_2^\ell B_\ell \qquad \text{E.5b}$$

$$h_r^\ell = -i\, h_2^\ell\, G'_\ell - i\, h_1^\ell B_\ell \qquad \text{E.5c}$$

$$h_\phi^\ell = h_1^\ell\, G'_\ell + h_2^\ell B_\ell \qquad \text{E.5d}$$

In Eq. E.5,

$$G_1 = H_1^n(k_{r1}r) \quad G_2 = H_2^n(k_{r1}r) \qquad B_{1,2} = (n/r)\, G_{1,2} \qquad \text{E.6}$$

$$G_3 = H_1^n(k_{r2}r) \quad G_4 = H_2^n(k_{r2}r) \qquad B_{3,4} = (n/r)\, G_{3,4}$$

The prime on the function G_ℓ indicates differentiation with respect to r. The following coefficients have been defined.

$$e_1^{\ell} = i\omega\mu_o \delta_1 u_{\ell} + k_z \delta_o v_{\ell} \qquad \text{E.7a}$$

$$e_2^{\ell} = i\omega\mu_o \delta_o u_{\ell} + k_z \delta_1 v_{\ell} \qquad \text{E.7b}$$

$$h_1^{\ell} = k_z \delta_o u_{\ell} - i\omega\epsilon_o \delta_2 v_{\ell} \qquad \text{E.7c}$$

$$h_2^{\ell} = k_z \delta_1 u_{\ell} - i\omega\epsilon_o \delta_z v_{\ell} \qquad \text{E.7d}$$

with,

$$u_1 = u_2 = 1, \quad u_3 = u_4 = y_2 \qquad \text{E.8}$$

$$v_1 = v_2 = z_1, \quad v_3 = v_4 = 1$$

For the fields in the "j th" strata, all the dielectric elements and wave numbers are evaluated for the plasma parameters of that strata. The coefficients in Eq. 6.16a are defined by,

$$\alpha_{1\ell} = e_{\phi}^{\ell} - \frac{k_z}{\nu}\frac{n}{\nu a} v_{\ell} + \frac{i\omega\mu_o}{\nu}\frac{\Delta_{a'c'}}{\Delta_{ac'}} u_{\ell} \quad G_{\ell} \cdot \sigma_{\nu} \qquad \text{E.9a}$$

$$\alpha_{2\ell} = h_{\phi}^{\ell} + \frac{i\omega\epsilon_o}{\nu}\frac{\Delta_{a'c}}{\Delta_{ac}} v_{\ell} - \frac{k_z}{\nu^2}\frac{n}{a} u_{\ell} \quad G_{\ell} \cdot \sigma_{\nu} \qquad \text{E.9b}$$

References

1. J. Hosea et al., Proceedings of the 3rd Joint Varenna-Grenoble International Symposium on Heating in Toroidal Plasmas, Grenoble, France, p. 213 (1982).

2. Equipe TFR, Proceedings of the 3rd Joint Varenna-Grenoble International Symposium on Heating in Toroidal Plasmas, Grenoble, France, p. 225 (1982).

3. I. B. Bernstein, Phys. Rev. 109 (1958) 10.

4. S. J. Buchshaum, Phys. Fluids 3, (1960) 418.

5. A. Hirose, I. Alexeff, W. D. Jones, Phys. Fluids 13 (1970) 2039.

6. A. Hasegawa, et al., Phys. Rev. Lett. 35 (1975) 370.

7. D. G. Swanson, Y. C. Ngan, Phys. Rev. Lett. 35 (1975) 517.

8. D. G. Swanson, Phys. Rev. Lett. 36 (1976) 316.

9. J. C. Hosea, R. M. Sinclair, Phys. Fluids 13 (1970) 701.

10. C. C. Swett et al., NASA TM X-52091 NASA Technical Memorandum (1965).

11. T. H. Stix, The Theory of Plasma Waves, McGraw-Hill, New York (1962).

12. F. J. Paoloni, Phys. Fluids 18, (1975) 640.

13. M. Ono, et al., Research Report IPPJ-662, Institute of Plasma Physics, Nagoya University.

14. M. Ono, K. L. Wong, G. A. Wurden, Phys. Fluids 26, (1983) 298.

15. T. Watari, et al., Phys. Fluids 21 (1978) 2076.

16. J. M. Dawson, et al., Phys. Rev. Lett. 37 (1976) 1547.

17. N. Hershkowitz, et al., Phys. Rev. Lett. 49 (1982) 1489.

18. J. R. Ferron, et al., Phys. Rev. Lett. 21 (1983) 1955.

19. O. M. Shvets, et al., Sov. J. Plasma Phys. 7(3) 261.

20. B. D. McVey, TRW Report, TASK II-2740.

21. R. F. Harrington, Time-Harmonic Electromagnetic Fields, McGraw-Hill, New York (1961).

22. M. Abramowitz, I. A. Stegun, Handbook of Mathematical Functions National Bureau of Standards (1965).

23. N. A. Krall, A. W. Trivelpiece, Principles of Plasma Physics, McGraw-Hill, New York (1973).

24. P. L. Bhatnagar, E. P. Gross, M. Krook, Phys. Rev. 94 (1954) 511.

25. G. Schmidt, Physics of High Temperature Plasmas, Academic Press, New York (1966).

26. E. D. Denman, Coupled Modes in Plasmas, Elastic Media, and Parametric Amplifiers, American Elsevier, New York (1970).

27. F. E. Terman, Radio Engineers' Handbook, McGraw-Hill, New York 1943.

28. I. S. Gradshteyn, I. M. Ryzhik, Table of Integrals Series and Products, Academic Press, New York 1965.